Biomechanical Models and Robotic Systems for Human Motion Assessment

Sarah Seko

Electrical Engineering and Computer Sciences
University of California, Berkeley

Technical Report No. UCB/EECS-2021-22
http://www2.eecs.berkeley.edu/Pubs/TechRpts/2021/EECS-2021-22.html

May 1, 2021

Biomechanical Models and Robotic Systems for Human Motion Assessment

by

Sarah Seko

A dissertation submitted in partial satisfaction of the

requirements for the degree of

Doctor of Philosophy

in

Engineering – Electrical Engineering and Computer Sciences

in the

Graduate Division

of the

University of California, Berkeley

Committee in charge:

Professor Ruzena Bajcsy, Chair
Professor Claire Tomlin
Professor Oliver O'Reilly

Spring 2020

Biomechanical Models and Robotic Systems for Human Motion Assessment

Abstract

Biomechanical Models and Robotic Systems for Human Motion Assessment

by

Sarah Seko

Doctor of Philosophy in Engineering – Electrical Engineering and Computer Sciences

University of California, Berkeley

Professor Ruzena Bajcsy, Chair

Over the past several decades, there have been advances in the development of complex robotic devices for daily assistance or rehabilitation. The use of such devices, however, has largely remained limited to a research setting due to the prohibitive cost and required operational engineering expertise. Likewise, dedicated biomechanics facilities perform quantitative motion analysis, contrasting the qualitative and static imaging methods which are standard in clinical care. The aim of this dissertation is to develop and validate affordable methods and devices for assessing and assisting human motion.

We first present a framework for improved estimation of whole-body human kinematics with data from a single depth-camera. The algorithm incorporates biomechanical and dynamic constraints for near-real time analysis of human motion. The approach is validated against data from a ground-truth motion capture system on sit-to-stand (STS), an activity of daily living which requires significant torque generation and coordinated movement of multiple joints. We additionally present two methods for modeling the torso: a generalized relationship for the lower-lumbar angle and an optimization-based method for estimating a subject-specific model. Building on these modeling methods, we introduce a passive elastic knee orthotic device which provides bilateral knee assistance during STS. The device design and analysis integrate models of the human and device dynamics. Preliminary human subjects tests demonstrate a decrease in the human knee torque as well as positive changes in whole-body biomechanics. Finally, we introduce an affordable planar robotic manipulandum for upper limb assessment and assistance. The mechanical, electrical, and control architectures are presented, along with preliminary human subjects tests of reaching and elliptical trajectories with force field assistance under an admittance controller. A protocol for the assessment of strength and coordination is introduced and integrated with a biomechanical model of the arm. With a total material cost of less than $800, this device provides an accessible platform for clinical robotic assessment and rehabilitation.

To my parents, Raymon and Georgianna Seko, for their endless love, support, and encouragement.

Contents

List of Figures

List of Tables

Acknowledgments

This work would not have been possible without the support of my collaborators and community. Firstly, I would like to thank my research advisor, Professor Ruzena Bajcsy, for giving me the freedom to explore my research interests, asking tough questions, and supporting me throughout my PhD. I would also like to thank my dissertation committee members, Professors Claire Tomlin and Oliver O'Reilly, as well as my qualifying exam committee member Professor Karunesh Ganguly.

I am grateful for the research insights and kindness that have been given to me by the members of the Human Assistive Robotic Technologies (HART) Lab. I would especially like to thank Robert Peter Matthew, who has been my closest collaborator and friend throughout my time at Berkeley. My additional co-authors who contributed directly to this dissertation include Raziel Riemer, Jeffrey Lotz, and Joel Loeza. I would additionally like to thank Gregorij Kurillo, Louis Cheng, Brian Feeley, Jeannie Bailey, and Patrick Curran for feedback on the clinical depth-camera framework, and Adelyn Tu-Chan and Karunesh Ganguly for insight into the design of the upper-limb assistive device. Special thanks go to Shirley Salanio and Jessica Gamble for their friendly support in stressful times.

Finally, I would like to thank all of my family, friends, and teachers who have supported and encouraged me throughout my education.

This dissertation includes research supported by the Office of Naval Research Embedded Humans MURI Award (N000141310341), the National Science Foundation SBIR Award (1R41AR068202-01A1), and the SanDisk Fellowship.

Chapter 1

Introduction

Motion of the human body is achieved through the complex and coordinated control of the elements of the musculoskeletal system by the central nervous system. Typical biomechanical function can be disrupted by neuromusculoskeletal injury or disease resulting in deficits in areas such as strength, coordination, and range of motion. These decreases in motor function affect the ability to complete activities of daily living (ADLs), fundamental actions necessary to care for oneself independently [1].

The quantitative assessment of motoric ability and impairment is useful for diagnosis, recovery tracking, and the prescription of medical intervention and treatment. Human motion analysis utilizes quantitative methods for tracking kinematics and developing biomechanical models, estimating internal forces and torques during movement. These methods often rely on sophisticated and expensive motion capture technology, which require specialized facilities and expertise. The clinical standard of care does not typically incorporate these tools, relying on qualitative and subjective measures of motion or static medical imaging.

The field of assistive or rehabilitation robotics is inherently connected to motion assessment, providing technologies for both collecting quantitative data of human motion and administering assistance. These devices mechanically connect to the subject, enabling measurement of interactions forces which can inform biomechanical models. Additionally, quantitative assessment of a subject's ability or performance can drive individualized models or therapy protocols. Despite significant engineering advances in the field of rehabilitation robotics over the last decades, we have not seen a widespread implementation of these complex robotic mechanisms in clinical or home care. While several factors inhibit the adoption of rehabilitation robotics, an undeniable barrier results from high device cost and complexity. This inaccessibility further contributes to a limited understanding of models of recovery and optimal robotic rehabilitation protocols.

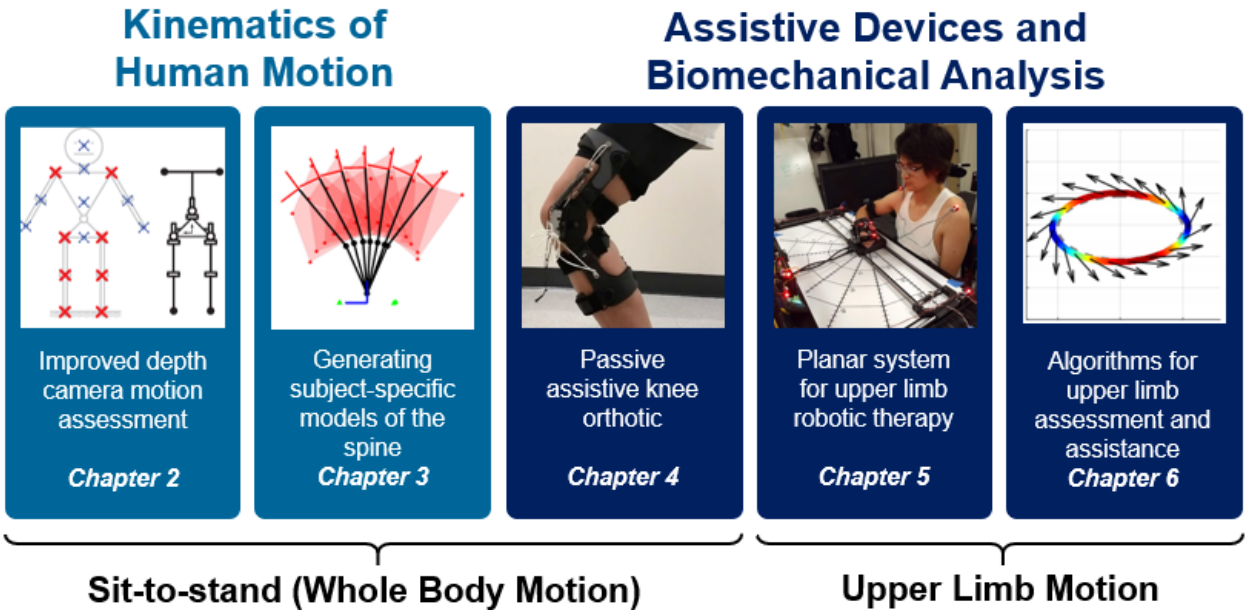

Figure 1.1: Thesis overview

1.1 Thesis Overview and Contributions

The focus of this dissertation is the development and validation of affordable methods and devices for assessing and assisting human motion with the future aim of translation to clinical or home settings. We utilize tools from rigid-body modeling, kinematic and dynamic analysis, optimization, and interaction control. An emphasis is placed on empirical validation through hardware characterization and human subjects studies which compare our technologies to ground truth measures. The organization and key contributions of the thesis are summarized below and shown in Figure 1.1.

Human Motion Analysis (Chapters 2 and 3)

We first present a framework for accurate and fast recovery of joint kinematics using a single-depth camera [2]. This method incorporates biomechanical and dynamical constraints into the recovery of joint kinematics from unconstrained joint center positions measured by a depth camera. Our method is validated on 10 subjects completing sit-to-stand (STS), an ADL and action of clinical interest. When compared against a gold-standard, marker-based, motion capture system, our method was found to produce accurate, reproducible, and consistent estimates of joint center positions and kinematics. The single depth camera can be used in a clinical or home space with a total test time of less than one minute and near real-time processing, providing an affordable and fast tool for clinical motion assessment.

While it was applied to STS and the single-leg squat motions, the method is extendable to other motions.

In whole-body motion analysis, the human torso is often modeled as a single rigid segment. More detailed modeling of the low back allows for the analysis of posture and loading on the spine. In Chapter 1, we present a method for a generalized relationship for the lumbosacral joint position. We expand on this in Chapter 2 with a method for estimating a subject-specific model of joint positions from observed marker-based motion data [3]. This optimization-method builds on existing functional methods for joint center recovery. We compare models generated from human subjects during sit-to-stand and a flexion-extension motion against a model generated from an allometrically-scaled measurement. An analysis of the marker residuals finds that the proposed functional models have lower residuals and phase-dependency, indicating a better fit for the analysis of torso kinematics.

Passive Knee Assistance (Chapter 4)

Building on our work in biomechanical modeling, we present a novel passive knee orthotic which provides bilateral knee extension assistance during STS [4]. This device utilizes an elastic element to store energy when the knee is flexed during sitting which is released during standing. By modeling the device and human kinematics and dynamics, we study the effect of single-joint assistance on the control strategy adopted by human subjects. We find that assistance results in a decrease in the human knee torque as well as changes in whole-body biomechanics, notably an increase in the linear momentum of the upper body and a decrease in the anterior excursion of the center of mass. These results indicate that single-joint assistance at the knee has the potential to both facilitate successful STS and positively alter whole-body biomechanics.

Active Upper Limb Assistance (Chapters 5 and 6)

Finally, we present the design, analysis, and validation of a planar robotic manipulandum for upper limb assessment and assistance. Connected at the wrist, the device enables end-effector control of the human arm, operating under position and velocity control as well as force-based admittance control for volitional motion. The device can move the arm through a large workspace with resistive and assistive forces applied along linear or curved trajectories. The mechanical, electrical, and control systems are presented, along with preliminary human subjects tests of reaching trajectories in a control population with case study data from two subjects with upper-limb impairment. We present a novel solution for 3-D upper limb inverse kinematic recovery, utilizing the device constraints. A 2-D model and a simple 6-muscle model of the upper limb are also discussed. Hardware validation and initial human subject results demonstrate device accuracy and functionality. We note differences in the interaction force, trajectory smoothness and velocity, and ability to stabilize between control subjects and subjects with upper-limb impairment .

In Chapter 6, we explore two algorithms for upper-limb assessment with the device detailed in Chapter 5: 1) the exploitation of assistive spring force-fields in tracking an elliptical trajectory and 2) the assessment of strength and coordination through isolated joint motion. These new methods demonstrate additional device functionality.

Chapter 2

Depth Camera Motion Assessment

The study of joint kinematics and dynamics has broad clinical applications including the identification of pathological motions or compensation strategies and the analysis of dynamic stability. High-end motion capture systems, however, are expensive and require dedicated camera spaces with lengthy set-up and data processing commitments. Depth cameras, such as the Microsoft Kinect, provide an inexpensive, marker-free alternative at the sacrifice of joint-position accuracy. In this work, we present a fast framework for adding biomechanical constraints to the joint estimates provided by a depth camera system. We also present a new model for the lower lumbar joint angle. We validate key joint position, angle, and velocity measurements against a gold standard active motion-capture system on ten healthy subjects performing sit-to-stand (STS). Our method showed significant improvement in Mean Absolute Error (MAE) and Intraclass Correlation Coefficients (ICC) for the recovered joint angles and position-based metrics. These improvements suggest that depth cameras can provide an accurate and clinically viable method of rapidly assessing the kinematics and kinetics of the STS action, providing data for further analysis using biomechanical or machine learning methods.

2.1 Overview of Clinical Motion Assessment

Musckuloskeletal disorders of the spine and knee lead to approximately 39 million visits to clinical care facilities each year in the United States [5]. Despite the prevalence of these conditions, there remains a lack of scalable, accessible, and quantitative assessments for whole body biomechanics in clinic. The current clinical gold standard for documenting functional spine impairment is the measurement of Cobb angles in flexion and extension [6, 7], or the Sagittal Vertical Axis (SVA) from radiographs [8]. Such radiographs are inexpensive and offer a precise measurement of vertebral range of motion, but they only assess static postures. During daily functional activities such as sit-to-stand (STS), the strategy used to stand can vary [9, 10, 11], potentially changing the loads experienced by the joints. This results in both inconsistencies in patient care throughout the recovery process and challenges

in understanding the relationship between static observations and functional abilities.

Full-body motion analysis can provide insight into pathological motions and compensation strategies. This analysis is performed in biomechanics labs using gold-standard techniques such as motion capture, force platforms, and surface electromyography. This data can be processed using full-body biomechanics software such as Anybody [12] or OpenSIM [13]. While these systems are a staple in obtaining high resolution kinematic, force, and muscular measurements, their application to regular clinical practice is limited by the time required to setup these measurements, the cost of the equipment, required expertise, and the need for a dedicated motion-capture space.

This has resulted in a dichotomy in analysis, with patients assessed with static measures focused at a particular body segment, while biomechanical labs are able to track and analyze the dynamic motion of the whole-body. Some researchers have explored the use of specialized wearable sensing systems for tracking spine function. Marras developed an exoskeletal tracking system for the lumbar spine to identify motions during occupational tasks, and to identify differences in individuals with low back pain [14, 15]. This system was shown to provide a quantitative kinematic measure of dysfunction based on a specific set of flexion tasks. Taylor and Consmüller developed a system for non-invasive back measurement using flexible strain gauges to measure the curvature of the spine [16, 17]. This system was shown to provide a reliable quantitative assessment of spine shape and range of motion when compared to X-ray. While these systems have been shown to provide good estimates of spine motion and can discriminate between pain and asymptomatic subjects, as they only track spine motion, they are not able to assess changes in full-body motion.

Depth cameras such as the Microsoft Kinect have been used as a marker-less method for assessing function. Unlike the prior motion capture strategies, no hardware (markers, sensors etc.) needs to be attached to the subject. This allows for rapid testing and simplifies clinical deployment. One of the disadvantages of the use of depth cameras is the method used to identify subject landmarks. As no markers are placed on the subject, the location of a subject's joint centres (Fig 2.1) relies on machine learning to label the pixels corresponding to each body segment. The intersection between body segments is then taken to be the estimated joint location [18]. This form of joint centre data from a depth camera is not unique to the Kinect; alternative depth camera sensors (Orbec, Intel RealSense, VicoVR, Depthsense, PMD, SIC), as well as skeletal tracking systems (Nuitrack, OpenNI) are commercially available. As there is no underlying rigid-body model, the estimated joint centres may be biologically inconsistent. This can lead to errors at the ankle, knee, and hip which complicate the use of depth sensors for later analysis [19]. Researchers have found that retro-reflective markers could be used to supplement the recovery process [20]. The addition of these markers adds to the experiment setup time, and sensitivity to the accuracy of marker placement.

An important distinction between this work and the work performed in the computer vision community is the underlying assumptions and goals of the final system. We develop a tool for rapid clinical assessment by applying a biomechanically realistic model to impose constraints on unconstrained estimates of joint position for a controlled task and environ-

ment. In contrast, the problem tackled by a number of these other works are the estimation of human poses across a wide range of tasks while being robust to real-world situations and environments [21].

Two approaches are generally taken when performing pose estimation: creating a skeletal model with a prior on the associated surface geometry, or the generation of a direct map between camera inputs and pose using machine learning. Pavlakos [22] uses convolutional neural networks to estimate the likelihood that a voxel contains a joint. This method resulted in an average 3D joint error of 9.6 cm for the Human3.6M sitting down motion and an average marker reconstruction error of 5 cm. This outperforms a number of other deep learning methods [23, 24] yet still highlights the inherent challenges in joint estimation, particularly in self-occluding tasks such as sitting. This is consistent with the work by Mehta [25] who adopted a similar approach at the pixel level providing a real time (30 fps) system, but with a mean joint position error of 14-15 cm for the sit-down task. While these methods offer a promising method for versatile estimation of human motion, the current joint estimation error is high relative to the surface fitting methods.

Surface fitting methods usually use a simplified approximation of human shape, consisting of scaled cylinders or ellipsoids that are adjusted to a subjects body morphology. This simplified model is then used to estimate pose by relating these volumes to camera depth data. Recent advances have involved the use of Gaussian models to approximate body shape [26], with Ding [27] developing a method that can estimate joint centre position at 20 fps with an associated position error of 3.5 cm. Shuai [28] used spherical harmonic decomposition rather than Gaussians to track subjects with multiple depth cameras. The resulting model exhibited low marker re-projection error, though this error increased in actions with self occlusion such as sitting. Zhang [18] used a full-body skinned mesh model in conjunction with multiple depth cameras and force sensing shoes to estimate kinematic and dynamic state. The resulting system was slow, but accurate with a mean joint error of 3.8 cm at 6 fps. Unfortunately no results were published for any sitting or standing actions, but the authors do state the the system performance did decrease on self-occluding activities. The lower errors and potential for these methods to run in real time suggests that these methods may be suitable for clinical use, but the need for initial calibration of the shape model by performing an explicit calibration motion [26, 18, 27] or through manual labelling [28] detracts from their use. Similarly, the use of multiple cameras suggests a requirement of a dedicated motion capture space where the system can be setup and left undisturbed between sessions.

Contributions

In this chapter, we assesses the feasibility of using a single depth camera as a clinical assessment tool for whole-body kinematic and kinetic assessment. As such, we prioritize:

1. *Accurate anatomical joint center locations and joint angles* which are needed for clinical assessment and future dynamic/musculoskeletal modeling.

2. *Fast computation time* to allow for immediate review by the clinician.

3. *Ease of use* by non-specialists in a clinical environment to perform a rapid motion assessment.

To these aims, we present a simple, fast method for taking any pre-estimated joint center locations, automatically scaling skeletal parameters based on the subject height and recovering kinematic and kinetic measures from the biomechanical model. This system provides accurate, reproducible, and consistent estimates of anatomical joint center locations, with a mean joint position error of 2.63 cm. An additional estimate of L5S1 location is added to the kinematic model allowing for assessment of the lower back, an important site of analysis in clinical and occupational health scenarios. The proposed system is used as a post-processing step on the raw Kinect 2 skeleton, with the mean computation speed of 524 frames per second. This suggests this method can be incorporated into many existing real-time methods without a significant drop in frame-rate. Only a single RGB-D camera is used, allowing for deployment clinical space without the need of a dedicated, calibrated motion capture space. The extraction of kinematic states is performed only requiring the user to specify the subject's height, without any manual model tuning, or joint labeling. The entire time to setup the camera, coach the subject to perform the STS action, data collection, and kinematic recovery takes under 1 minute.

2.2 Rigid-Body Modeling Framework

Rigid-body models are commonly used in biomechanics research to estimate joint kinematics and loading [29, 30, 31, 32, 33]. The mathematical formulations for the kinematics, kinetics, and dynamics of these systems can be taken from the robotics literature [34], providing a versatile method for analyzing arbitrary rigid-body systems. In this work, we present and evaluate two rigid-body models:

1. *Floating pelvis rigid-body model*: constrained body segment lengths. This form of model is typically used in motion analysis, with no environmental constraints.

2. *Fixed-ankle rigid-body model*: constrained body segment lengths and angle-ground contact. As the ankles do not move in the sit-to-stand action, a kinematic constraint on ankle position can be used to determine the effect on the recovered kinematic and kinetic measures.

The models are driven by the raw Kinect shoulder, hip, knee, and ankle joint center positions.

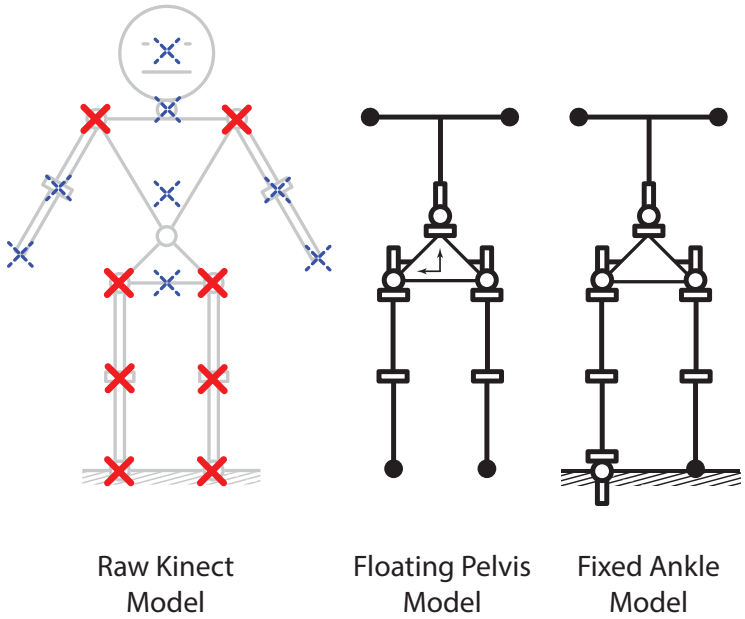

Figure 2.1: The three skeletal models. Left: Raw Kinect Skeleton. The joint centers obtained from the Kinect are shown as crosses. The markers which are not used in this work are shown in the dashed blue. A cartoon outline of a subject is shown for reference. Center: Model I: Floating Pelvis Rigid-body Model. The pelvis is defined as the base link, with three serial chain branches. The sequence of revolute joints are shown as cylinders. Right: Model II: Fixed-ankle Rigid-body Model. The right ankle is fixed to the ground and used as the base link. The revolute joint sequence and segment lengths are the same as in the center figure.

Model I: Floating pelvis rigid-body model

Model structure

The human body is commonly modeled as a *floating* tree system, consisting of a pelvic base-link with serial chains that terminate at the head, hands, and feet [35]. In this work, we study the kinematics of the lower limbs and trunk during STS, neglecting the motion of the arms. We consider a 3D rigid-body model with six segments: (left and right) lower leg, (left and right) upper leg, pelvis, and torso (Figure 2.1). The corresponding joint centers are at the ankle, knee, hip, and lower-lumbar joints. The knee joint is modeled as a cylindrical joint. The ankles, hips, and lower-lumbar (L5S1) joint are modeled as spherical joints with three successive rotations. The order of these rotations is based on relations to common range of motion measures [36].

Segment lengths are determined by recommended height-scaled, sex-specific, allometric relations [37]. These relations provide estimated link length for the upper and lower leg, (l_{UL} and l_{LL}), shoulder width and hip width, (w_S and w_P), the length between the midpoint of the hip centers and L5S1 (h_P) and the length between L5S1 and midpoint of the shoulder

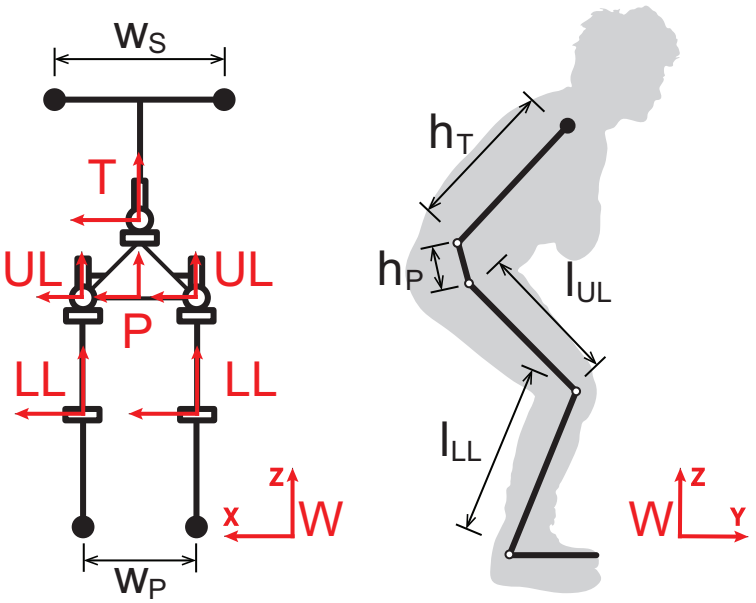

Figure 2.2: The frame labeling and key lengths for the floating pelvis model. Left: Frontal plane view showing shoulder and pelvic width w_S, w_P, coordinate frames for the torso T, pelvis P, the upper and lower legs (UL, LL), and the world frame W. Axes are aligned with the Z axis lying along the primary axis of the segment. Right: Sagittal plane view showing torso and pelvis heights h_T and h_P, and the upper and lower leg lengths, l_{UL} and l_{LL}.

centers (h_T).

Kinematic Formulation

The following mathematical formulation utilizes relative coordinate frame transformations to relate the observed Kinect joint center positions to corresponding joint angles in the rigid-body model. Local coordinate frames are defined in Fig. 2.2. The origin of the base pelvic frame (P) is located at the midpoint between the hip joint centers. All other frame origins are located at the joint center with Z axis pointing along the segment length in the sagittal plane. We represent the position and orientation of the pelvic frame as an X, Y, Z translation ($\boldsymbol{t}_P$), and three sequential rotations about the X, Y, and Z axes (θ_{PX}, θ_{PY}, θ_{PZ}). This is formulated as the homogeneous transformation between the World and Pelvic frames $\boldsymbol{g}_{W,P}$:

$$\boldsymbol{g}_{W,P}\left(\boldsymbol{t}_P, \theta_{PX}, \theta_{PY}, \theta_{PZ}\right) = \begin{bmatrix} \boldsymbol{R}_X \boldsymbol{R}_Y \boldsymbol{R}_Z & \boldsymbol{t}_P \\ \boldsymbol{0} & 1 \end{bmatrix} \tag{2.1}$$

where $\boldsymbol{R}_X$, $\boldsymbol{R}_Y$, and $\boldsymbol{R}_Z$ are the standard rotation matrices about the X, Y, and Z axes, respectively.

The relative transformations between each adjacent segment are defined in the same notation. For example, the transformation between the Pelvis and Torso (T) frames, $\boldsymbol{g}_{P,T}$ can be written:

$$\boldsymbol{g}_{P,T}\left(h_P, \theta_{TX}, \theta_{TY}, \theta_{TZ}\right) = \begin{bmatrix} \boldsymbol{R}_X \boldsymbol{R}_Y \boldsymbol{R}_Z & \begin{bmatrix} 0 \\ 0 \\ h_P \end{bmatrix} \\ \mathbf{0} & 1 \end{bmatrix} \tag{2.2}$$

using the coordinate frames and segment lengths defined in Figure 2.2.

These homogeneous pose matrices are used to estimate the World frame locations of the left and right shoulder centers from their local positions and relative frame transformations:

$$\begin{bmatrix} \boldsymbol{p}_{sho\_left} & \boldsymbol{p}_{sho\_right} \\ 1 & 1 \end{bmatrix} = \boldsymbol{g}_{W,P}\boldsymbol{g}_{P,T} \begin{bmatrix} \begin{bmatrix} -w_S \\ 0 \\ h_T \\ 1 \end{bmatrix} & \begin{bmatrix} +w_S \\ 0 \\ h_T \\ 1 \end{bmatrix} \end{bmatrix} \tag{2.3}$$

This process can be repeated for each joint center to create the observation model for all joints:

$$\begin{bmatrix} \boldsymbol{p}_{sho\_left} \\ \boldsymbol{p}_{sho\_right} \\ \boldsymbol{p}_{hip\_left} \\ \boldsymbol{p}_{hip\_right} \\ \boldsymbol{p}_{knee\_left} \\ \boldsymbol{p}_{knee\_right} \\ \boldsymbol{p}_{ankle\_left} \\ \boldsymbol{p}_{ankle\_right} \end{bmatrix} = h_{obs}\left(\boldsymbol{\eta}, \boldsymbol{X}\right) \tag{2.4}$$

where $\boldsymbol{\eta}$ are the model parameters:

$$\boldsymbol{\eta} = \left[h_P, h_T, l_{UL}, l_{LL}, w_S, w_P\right] \tag{2.5}$$

and $\boldsymbol{X}_I \in \mathbb{R}^{17}$ is the state vector containing the corresponding translations and rotations:

$$\boldsymbol{X}_I = \begin{matrix} [\boldsymbol{t}_P, \boldsymbol{\theta}_P, \boldsymbol{\theta}_T, \boldsymbol{\theta}_{UL\_left}, \boldsymbol{\theta}_{UL\_right}, \\ \theta_{LL\_left}, \theta_{LL\_right}]^T \end{matrix} \tag{2.6}$$

Model II: Rigid-body model with fixed-ankle

Our second rigid-body model introduces an additional constraint by fixing the position of the ankle joint centers. The raw joint centers from the depth camera are not constrained by the ground plane, allowing the ankle to phase through the floor or hover above the floor while the person is standing. During STS, we assume the position of the ankle remains fixed and can be constrained at a fixed position throughout the motion. To implement this constraint, we select the base link to be one of the feet and fix this position to the ground.

The mathematical formulation of the observation model is similar to Section 2.2, with the model starting at one foot and moving up the leg, before branching at the pelvis into the torso and second leg branches.

The state vector $\boldsymbol{X}_{II} \in \mathbb{R}^{14}$ for the fixed ankle model has three fewer states when compared to the floating pelvis model, with the addition of the ipsilateral ankle rotation $\boldsymbol{\theta}_{A\_ipsi} \in \mathbb{R}^3$ and the removal of the pelvis translation and orientation ($\mathbb{R}^6$):

$$\boldsymbol{X}_{II} = \begin{matrix}[\boldsymbol{\theta}_{A\_ipsi}, \theta_{LL\_ipsi}, \boldsymbol{\theta}_{UL\_ipsi}, \boldsymbol{\theta}_{UL\_contra}, \\ \theta_{LL\_contra}, \boldsymbol{\theta}_T]^T\end{matrix} \tag{2.7}$$

where the subscripts *ipsi* and *contra* refer to the ipsilateral and contralateral sides to the base foot.

In our model, the ankle joint center is fixed at a position based on the observed motion. The X and Z coordinates are taken to be the mean observed position throughout the motion. The Y coordinate is fixed to be equal to the mean anterior-posterior position of the knee at a standing posture.

Inverse Kinematics

The kinematic recovery process allows for the estimation of joint angles from observations of joint position. We use two methods of kinematic recovery are: Non-linear Least Squares (NLS) and Unscented Kalman Filtering (UKF).

Non-linear Least Squares (NLS)

The error between the observed joint centers $\boldsymbol{q}$ and the expected joint centers $h_{obs}(\boldsymbol{\eta}, \boldsymbol{X})$ is minimized for each frame k:

$$\min_{\boldsymbol{X}_k} \|\boldsymbol{q}_k - h_{obs}(\boldsymbol{\eta}, \boldsymbol{X}_k)\|_2^2 \tag{2.8}$$

Unscented Kalman Filtering (UKF)

While the NLS method allows for the estimation of the state at each frame, it does not enforce any relationship between sequential states. The UKF balances inaccuracies in measurement with an estimate of the change in state between two successive states [38, 39]. Using the notation for Kalman filters, every observed joint center at frame k can be written:

$$\boldsymbol{q}_k = h_{obs}\left(\boldsymbol{\eta}, \bar{\boldsymbol{X}}_k\right) + \boldsymbol{v}_k \tag{2.9}$$

where $\boldsymbol{v}_k$ is a model of the sensor noise which is taken to be white noise: $\boldsymbol{v}_k \sim \mathcal{N}(0, \boldsymbol{R}_k)$, $\boldsymbol{R}_k$ is the covariance matrix of the Kinect, and the state $\bar{\boldsymbol{X}}_k$ is the true state that underlies each observation.

This observation model is combined with a process model f_{proc} which relates previous estimates of the the true state $\bar{\boldsymbol{X}}_{k-1}$ to the current true state:

$$\bar{\boldsymbol{X}}_k = f_{proc}\left(\bar{\boldsymbol{X}}_{k-1}\right) + \boldsymbol{w}_k \tag{2.10}$$

Figure 2.3: Left: Model used for L5S1 angle estimation. The sagittal location of the shoulder, L5S1, hip, and knee are shown. The included angle at the hip is used to predict the angle at L5S1. Right: sagittal plane model. Joint centers and angle definitions are shown. The definition of the Sagittal Vertical Axis (SVA) metric is also shown.

where $\boldsymbol{w}_k$ is a model of the process noise which is taken to be white noise: $\boldsymbol{w}_k \sim \mathcal{N}(0, \boldsymbol{Q}_k)$. To set limits on the variation of each of the states between samples, the process covariance $\boldsymbol{Q}$ is fixed to be the expected change due to the velocities $\boldsymbol{\sigma}_V$. This allows the process covariance to be written explicitly as the diagonal matrix:

$$\boldsymbol{Q} = \Delta t^2 diag\left(\boldsymbol{\sigma}_V^2\right) \tag{2.11}$$

where Δt is the time between samples, and the process model as the identity matrix.

Planarization

The recovered 3D kinematic data is planarized for analysis of the sagittal kinematics. A plane is fit to the motion of the Kinect joint centers and the data is projected onto the plane. For the symmetric joint centers (ankles, knees, hips, shoulders), the mean of the sagittal plane positions is taken.

Lower lumbar joint (L5S1) estimation

The raw Kinect skeleton provides a single joint center along the spine. We found the position of this joint center to be inconsistent between subjects and within single trials. Due to this unreliability and lack of relation to an anatomical landmark, we disregard the mid-spine marker in our kinematic analysis and consider an alternate method for determining a joint between the hip and shoulders in the sagittal plane.

From marker-based motion capture data, the position of the lower lumbar joint, located at L5S1, can be estimated from pelvic landmarks. An allometric model for the position of

L5S1 in a pelvic frame is presented in Reed et al. [40] Unfortunately, the pelvic orientation is not observable from the Kinect data, so we cannot apply this method.

A model for lumbosacral orientation using knee flexion and trunk inclination is presented by Anderson et al. [41]. In that work, a quadratic model was trained on four subjects in multiple static lifting postures. This model was not assessed on any test data. Using active motion capture data, we tested the Anderson model against the marker-based Reed method. We found that the model did not accurately predict the sacral orientation during STS.

In this work, we present a new regression model for $KHL5$, the angle formed by the knee, hip, and L5S1 joints, driven by KHS, the angle formed by the knees, hips, and shoulders (joints present in the Kinect data). This model assumes that coordination between the hip and L5S1 joints follows a predictable pattern across subjects.

The model is trained using marker-based motion capture data (protocol detailed in Section 2.3). We define the pelvic frame by anterior and posterior superior iliac spine (ASIS and PSIS) markers shown in Fig. 2.5. The location of the L5S1 joint center is based on the model presented in Reed, in which the L5S1 joint center in given a frame defined by the ASIS and pubic symphysis (PS) landmarks. The PS landmark is not possible to mark on a clothed subject or easily observable from motion capture data. Using dry pelvis data from Reynolds, et al. [42], we re-derived the position of the L5S1 joint in the ASIS-PSIS pelvic frame:

$$L5S1 = \begin{bmatrix} 0 & 0 & .11PW \end{bmatrix}^T \tag{2.12}$$

where the pelvic width PW is the distance between the left and right ASIS landmarks. From the observed L5S1 joint center, we compute the joint angles in the sagittal plane. A linear model was fit to the data:

$$KHL5 = \alpha SHK + \beta \tag{2.13}$$

with derived model parameters $\alpha = 0.82$, $\beta = 0.54$ and r-squared 0.9784. This model was trained on four subjects performing STS and tested against six subjects. Each subject performed STS three times. The fitted model and test data are shown in Fig. 2.4. The mean absolute error (MAE) between the predicted and observed $L5S1$ angles was 3.63 ± 1.72 degrees for the test set 4.21 ± 2.73 degrees for the training set.

From Eq. 2.13 and an allometrically scaled pelvic height, h_p, we can express the position of the L5S1 joint center. In our recovery framework, this L5S1 model is used after the kinematic recovery and planarization steps are performed.

2.3 Experimental Validation

The modeling and kinematic recovery methods introduced in Section 2.2 were tested experimentally and validated against marker-based motion capture data on non-clinical subjects.

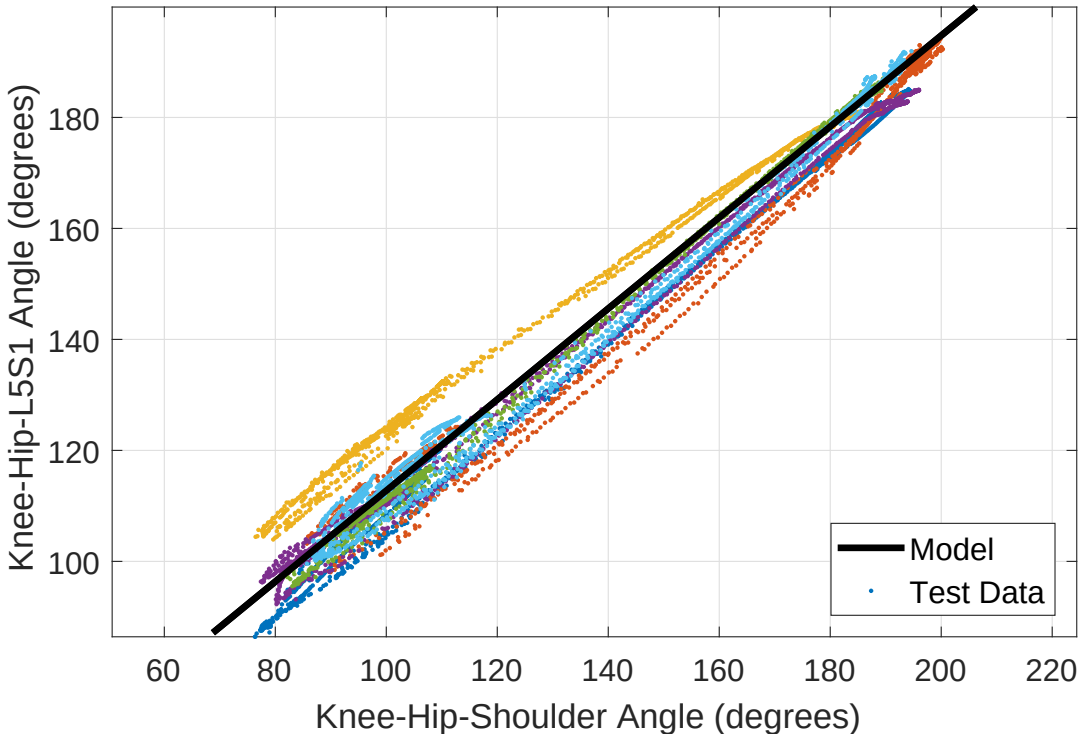

Figure 2.4: Linear regression for L5S1, the angle formed by the knee, hip, and L5S1, joints, from KHS, the angle formed by the knee, hip, and shoulder joints. The model is shown in solid black. Data from the test set of 6 subjects is shown in dotted color.

Experimental Protocol

Ten subjects (3F/7M, age: 30.9 ± 9.6, height: 1.76 ± 0.12 m, mass: 67.4 ± 11.2 kg) were recruited under informed consent (UCSF IRB 16-21015). Subjects wore close fitting exercise clothing (sports bra, exercise shorts). The chair height was adjusted so that the subject's thighs were parallel to the ground, and their knees directly above their ankles during natural sitting. Subjects were asked to perform STS with their arms folded across their chest, hands touching the opposite elbow. The standing action was otherwise non-coached, with subjects performing the action naturally. Three trials, each consisting of three STS, were recorded for each subject.

Active Motion Capture Model

An 8-camera active motion capture system was used in this study to provide a ground-truth estimate of position and orientation of each body segment. Motion data of STS was simultaneously recorded from the Kinect and the motion capture system. The Kinect camera

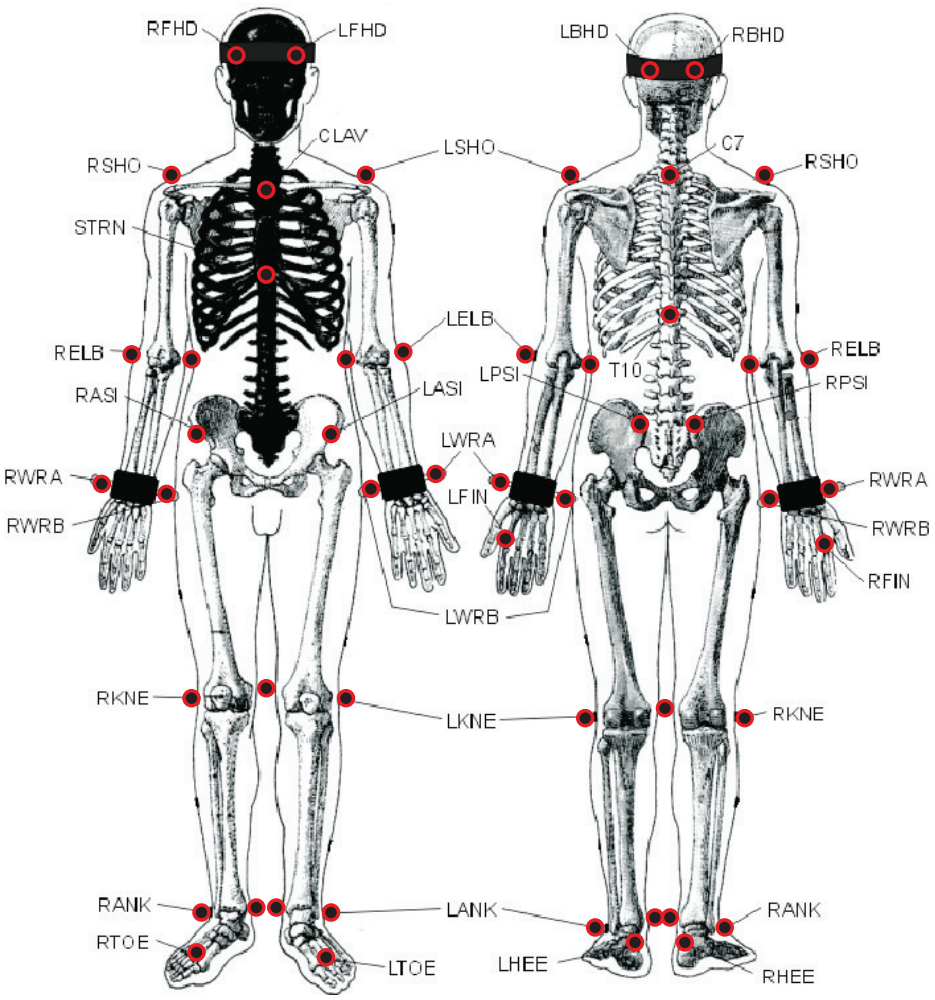

Figure 2.5: Motion capture marker protocol used in this work. Markers (red) are shown superimposed on the standard Plug-in-Gait model.

was located 2.5 meters directly in-front of the subject. The Kinect joint centers were streamed at 30Hz and saved with a UNIX timestamp onto a desktop computer. Each trial consisted of 883 ± 87 frames of Kinect depth data, and 14224 ± 1548 frames of Phasespace data for three successive stand-sit-stand motions (around 30 seconds). The Kinect and motion capture systems were time synchronized using a network time protocol server.

Thirty-two LED markers (Phasespace, San Leandro, CA) were recorded at 480Hz with an associated UNIX timestamp. Kinematic recovery was performed offline in MATLAB. The markers were placed onto the subjects skin using adhesive Velcro® based on the Plug-in-Gait markers set [43] (Figure 2.5). Additional markers were placed on the medial elbow, knee, and ankle positions to allow for estimates of joint center from the medio-lateral marker pairs. In cases where the subject's shorts or sports bra obscured the ASIS, PSIS, or XP landmarks,

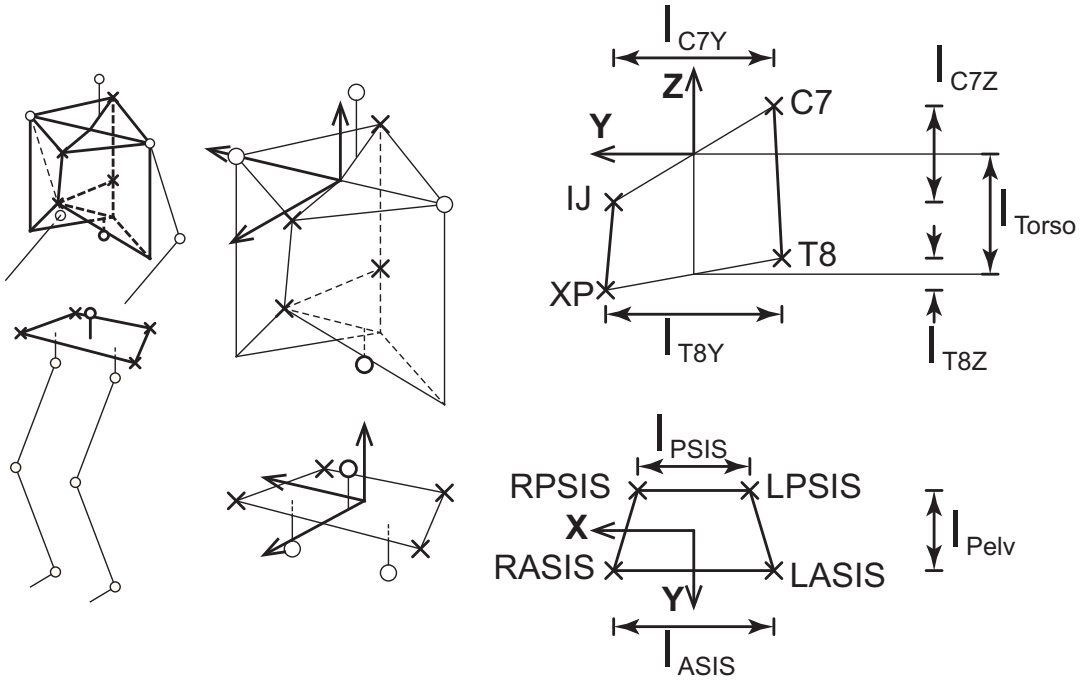

Figure 2.6: Left: Torso and pelvis frames are highlighted, with markers shown as crosses, and joint centers shown as circles. Right: Segment-marker definitions used for NLS recovery. The sagittal view of the torso frame, and caudal view of the pelvis frame are shown. Torso markers were located at the Incisura jugularis sternalis (IJ), Xiphoid Process (XP), and at the C7 and T8 spinous processes which were found during standing. Pelvis markers were located at the right and left Anterior Superior Iliac Spines (ASIS) and Posterior Superior Iliac Spines (PSIS).

a clip was used to secure the marker to the clothes band at the desired landmark.

In addition to the STS protocol, a data set was collected for identifying the functional joint centers for each segment using the Recap2 protocol. Subjects were asked to move each joint through its full range of motion three times, starting with the wrists, elbows, and shoulders, before moving the ankles, knees, and hips. The Recap2 protocol was only used to find the functional centers for the ground truth motion capture model.

NLS (Section 2.2) was used to recover the instantaneous position and orientation of each limb segment in 3D coordinates. Each limb segment was recovered independently without any modeling of the connection between connected limbs.

The rigid-body models used for each each segment are shown in Figure 2.6. The coordinate system is based on Wu [44], with the exception of the pelvis segment where the origin is located at the midpoint of the ASIS and PSIS markers. The labeling of the coordinate axes were also modified to simplify plotting and analysis in MATLAB. NLS was used to estimate the marker positions in the local coordinate frame for each subject.

The joint centers for the ground-truth model were recovered using functional methods (hip and shoulder), and marker-based methods (ankle, knee, and L5S1). Geometric sphere fitting for the hip was chosen based on the recommendation by the ISB [44] and as all subjects were able to move sufficiently [45]. The inter-malleolar point was selected for the ankles from Wu [44], the inter-epicondyle point for the knee [46], and L5S1 from the allometric model described in Section 2.2. The recovered joint-centers were planarized and the relative angles were determined at each frame.

Data Analysis

All data processing was performed on previously stored Kinect 2 data on an Intel i7-5820K processor, with 32GB of RAM running Windows 7 Enterprise. Each trial of three stand-sit-stand actions consisted of roughly 880 frames and was post-processed at 524 ± 140 fps. A graphics card was not used to aid computation.

The joint angles recovered from each method were filtered and numerically differentiated to obtain joint velocity estimates. A first-order, low-pass Butterworth filter at 5 Hz was applied to the active motion capture and both rigid-body Kinect models [47, 48]. The raw kinect data was filtered more heavily, using a first-order low-pass Butterworth filter at 2 Hz. This was to account for significant noise in the raw joint angles leading to unrealistic velocity estimates.

We compute the horizontal distance between the shoulder joint and hip joint centers at each frame as well as its velocity. This is a surrogate for the Sagittal Vertical Axis (SVA), a metric for spinal alignment, measured by static radiographs as the distance between C7 and L5S1 [8]. We also compare recovered peak values for several metrics during STS: flexion and extension velocities of the torso, torso inclination angle, and SVA.

We consider each combination of sensor and model (raw Kinect, floating rigid-body Kinect, fixed-ankle rigid-body Kinect, and active motion capture) to be a different *rater*, allowing for the use of inter-rater reliability assessment methods. Three statistical measures were used to analyze the performance of the raw and rigid-body Kinect models against the active motion capture ground truth:

1. **Absolute Error (MAE)** identifies the raw position or velocity error between methods.

2. **Lin's Concordance Correlation Coefficient (CCC)** assesses inter-rater reliability between methods [49]

3. **Inter-class Correlations Coefficients (ICC)** identifies the absolute agreement (ICC(2,1)) and relative consistency (ICC(3,1)) between methods [50, 51, 52]. ICC values were interpreted as poor (< 0.4), fair ($0.4 - 0.59$), good ($0.6 - 0.74$), and excellent (≥ 0.75) based on the treatment by [53, 54].

2.4 Algorithm Performance

MAE, CCC, and ICC statistics are given for joint center positions (Table 2.1), joint trajectories (Table 2.2), velocity trajectories (Table 2.3), and selected peak metrics (Table 2.4). A representative motion capture trace is shown in Figure 2.7.

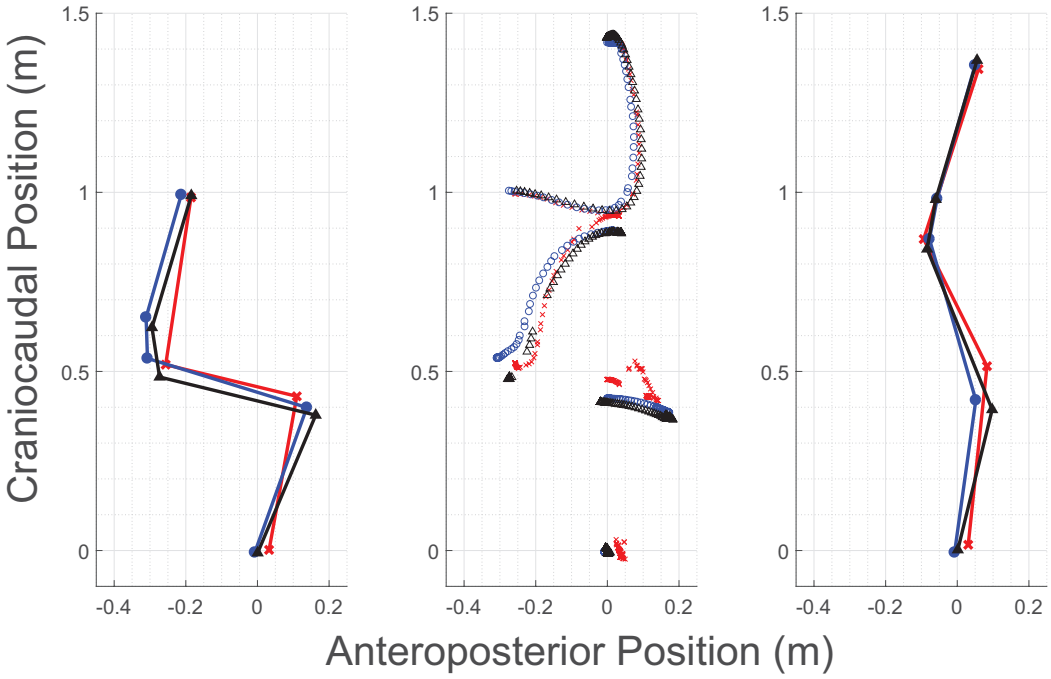

Figure 2.7: Sagittal views of a representative subject performing the STS action. Left: Subject in the seated position. Black triangles outline the subject joint position from the active motion capture system. Red crosses show the raw Kinect 2 joint positions. Blue circles show the estimates from the proposed method. Middle: Motion traces for the entire STS action. L5S1 joints for the Phasespace and proposed models are hidden for clarity. Right: Subject in the near standing position. Note that the raw Kinect 2 skeleton does not provide an estimate for the L5S1 joint center.

Both rigid-body Kinect models (floating and fixed-ankle) achieved significantly lower MAE than the raw Kinect for all joint angle and position measures (Tables 2.1, 2.2). In comparison to the floating model, the fixed-ankle model had significantly less error in the ankle and knee positions and angles, and comparable error in all other measures.

Higher CCC and ICC values indicate greater reliability, relative consistency, and absolute agreement. For the position measures, the fixed-ankle model has higher CCC and ICC values than the raw Kinect in all cases. The floating pelvis model was better than the raw Kinect model, but has poor performance in recovering the ankle positions and angle.

Table 2.1: Inter-rater assessments for estimated joint position. Mean absolute error (MAE), concordance correlation coefficient (CCC) and interclass correlation coefficient (ICC) are given for each skeletal joint. Mean absolute errors are stated as a mean with the standard deviation in parenthesis. Ankle correlation coefficients for the fixed-ankle model are omitted as the ankle position in this model does not vary with time.

		Ankle Position		**Knee Position**		**Hip Position**		**Shoulder Position**	
Measure	**Model**	**X**	**Y**	**X**	**Y**	**X**	**Y**	**X**	**Y**
MAE (cm)	**Raw**	8.66 ± 3.17	2.01 ± 1.69	1.96 ± 1.69	3.57 ± 2.38	1.93 ± 1.95	4.07 ± 2.44	1.98 ± 1.38	4.05 ± 2.04
	Floating	8.31 ± 3.21	1.95 ± 1.59	1.88 ± 1.26	1.46 ± 1.42	2.40 ± 1.69	2.36 ± 1.28	1.71 ± 1.57	2.93 ± 2.11
	Fixed	1.62 ± 0.07	1.97 ± 1.29	1.30 ± 1.08	0.78 ± 0.62	1.98 ± 1.36	2.07 ± 1.27	1.58 ± 1.28	3.08 ± 1.97
CCC	**Raw**	0.24	0.03	0.95	0.62	0.98	0.95	0.98	0.97
	Floating	0.26	0.04	0.96	0.88	0.98	0.98	0.98	0.98
	Fixed	-	-	0.97	0.97	0.99	0.99	0.99	0.98
ICC(2,1)	**Raw**	0.24	0.03	0.95	0.62	0.98	0.95	0.98	0.97
	Floating	0.26	0.04	0.96	0.88	0.98	0.98	0.98	0.98
	Fixed	-	-	0.97	0.97	0.99	0.99	0.99	0.98
ICC(3,1)	**Raw**	0.72	0.05	0.95	0.62	0.99	0.99	0.99	0.99
	Floating	0.73	0.05	0.96	0.91	0.99	0.99	0.99	0.99
	Fixed	-	-	0.97	0.97	0.99	0.99	0.99	0.99

Table 2.2: Inter-rater assessments for angle and positions measures. Mean absolute errors (MAE), concordance correlation coefficient (CCC), and interclass correlation coefficients (ICC) are given for selected trajectory measures. Mean absolute errors are stated as mean with the standard deviation in parenthesis. Asterisks indicate that the absolute errors were significantly different from the raw Kinect model at the 5% (*) and 1% (**) significance levels. Correlation coefficients are given with the 95% confidence interval in parenthesis.

Measure	Model	Ankle Angle (deg)	Knee Angle (deg)	Hip Angle (deg)	L5S1 Angle (deg)	Trunk Angle (deg)	SVA Position (cm)
MAE	**Raw**	12.6 (4.9)	9.4 (6.4)	11.1 (7.7)	-	3.9 (2.4)	3.4 (2.2)
	Floating	11.5 (5.0)**	9.0 (5.5)**	5.6 (4.7)**	6.4 (4.4)	3.6 (2.4)**	2.6 (1.7)**
	Fixed	4.2 (2.6)**	5.2 (3.5)**	5.8 (5.4)**	6.1 (4.1)	3.5 (2.4)**	2.6 (1.7)**
CCC	**Raw**	0.43 (0.42 - 0.44)	0.97 (0.96 - 0.97)	0.95 (0.95 - 0.95)	-	0.93 (0.93 - 0.94)	0.93 (0.93 - 0.93)
	Floating	0.43 (0.42 - 0.44)	0.97 (0.97 -0.97)	0.98 (0.98 - 0.98)	0.79 (0.78 - 0.80)	0.95 (0.95 - 0.95)	0.96 (0.96 - 0.96)
	Fixed	0.82 (0.81 - 0.83)	0.99 (0.99 - 0.99)	0.98 0.97 - 0.98)	0.81 (0.80 - 0.81)	0.95 (0.95 - 0.95)	0.96 (0.96 - 0.96)
ICC(2,1)	**Raw**	0.43 (0.00 - 0.77)	0.97 (0.76 - 0.99)	0.95 (0.91 - 0.97)	-	0.93 (0.71 - 0.97)	0.93 (0.75 - 0.97)
	Floating	0.43 (0.00 - 0.76)	0.97 (0.46 - 0.99)	0.98 (0.96 - 0.99)	0.79 (0.71 - 0.84)	0.95 (0.71 - 0.98)	0.96 (0.89 - 0.98)
	Fixed	0.82 (0.78 - 0.85)	0.99 (0.99 - 0.99)	0.98 (0.97 - 0.98)	0.81 (0.75 - 0.85)	0.95 (0.70 - 0.98)	0.96 (0.88 - 0.98)
ICC(3,1)	**Raw**	0.85 (0.84 - 0.86)	0.98 (0.98 - 0.98)	0.96 (0.96 - 0.96)	-	0.96 (0.96 - 0.96)	0.96 (0.95 - 0.96)
	Floating	0.83 (0.82 - 0.84)	0.99 (0.99 - 0.99)	0.98 (0.98 - 0.98)	0.81 (0.80-0.82)	0.97 (0.97 - 0.97)	0.97 (0.97 - 0.97)
	Fixed	0.83 (0.83 - 0.84)	0.99 (0.99 - 0.99)	0.98 (0.98 - 0.98)	0.82 (0.81 - 0.83)	0.97 (0.97 - 0.97)	0.97 (0.97 - 0.97)

Table 2.3: Inter-rater assessments for angular and linear velocity measures. Mean absolute errors (MAE), concordance correlation coefficient (CCC), and interclass correlation coefficients (ICC) are given for selected trajectory measures. Mean absolute errors are stated as mean with the standard deviation in parenthesis. Asterisks indicate that the absolute errors were significantly different from the raw Kinect model at the 5% (*) and 1% (**) significance levels. Correlation coefficients are given with the 95% confidence interval in parenthesis.

Measure	Model	Ankle Angular Velocity (deg/s)	Knee Angular Velocity (deg/s)	Hip Angular Velocity (deg/s)	L5S1 Angular Velocity (deg/s)	Trunk Angular Velocity (deg/s)	SVA Velocity (cm/s)
MAE	**Raw**	7.5 (7.3)	13.0 (14.0)	16.7 (17.0)	-	8.0 (7.9)	7.2 (7.0)
	Float	7.9 (9.0)*	11.3 (12.1)**	12.0 (12.6)**	9.9 (10.1)	8.1 (9.4)	6.8 (6.7)**
	Fixed	6.5 (7.2)**	13.5 (15.0)	13.7 (13.8)**	10.1 (10.0)	8.8 (9.0)**	7.1 (6.4)
CCC	**Raw**	0.80 (0.79 - 0.81)	0.93 (0.93 - 0.93)	0.93 (0.93 - 0.93)	-	0.95 (0.95 - 0.95)	0.95 (0.94 - 0.95)
	Float	0.73 (0.72 - 0.75)	0.94 (0.94 - 0.95)	0.95 (0.95 - 0.96)	0.69 (0.68 - 0.70)	0.95 (0.95 - 0.95)	0.95 (0.95 - 0.96)
	Fixed	0.87 (0.86 - 0.87)	0.93 (0.92 - 0.93)	0.94 (0.94 - 0.95)	0.70 (0.69 -0.72)	0.95 (0.95 - 0.95)	0.95 (0.95 - 0.96))
ICC(2,1)	**Raw**	0.80 (0.79 - 0.81)	0.93 (0.93 - 0.93)	0.93 (0.93 - 0.93)	-	0.95 (0.95 - 0.95)	0.95 (0.94 - 0.95)
	Float	0.73 (0.72 - 0.75)	0.94 (0.94 - 0.95)	0.95 (0.95 - 0.96)	0.69 (0.68 - 0.71)	0.95 (0.95 - 0.95)	0.95 (0.95 - 0.96)
	Fixed	0.87 (0.86 - 0.87)	0.93 (0.92 - 0.93)	0.94 (0.94 - 0.95)	0.70 (0.68 - 0.72)	0.95 (0.95 - 0.95)	0.95 (0.95 - 0.96)
ICC(3,1)	**Raw**	0.80 (0.79 0.81)	0.93 (0.93 - 0.93)	0.94 (0.94 - 0.94)	-	0.95 (0.95 - 0.95)	0.95 (0.94 - 0.95)
	Float	0.73 (0.72 - 0.75)	0.94 (0.94 - 0.95)	0.95 (0.95 - 0.96)	0.69 (0.68 - 0.71)	0.95 (0.95 - 0.95)	0.95 (0.95 - 0.96)
	Fixed	0.87 (0.86 - 0.88)	0.93 (0.92 - 0.93)	0.95 (0.94 - 0.95)	0.70 (0.69 - 0.72)	0.95 (0.95 - 0.95)	0.95 (0.95 - 0.96)

Table 2.4: Inter-rater assessments for peak measures. The angle at L5S1 is modeled using the author's proposed method. Mean absolute errors (MAE), concordance correlation coefficient (CCC), and interclass correlation coefficients (ICC) are given for selected trajectory measures. Mean Absolute Errors are stated as mean with the standard deviation in parenthesis. Asterisks indicate that the absolute errors were significantly different from the raw Kinect model at the 5% (*) and 1% (**) significance levels. Correlation coefficients are given with the 95% confidence interval in parenthesis.

Measure	Model	Peak Trunk Flexion Angle (deg)	Peak SVA Position (cm)	Peak Trunk Flexion Angular Velocity (deg/s)	Peak Trunk Extension Angular Velocity (deg/s)
Typical Value	**Mocap**	61.8 (4.9)	24.1 (3.6)	73.3 (10.0)	55.4 (10.8)
	Raw	60.4 (3.5)	25.1 (2.9)	58.8 (11.0)	50.5 (7.2)
	Floating	57.6 (6.2)	24.5 (4.1)	76.3 (17.0)	65.1 (15.4)
	Fixed	57.2 (6.2)	24.9 (4.0)	75.7 (16.3)	67.7 (14.1)
MAE	**Raw**	3.1 (2.5)	2.9 (2.4)	16.7 (9.4)	6.1 (5.3)
	Floating	4.2 (3.1)**	1.9 (1.6)**	11.1 (9.9)**	8.8 (12.7)**
	Fixed	4.6 (3.1)**	1.9 (1.7)**	8.2 (11.4)**	12.6 (7.5)**
CCC	**Raw**	0.58 (0.44 - 0.69)	0.35 (0.17 - 0.51)	0.15 (0.04 - 0.25)	0.66 (0.56 - 0.74)
	Floating	0.65 (0.55 - 0.73)	0.79 (0.70 -0.85)	0.40 (0.24 - 0.53)	0.51 (0.38 - 0.61)
	Fixed	0.63 (0.54 - 0.71)	0.78 (0.69 - 0.85)	0.47 (0.31 - 0.59)	0.54 (0.43 - 0.63)
ICC(2,1)	**Raw**	0.58 (0.40 - 0.71)	0.36 (0.16 - 0.52)	0.15 (-0.07 - 0.36)	0.66 (0.27 - 0.82)
	Floating	0.65 (-0.03 - 0.86)	0.79 (0.70 - 0.86)	0.40 (0.21 - 0.56)	0.51 (0.08 - 0.73)
	Fixed	0.64 (-0.01 - 0.87)	0.78 (0.68 - 0.86)	0.47 (0.29 - 0.62)	0.54 (-0.09 - 0.82)
ICC(3,1)	**Raw**	0.61 (0.46 - 0.73)	0.96 (0.95 - 0.96)	0.28 (0.09 - 0.46)	0.75 (0.64 - 0.83)
	Floating	0.83 (0.75 - 0.88)	0.97 (0.97 - 0.97)	0.41 (0.22 - 0.57)	0.64 (0.50 - 0.75)
	Fixed	0.84 (0.77 - 0.89)	0.80 (0.71 - 0.86)	0.47 (0.30 - 0.62)	0.79 (0.70 - 0.86)

The MAE of the velocity trajectories shown in Table 2.3 are comparable between the raw, floating, and fixed-ankle models. This similarity in performance was also seen in the CCC and ICC values, with the knee, hip, trunk and SVA velocities showing high agreement and repeatability for all methods. The estimated ankle velocities had lower ICC and CC values across the methods, but showed an improvement using the fixed-ankle model. The recovery of the angles and angular velocities at L5S1 were consistently worse than that of the other joints, classified as good-excellent instead of excellent.

The peak measures in Table 2.4 show the performance of the different methods in extracting candidate performance metrics from the trajectory data. The MAE for the floating and fixed-ankle models are significantly lower than the raw Kinect for the peak SVA and peak flexion velocity, but significantly higher for the flexion angle, and the extension angular velocity. The CCC and ICC values for the fixed-ankle model show fair-excellent performance, compared to the raw Kinect which had poor performance measuring the peak SVA and trunk flexion velocity. The peak trunk flexion angle and extension velocity were found to be consistent (ICC(3,1): excellent), but with lower agreement (ICC(2,1): good/fair).

2.5 Discussion

The introduction of segment length constraints in the floating rigid-body model resulted in significant improvement in all joint position and angle measures. The fixed-ankle model, which combined segment length constraints with an ankle contact constraint, further improved the recovery of the ankle and knee joint angles. Accurate lower-limb recovery is essential for performing whole-body dynamic analysis. This model had excellent estimates of joint position and velocity trajectories when compared to the gold-standard motion capture. The peak metrics associated with the position data were found to provide good to excellent agreement and consistency. These improvements are also seen peak metrics obtained from the floating-pelvis model, though the MAE, CCC, and ICC values for the ankle, knee, and hip are comparable or worse than the fixed-ankle model. In contrast, the raw Kinect had higher MAE in recovered joint angles, notably at the ankle, knee, and hip, and poor-fair agreement for the peak position metrics.

The mean joint position error of 2.63 cm (in the sagittal plane) is substantially lower than those seen in more generalized camera methods. In comparison to the joint errors on the Human3.6m data set presented by Mehta [25], the lowest mean joint position error for the sit-down action was found to be 10.4 cm reported by Pavlakos [22]. The approach proposed by Shuai [28] for the used of multiple depth cameras resulted in marker residuals of approximately 3.5 cm for the sit down then stand up action (MHAD action 9 [55]), but requires the use of three synchronized Kinect 2 cameras.

The trunk angle trajectory and peak trunk flexion angle were found to be consistent (ICC(3,1): 0.95, 0.84) for the fixed-ankle model, but with lower absolute agreements (ICC(2,1): 0.95, 0.64). This indicates that there may be a consistent offset between the motion-capture and the Kinect models. The MAE for these values suggest that there is an approximately 4 degree offset in the trunk angles between the active motion capture model and the fixed-ankle model. This offset may be based on the difference in the location of the shoulder center between the motion capture and the Kinect models. The motion capture model defines the shoulder as the functional center of the arm which is then fixed in the torso frame. This functional center was estimated from the subject performing arm *windmills* in the sagittal plane. This motion also includes motion of the scapula, translating the location of the glenohumeral center (GHC). The estimated shoulder center is likely to be in the center of that space. During the sit to stand action, the subject's arms were placed across their chest, with their hands touching the opposite elbows. This action protracts the scapula, moving the GHC anteriorly. The Kinect however is estimating the location of the GHC for each frame accounting for this new location for the GHC.

The error in angular velocities were comparable across the raw Kinect and rigid-body methods. To obtain the velocities, the raw Kinect position data was heavily filtered. There is a notable trade-off in the performance of the models between the joint angle and angular velocity MAEs. In particular, the angular velocities of the floating-pelvis model outperforms the fixed-ankle model for all joints other than the ankle. As the floating-model is not constrained the model is able to respond rapidly to changes in observed position, resulting

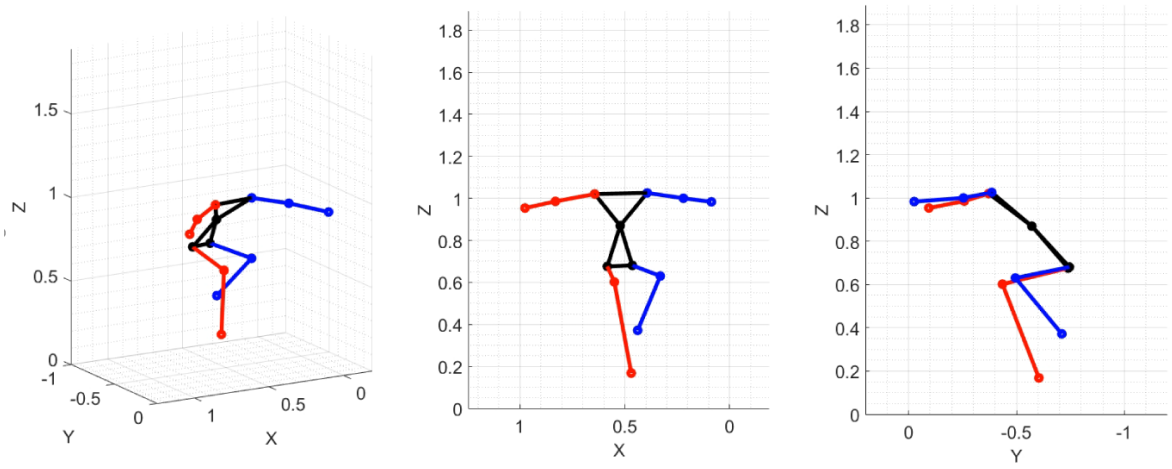

Figure 2.8: Example visualization of the single-leg squat motion as recorded with the depth camera and filtered with the rigid-body algorithm.

in lower velocity errors. In contrast, these rapid changes are moderated by the constraints imposed by the fixed-ankle model.

The improved position accuracy from the models, combined with accurate angular velocities suggests the suitability of using the fixed-ankle model for further dynamic analysis. This is not possible using the original raw Kinect data due to the inaccurate joint center positions and corresponding angle errors.

It is important to note that this study was conducted with the person directly in front of the depth camera. From a previous study [56], the authors did find that there is an increase in estimated joint center position when the camera is set at increasing angles from the subject. These joint center errors were found to be higher in the lower limbs (+1.5 cm) in both standing and sitting activities, with higher error seen in the limb distal to the camera. While this issue could arise in clinic, especially in cases where the system may be rapidly set-up, the 30 degree offset used in the study is larger than a reasonably expected set-up error. Furthermore, the addition of an constraints to the ankle may improve recovery performance in the lower limbs.

2.6 Extension to Single-leg Squat

The single leg squat (SLS) test is useful for clinical assessment of strength, flexibility, balance and motor control. In contrast to STS, which can be modeled in the sagittal place, accurate measurements of 3-D joint kinematics are necessary for detailed analysis of the motion. Utilizing the methods described in Section 2.2, we assess the utility of a depth sensor in capturing knee kinematics during SLS by direct comparison with a ground-truth motion capture system. The single-leg squat motion is challenging due to potential occlusion of the

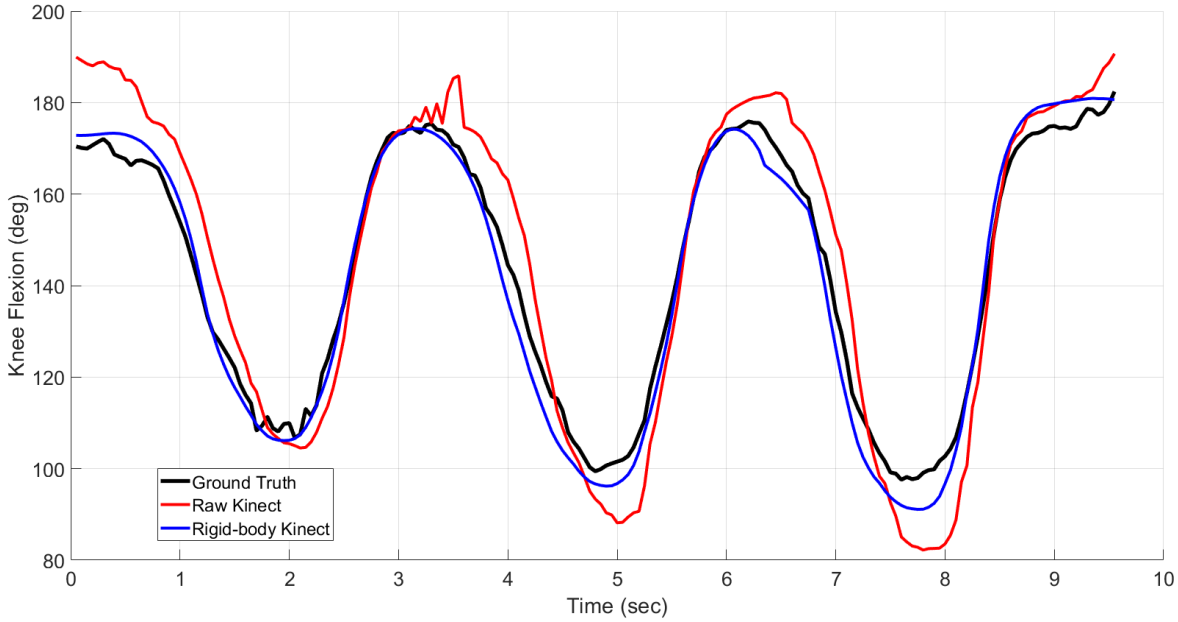

Figure 2.9: Example knee flexion angles (deg) recovered from the ground truth motion capture system (black), raw Kinect depth camera (red), rigid-body algorithm (blue).

base (standing leg) by the leg off the ground. This can result in additional inaccuracies and noise in the raw data from the Kinect.

Time-synchronized squat data were simultaneously recorded by a single depth camera (Kinect 2, 30Hz) and an active marker motion capture system (Phasespace, 480 Hz). Forty-nine LED markers were placed on anatomical landmarks, following a modified Plugin-Gait marker protocol. Functional joint centers were computed from the active marker trajectories, providing a ground truth measurement of joint angles. Subject-specific limb lengths were estimated using height-scaled allometry. Six healthy subjects (age 29.5 ± 6.3 years, 1F, 5M) were recruited under IRB approval. Each performed three trials consisting of three single-leg-squats on each foot (108 total motions). Subjects were instructed to squat as low as comfortably possible at their own pace.

Figure 2.8 shows a representative still image of the 3D skeleton during the SLS motion. Peak knee flexion and frontal-plane knee position (relative to a pelvic coordinate system) were evaluated. The knee displacement was measured along an axis running through the hip joint centers. The error of the raw and filtered Kinect data was computed against the ground truth. The proposed method shows improvement in the peak knee flexion error: filtered (5.38 ± 5.31 degrees) vs raw (9.57 ± 5.70 degrees), and comparable frontal plane displacement error: filtered (2.61 ± 2.17 cm), raw (2.80 ± 2.34 cm). A comparison of the knee flexion angles for a representative trial is shown in Figure 2.9. These results demonstrate the efficacy of using low-cost depth cameras for the clinical analysis of the SLS motion. The

proposed method of applying rigid-body constraints has been shown to improve the accuracy of the recovered 3D motion metrics.

2.7 Chapter Summary

In this chapter, we presented a framework for improving kinematic recovery from depth-camera data through the use of rigid-body modeling. We validated the performance of our proposed method and raw Kinect data through comparison against a ground-truth active motion capture system on the sit-to-stand and single-leg-squat motions. The use of a rigid-body model and contact constraints significantly were found to improve the accuracy of joint kinematics and metrics of clinical interest. This framework enhances the utility of a depth-camera for quantitative motion analysis with accurate kinematic and kinetic measurements allow for the expansion to dynamic analysis of joint torques. The proposed system has low cost, space, and time requirements and can be easily deployed in clinic, with the total time to setup, collect, and process the motion data taking less than a minute. While this framework is validated against specific motions of clinical interest with a single depth-camera system, the method presented is extensible to additional actions and sensing devices.

Chapter 3

Recovering a Rigid-Body Model of the Spine

A representative model is necessary for the analysis of spine kinematics and dynamics during motion. Existing models, based on stationary imaging or cadaveric data, may not be accurate through the full range of spinal motion or for clinical populations. In this chapter, we propose a functional method for estimating subject-specific spinal joint centers, generating a one-joint or two-joint kinematic model of the spine. These models are driven by the motion of the thorax and pelvis as observed by eight surface landmarks. We apply this method to experimental data from ten subjects performing flexion/extension and sit-to-stand motions. The recovered functional models are assessed against an allometric model though the analysis of marker residuals. We found that the functional models provide lower residuals than the allometric methods. Between the functional models, the two-joint model provided lower residuals with less sensitivity to the training action, while the one-joint model should be trained on the motion of interest.

3.1 Torso Models in Motion Assessment

The biomechanical modeling process allows for analysis of movement through the creation and use of representative models. These models can be relatively simple *template* models, designed to describe key behaviors, or more detailed *anchor* models [57]. Rigid body models are often used for the analysis of human movement, allowing for the estimation of joint angles and loads from observed motions. To account for individual variation, joint center locations and segment lengths may be adjusted with *allometric* or *functional* methods.

Allometric methods scale key dimensions and inertias by measurable lengths and masses, typically the standing height and mass of the subject [31]. These methods allow for the estimation of internal joint centers from external anatomical landmarks. These relationships may be based on imaging studies on living subjects or from the measurement of dry cadaver specimens [42, 58, 59]. While these methods provide a powerful tool for creating rigid body

models, the underlying scaling assumptions may not hold for clinical populations or capture the full variations between individual.

Functional methods estimate the location of joint centers by performing spherical (or circular) fits on observed motion capture data. These methods are well suited for the recovery of joints with a large range of motion that can be appropriately simplified to a spherical or cylindrical surface such as the hip [46, 60] and glenohumeral rotation of the shoulder [61]. The use of functional methods for these joints has been shown to provide higher accuracy estimates of joint centers when compared to allometric methods [60]. However, functional methods have been limited to joints that can be independently excited such as the upper and lower limbs.

Spinal joint centers are difficult to identify due to the compound motion of multiple vertebrae, relatively low intervertebral ranges of motion, and difficulty obtaining ground-truth values. In the analysis of motion, the torso is often modeled as a rigid body with a single lumbosacral joint [62], with a number of models omitting spinal motion entirely [63]. An allometric estimate of the lumbosacral joint from pelvic markers is presented in the study by Reed et al. [40], and a predictive relationship based on knee and torso angles is presented in the study by Anderson et al. [64]. More complex regression models of individual intervertebral joint locations from surface data have been presented. However, these methods are limited by small datasets or only applicable to a single posture [58, 65].

Contributions

In this chapter, we present a functional method for generating a subject-specific model of the spine. Joint centers are derived for a one-joint and two-joint spine model that best describes the motion of the pelvis and thorax as observed from eight surface landmarks. These simplified models allow for the application of the functional method and for subsequent work in dynamic modeling. We compare functional models derived from flexion-extension (FE) and sit-to-stand (STS) actions to an allometric model. The STS action is both an activity of daily living as well as a well studied biomechanical and clinical test for motion and stability in healthy and clinical populations [10, 47]. The FE action, another clinical test, was chosen to maximize the observed range of spinal motion.

3.2 Recovering a Functional Spine Model

This section outlines the proposed functional method to identify rigid-body model parameters from motion capture data. The algorithm consists of the following steps:

A) Identification of marker coordinates in local pelvic and thoracic frames from marker trajectories measured in the world frame

B) Transformation of thoracic markers to the pelvic frame using the recovered pelvis configuration.

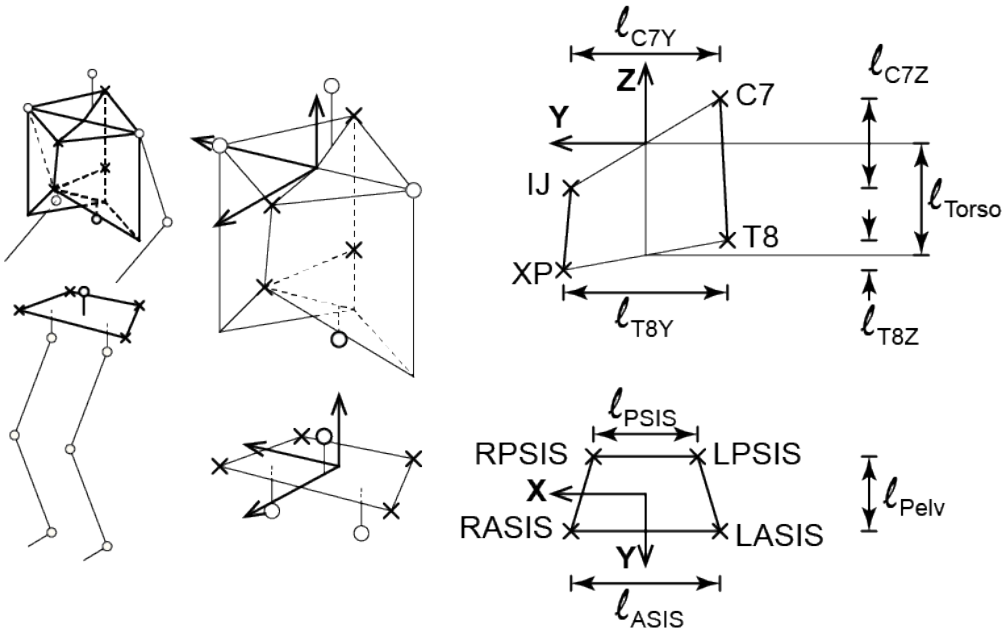

Figure 3.1: Definition of pelvic (P) and thoracic (T) coordinate systems. Left: 3D cartoon of a standing figure with pelvis and torso frames highlighted. Middle: Isolated 3D cartoon of pelvis and torso. Right: Flattened pelvic and thoracic frames with anatomical landmarks, coordinate definitions, and segment lengths.

C) Identification of rigid-body model parameters which define the functional joint centers and segment lengths

Local marker parameter identification

We consider the motion of the pelvis and upper thorax, assuming the thorax behaves as a single rigid-body above T8 [58]. Each local coordinate system is defined by four motion capture markers at anatomical landmarks (Figure 3.1). The pelvic coordinate system is defined by left and right ASIS (anterior superior iliac spines) and left and right PSIS (posterior superior iliac spines) [44]. The thoracic coordinate system is defined by C7, T8, IJ (Incisura Jugularis), and XP (xiphoid process) [66]. Minor modifications were made to the origins of these coordinate systems to reduce the effect of individual marker error through the addition of the fourth (redundant) marker.

The pelvic markers $\boldsymbol{q}$ have fixed coordinates $\boldsymbol{q}_P$ in the local pelvic (P) frame. Likewise, the thoracic markers $\boldsymbol{r}$ have fixed coordinates $\boldsymbol{r}_T$ in the local thoracic (T) frame. Local marker coordinates are parameterized by $\boldsymbol{\phi}_P$ and $\boldsymbol{\phi}_T$, vectors of length parameters illustrated in Figure 3.1. Given local coordinates $\boldsymbol{q}_P(\boldsymbol{\phi}_P)$, we can express the coordinates of the marker in the world (W) frame, $\boldsymbol{q}_W(t)$:

$$\boldsymbol{q}_W(t) = \boldsymbol{g}_{WP}(t)\boldsymbol{q}_P(\boldsymbol{\phi}_P) \tag{3.1}$$

where $\boldsymbol{g}_{WP}(t)$ is the rigid body transformation between the world and pelvic frames at time t [67]. The transformation is defined by a linear translation and rotation:

$$\boldsymbol{g}_{WP}(t) = \begin{bmatrix} \boldsymbol{R}_{WP}(t) & \boldsymbol{p}_{WP}(t) \\ \mathbf{0} & 1 \end{bmatrix} \tag{3.2}$$

where $\boldsymbol{R}_{WP}(t)$ is a rotation matrix, and $\boldsymbol{p}_{WP}(t)$ are the coordinates of the center of rotation as viewed in the W frame.

The rigid-body transform can be described by the translation $\boldsymbol{p}_{WP}$ and scaled axis of rotation $\boldsymbol{\omega}_{WP}$ written as the vector $\boldsymbol{\xi} \in \mathbb{R}^6$ where $\boldsymbol{\xi} = [\boldsymbol{\omega}_{WP}, \boldsymbol{p}_{WP}]^T$ which gives the transformation:

$$\boldsymbol{g}_{WP}(\boldsymbol{\xi}) = \begin{bmatrix} e^{\hat{\omega}_{WP}} & \boldsymbol{p}_{WP} \\ \mathbf{0} & 1 \end{bmatrix}. \tag{3.3}$$

The best fit local marker parameters $\boldsymbol{\phi}_P$ and the corresponding states $\boldsymbol{\xi}$ are recovered from n samples of observed marker positions in the world frame. This can be written as the optimization:

$$\min_{\boldsymbol{\phi}_P, \boldsymbol{\xi}_1 \cdots \boldsymbol{\xi}_n} \sum_{i=1}^{n} \left\| \boldsymbol{g}_{WP}(\boldsymbol{\xi}_P(i))\boldsymbol{q}_P(\boldsymbol{\phi}_P) - \boldsymbol{q}_W(i) \right\| \tag{3.4}$$

where $\boldsymbol{q}_W(i)$ are the observed markers in world coordinates and $\boldsymbol{\xi}_P(i)$ is the corresponding state at the ith sample.

These parameters were optimized over 20 sample frames from the flexion-extension motion to find the best fit local marker coordinates, using the non-linear least squares (NLS) solver in MATLAB, obtaining the marker parameters $\boldsymbol{\phi}_p$ and local marker coordinates, $\boldsymbol{q}_P$. This process was repeated to determine the local thoracic marker positions $\boldsymbol{r}_T$. This optimization was performed for each subject, obtaining subject-specific pelvis and torso local marker locations.

Transformation to the local pelvic frame

During the flexion-extension and sit to stand motions, a significant portion of the observed rotation is due to motion of the pelvis. To isolate the motion of the spine, we transform the observed world-frame motion of the thoracic markers $\boldsymbol{r}_W$ into pelvic frame coordinates $\boldsymbol{r}_P$ shown in Figure 3.2. The configuration of the pelvis $\boldsymbol{g}_{WP}$ at each frame i is recovered using the fixed marker model identified in Section II-A:

$$\min_{\boldsymbol{\xi}_i} \left\| \boldsymbol{g}_{WP}(\boldsymbol{\xi}(i)\boldsymbol{q}_P) - \boldsymbol{q}_W) \right\|. \tag{3.5}$$

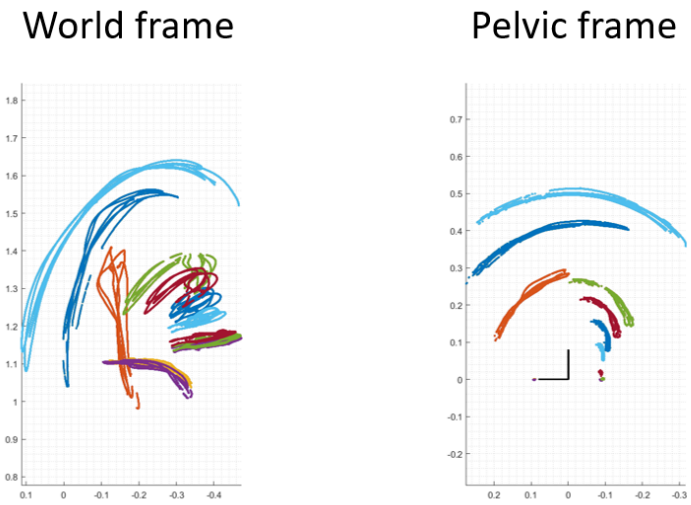

Figure 3.2: Visualization of transformation of the motion capture markers from the World frame (left) into the recovered Pelvic frame (right). Data from the eight markers used in the model recovery algorithm as well as three additional markes on the lumbar spine is shown.

This allows for the transformation of the thoracic markers from the world frame into the pelvic frame:

$$\boldsymbol{r}_P = \boldsymbol{g}_{WP}^{-1}(\boldsymbol{\xi}(i))\boldsymbol{r}_W(i). \tag{3.6}$$

Spine model parameter identification

We consider a one-joint and two-joint rigid-body model of the spine (Figure 3.3). The motion of the torso during FE and STS actions are assumed to be constrained to the sagittal plane, allowing the joints to be simplified to rotations about the x-axis. The one-joint model contains a single joint center JC between the pelvic and thoracic frames. The intermediate coordinate frame J is defined with origin at the JC. The length parameter l_{JT} is the distance between the JC and the origin of the thoracic frame. The forward kinematics of the one-joint model can be expressed as a series of relative rigid-body transforms:

$$\begin{aligned} \boldsymbol{g}_{PT} &= \boldsymbol{g}_{PJ}\boldsymbol{g}_{JT} \\ &= \begin{bmatrix} \boldsymbol{R}_x\theta & JC_P \\ \boldsymbol{0} & 1 \end{bmatrix} \begin{bmatrix} \boldsymbol{I}_3 & p_{JT} \\ \boldsymbol{0} & 1 \end{bmatrix} \end{aligned} \tag{3.7}$$

where R_x is the standard rotation matrix about the x-axis, θ is the angle of rotation at the JC, JC_P is the location of the JC in pelvic frame coordinates, and $p_{JT} = \begin{bmatrix} 0 & 0 & l_{JT} \end{bmatrix}^T$ is the fixed translation from the joint center to the thoracic frame.

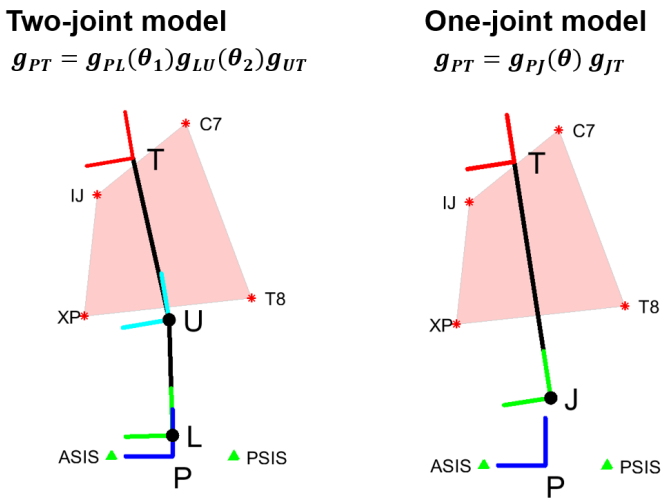

Figure 3.3: Rigid-body spine models in the pelvic (P) coordinate system. Local coordinate frames and surface markers are labeled.

The two-joint model contains a lower joint center LJC fixed in the pelvic frame and an upper joint center UJC fixed in the thoracic frame. The intermediate coordinate frames L and U are defined with origins at the LJC and the UJC, respectively. The length parameter l_{LU} is the distance between the LJC and the UJC. The forward kinematics of two-joint model can be expressed as a series of relative rigid-body transforms:

$$\begin{aligned} \boldsymbol{g}_{PT} &= \boldsymbol{g}_{PL}\boldsymbol{g}_{LU}\boldsymbol{g}_{UT} \\ &= \begin{bmatrix} \boldsymbol{R}_x\theta_1 & LJ_P \\ \mathbf{0} & 1 \end{bmatrix} \begin{bmatrix} \boldsymbol{R}_x\theta_2 & p_{LU} \\ \mathbf{0} & 1 \end{bmatrix} \begin{bmatrix} \boldsymbol{I}_3 & -UJ_T \\ \mathbf{0} & 1 \end{bmatrix} \end{aligned} \tag{3.8}$$

where θ_1 and θ_2 are the angles of rotation at the LJC and the UJC, LJ_P is the location of the LJC in the P frame, UJ_T is the location of UJC in the T frame and $p_{LU} = \begin{bmatrix} 0 & 0 & l_{LU} \end{bmatrix}^T$ is the fixed translation from the LJC to the UJC.

By grouping the joint center and length parameters for each model into a parameter vector $\boldsymbol{\psi}_s$ (single-joint) or $\boldsymbol{\psi}_d$ (double-joint) the optimization problem for each model can be written:

$$\min_{\boldsymbol{\psi_s}, \boldsymbol{\theta}} \sum_{i=1}^{n} \| \boldsymbol{g}_{PT}(\boldsymbol{\psi_s}, \boldsymbol{\theta}(i)) \boldsymbol{r}_T - \boldsymbol{r}_p(i) \| \tag{3.9}$$

$$\min_{\boldsymbol{\psi_d}, \boldsymbol{\theta_1}, \boldsymbol{\theta_2}} \sum_{i=1}^{n} \| \boldsymbol{g}_{PT}(\boldsymbol{\psi_d}, \boldsymbol{\theta}_1(i), \boldsymbol{\theta}_2(i)) \boldsymbol{r}_T - \boldsymbol{r}_p(i) \| \tag{3.10}$$

where $\boldsymbol{r}_p$ are the observed thoracic markers transformed to the pelvic frame using Eq. 3.6.

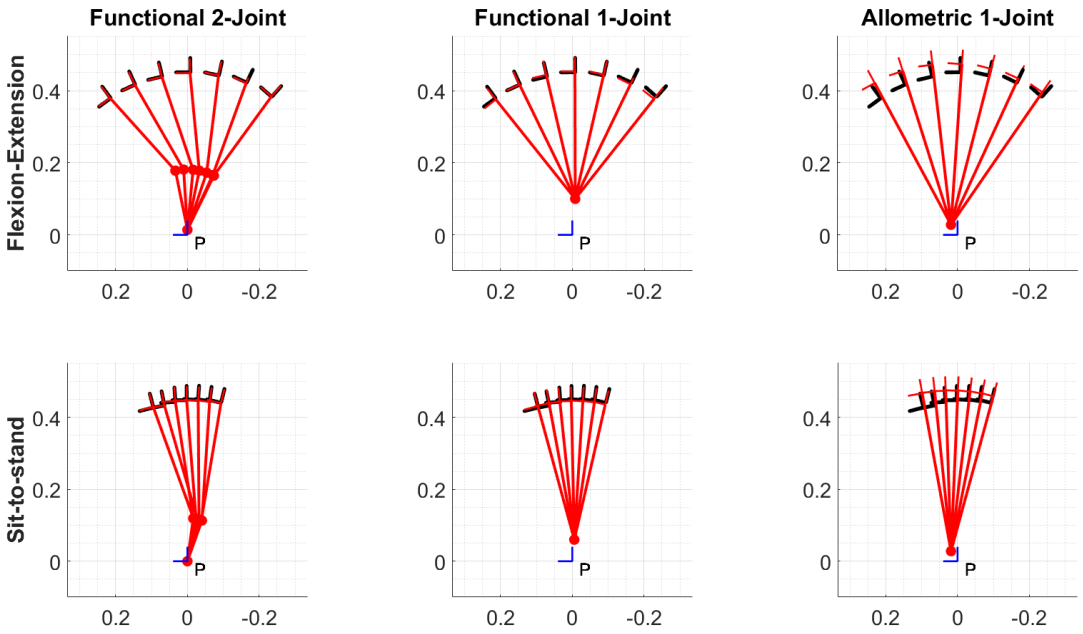

Figure 3.4: Representative example of rigid-body models recovered from flexion-extension (*top*) and sit-to-stand (*bottom*). The models from each method are shown in the sagittal plane: functional two-joint (*left*), functional one-joint (*center*), and allometric one-joint (*right*). Models are plotted in the local pelvic coordinate frame with the subjects facing left. In each plot, full flexion is the left-most configuration and full-extension is the right-most configuration. The ground truth thoracic frame is plotted in black.

Allometric Model

For comparison, height-based allometric relationships for the model parameters of a single-joint spine were derived using the methodology from Reed [40], the original dry pelvis data from Reynolds [42], and surface to spine models from Snyder [58] and Robbins [59, 68]. These relationships were recomputed for the pelvic and thoracic coordinate frames specified in Section II-A.

3.3 Experimental Validation

Experimental Protocol

The method was evaluated on ten healthy subjects (3F/7M age: 30.9 ± 9.6 years, height: 1.76 ± .12 m, mass: 67.4 ± 11.2 kg) under approval of informed consent (UCSF IRB: 12-10253).

Table 3.1: Parameter and state constraints for one-joint (left) and two-joint (right) models.

Variable	Range
JC_Y	$[-0.05, 0.05]\,m$
JC_Z	$[0, 0.2]\,m$
l_{JT}	$[0, 0.5]\,m$
θ	$[-\pi/2, \pi/4]\,rad$

Variable	Range
LJC_Y	$[-0.05, 0.05]\,m$
LJC_Z	$[0, 0.1]\,m$
UJC_Y	$[-0.05, 0.05]\,m$
UJC_Z	$[-0.2, 0.5]\,m$
l_{LU}	$[0, 0.25]\,m$
θ_1 (LJC)	$[-\pi/2, \pi/4]\,rad$
θ_2 (UJC)	$[-\pi/6, \pi/6]\,rad$

An 8-camera PhaseSpace active motion capture system (480 Hz) was used to track the motion of the surface landmarks detailed in Section II-A. LED markers were placed directly on the skin with adhesive Velcro.

The protocol consisted of three self-paced standing FE motions and three sit-to-stand and stand-to-sit actions. During FE, subjects were instructed to bend forward and backward as far as comfortable with arms at their sides. During STS, subjects were instructed to perform the action naturally with arms at their sides.

Model Recovery and Evaluation

The methods outlined in Section II were applied to recover parameters for the one-joint and two-joint models. Models were separately recovered from FE and STS data, using twenty frames of data, sampled across the full range of each motion. No constraints were applied during step A or B of Section II. Loose constraints were applied during the optimization of model parameters and joint states in step C (Table 3.1).

The recovered functional models and the allometric one-joint model were tested on FE and STS data sets, each consisting of 300 samples with training data excluded. Given fixed model parameters, we recover the joint angles using Equation 3.9 or 3.10. An example of the generated rigid-body models for a single subject is presented in Figure 3.4. Each plot displays the recovered spinal configuration at positions sampled across the motion. Note that we observe a smaller range of spinal motion in STS compared to FE.

Results

From the joint state recovery process, we compute the thoracic marker residuals, the distance between the observed and predicted (best fit) marker locations. The mean marker residual for each model is presented in Table 3.2. The residual plots in Figure 3.5 allow for visual inspection of the marker residuals dependence on the spine configuration (from fully extended to fully flexed). The mean recovered subject-specific parameters for the one-joint and two-joint models are given in Table 3.3.

Table 3.2: Mean thoracic marker residuals (mm) for functional and allometric models. Bolded entries indicate models trained and tested on the same motion (different data set).

	Test action	
Model (training action)	**Flexion/Extension**	**Sit-to-Stand**
Functional 2-Joint (FE)	**6.0 ± 3.7**	7.9 ± 5.3
Functional 1-Joint (FE)	**9.0 ± 5.7**	12.6 ± 7.3
Functional 2-Joint (STS)	9.0 ± 6.4	**5.3 ± 3.1**
Functional 1-Joint (STS)	13.6 ± 8.7	**7.5 ± 4.8**
Allometric 1-Joint	27.2 ± 15.4	27.7 ± 14.4

Table 3.3: Mean recovered parameters for functional models. Values represent the parameter as a percentage of subject height.

Parameter	**Functional FE**	**Functional STS**	**Allometric**
$\mathbf{JC_Y}$	-1.4 ± 1.1	1.2 ± 1.5	1.1
$\mathbf{JC_Z}$	4.6 ± 1.6	2.7 ± 2.7	1.84
$\mathbf{l_{JT}}$	21.5 ± 1.7	23.8 ± 3.0	25.10
$\mathbf{LJC_Y}$	-1.2 ± 0.9	-0.7 ± 0.8	–
$\mathbf{LJC_Z}$	1.6 ± 1.2	0.9 ± 1.3	–
$\mathbf{l_{LU}}$	10.3 ± 2.6	8.1 ± 4.6	–
$\mathbf{UJC_Y}$	-1.1 ± 0.7	-0.7 ± 1.0	–
$\mathbf{UJC_Z}$	-14.2 ± 1.5	-16.6 ± 4.6	–

3.4 Discussion

While the proposed kinematic models are representative of the observed aggregate motion of the spine, we make no claims on the relationship between the recovered joint centers and the internal anatomy. Therefore, it is not appropriate to compare the recovered joint centers to internal imaging studies of static postures. Rather, we consider the marker residuals as an indication of the goodness-of-fit of each model.

The marker residuals of the functional methods were lower than those of the allometric model across both motions and all subjects (Table 3.2). The two-joint model outperformed the one-joint model both when the models were trained and tested on the same action and when the models were trained and tested on a different actions. As expected, there was a decline in performance when the functional models were trained and tested on different motions, though the decline was smaller for the two-joint model.

Visual analysis of the residual plots in Figure 3.5 provides additional insight into the fit of the models. The plots show the mean residual against the % of the phase (ie. the proportion of the motion completed). For a perfectly fit model, we expect to see a horizontal line, meaning the marker residuals do not vary predictable with the motion of the spine. For the allometric model, we observe a dependency on the phase, with greater marker residuals

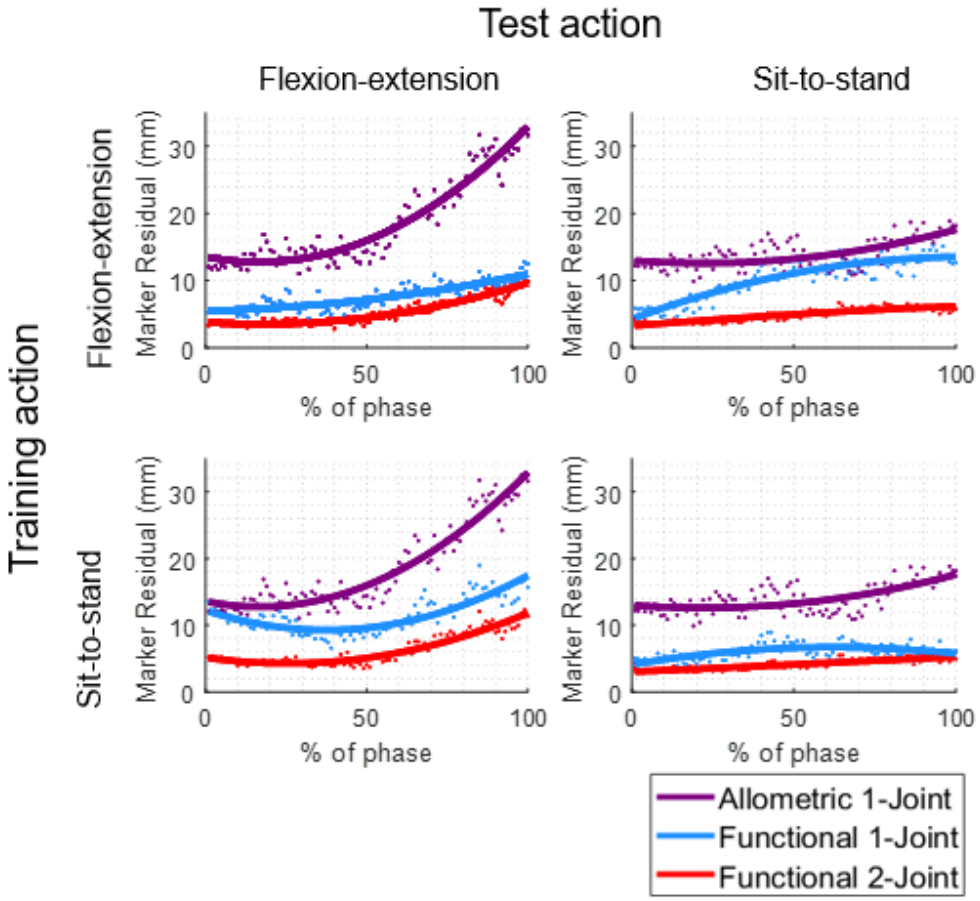

Figure 3.5: Marker residual plots for three models for FE and STS. The vertical axis is the mean distance between the observed and predicted thoracic markers, averaged across ten subjects. The horizontal axis is the percent of phase of each motion, where 0 corresponds to full-extension and 100 corresponds to full-flexion. Two-degree polynomials were fitted to the data for visualization.

with higher flexion in the FE action. While significantly less pronounced in the functional methods, we also see an increase in marker residuals during the higher flexion portion of the FE action. Soft tissue artifacts, particularly the stretching of the skin, may account for some of this increased error. We also see a greater dependency on the phase when the functional methods are tested on a different action. However, there is less variation in the two-joint model, indicating that the recovered model may be less action-specific.

Although the goal of this work is not to suggest new allometric scaling relationships, we present the mean recovered model parameters in Table 3.3. We observe variations across subjects and within subjects for models trained on FE and STS. For the one-joint model,

there is a statistically significant ($p = .009$) difference between the recovered joint location from FE and STS. The lower joint center in STS may be a result of less motion in the upper lumbar or thoracic vertebrae. It is necessary to train the simplified one-joint model on the test action of interest.

3.5 Chapter Summary

The functional joint center method presented in this chapter provides a quick method for generating a subject-specific model of the spine for use in analysis of motion. This method does not require internal imaging or rely on allometric relationships. When compared to an allometric model, the functional models result in lower marker residuals with less dependency on the phase of the motion. This method does not provide the location of intervertebral joint center locations, but rather presents joint centers for a representative kinematic model of the aggregate motion of the spine. The formulation of the optimization limits the structure of the rigid-body model to a maximum of two joints. However, the method could be applied to motions outside of the plane, such as lateral bending.

Future work may explore the application of this method to the analysis of spinal motion and loading in a clinical population. In contrast to allometric models or regression equations, this functional method is not based on data from a healthy population. Thus, it may have greater applicability to a clinical population, such as subjects with spinal deformity or spinal fusion. Known fusion geometry may be incorporated into the model parameter constraints to derive subject-specific models.

Chapter 4

A Passively Assistive Knee Orthotic

As described in Chapter 2, the sit-to-stand motion is an activity of daily living which requires significant torque generation and coordinated movement at multiple joints. It is therefore important to consider the whole-body biomechanics when designing an assistive device for STS. In this chapter, we present a passive elastic orthotic was developed which provides bilateral knee extension assistance. Initial human experiments were conducted with two subjects under two foot-placement conditions. The human and device kinematics and dynamics were modelled, allowing for the assessment of the biomechanical effects of the device. The assistance resulted in a decrease in the human knee torque as well as changes in whole-body biomechanics, notably an increase in the linear momentum of the upper body and a decrease in the anterior excursion of the center of mass. These results indicate that single-joint assistance at the knee has the potential to both facilitate successful STS and positively alter whole-body biomechanics.

4.1 Motivation and Overview

Sit-to-stand (STS) is both an activity of daily living and a common clinical test of strength and balance. Rising from a chair requires coordinated joint motion: extension of the knees, coupled with an initial flexion and then extension of the hips [69]. The biomechanics of the motion are well-studied, including the analysis of failed STS and the identification of STS strategies in elderly and pathological populations [70]. When compared to the momentum-transfer strategy adopted by most healthy, younger adults, elderly subjects have been found to lean forward more, moving their center of mass over their ankles quasi-statically before rising [71]. Conversely, individuals with low back pain rise with less hip swing and torso inclination [72]. Although the motion can be successfully completed under these strategies, they may result in greater joint loads or a higher likelihood of STS failure. Building on these strategy studies, this work aims to study how passive knee assistance will affect whole-body biomechanics. Primarily, the goal of the device is to facilitate successful STS. However, we also hypothesize that, in addition to reducing the required human knee torque, assistance

at the knee will alter full-body biomechanics, potentially encouraging a STS strategy with a desirable biomechanical outcome (e.g. decreased spinal loading or greater momentum).

While most lower-limb exoskeleton development has focused on gait assistance, a number of devices have been designed specifically for STS assistance and assistance at the knee [73]. These systems are actively actuated by DC motors, series elastic actuators (SEA), or pneumatic artificial muscles, typically operating under position, force or impedance control. After a reference position or torque trajectory has been identified, a low level controller is used to provide feedback based on observed center of pressure or estimates of torque from EMG or SEA deflection [74, 75, 76]. While these systems are able to provide a standing assist, the changes to the subject's biomechanics and joint loads are under-studied, with analysis constrained to predicted changes in knee torque and power. The effects of compensation and adaptation to the device are therefore neglected, with potentially beneficial factors being omitted from the analysis. As active systems usually exhibit delays or adaptions to the user, the coupled system may behave differently to that of the individual components, so analysis of the knee joint in isolation is insufficient.

In addition, these powered systems require complex controllers and are limited by cost, weight, and energy consumption. In contrast, passive or passive/active systems utilize adjustable energy storage mechanisms such as electrostatically clutched elastics or pneumatics to adjust the dynamic response of the human-device system, providing assistance for upper or lower limbs [77, 78, 79]. Notably, a quasi-passive knee exoskeleton has been developed to provide various levels of assistive stiffness in parallel with the knee during gait with analysis of the biomechanical effects at the ankle, knee, and hip joints [80], [81]. Tuned passive devices have also been shown to provide super-human ability in the form of decreased VO_2 consumption during gait [82]. As a measure of endurance, VO_2 is not an appropriate metric for an activity such as STS which is not aerobically limited. This we therefore present changes in the observed biomechanics, specifically the joint torque, body momentum, and center of mass trajectory which may correspond to limitations in strength, coordination, or speed.

Contributions

We introduce a passive knee orthotic designed to provide bilateral assistance in knee extension during STS. The system utilizes an elastic element to generate an assistive torque with a fraction of the mass required by an equivalent active system. The device and resulting motion are assessed on two healthy subjects performing STS under two initial foot placement conditions. Initial analysis demonstrates the feasibility of the device to induce changes in knee and whole-body biomechanics.

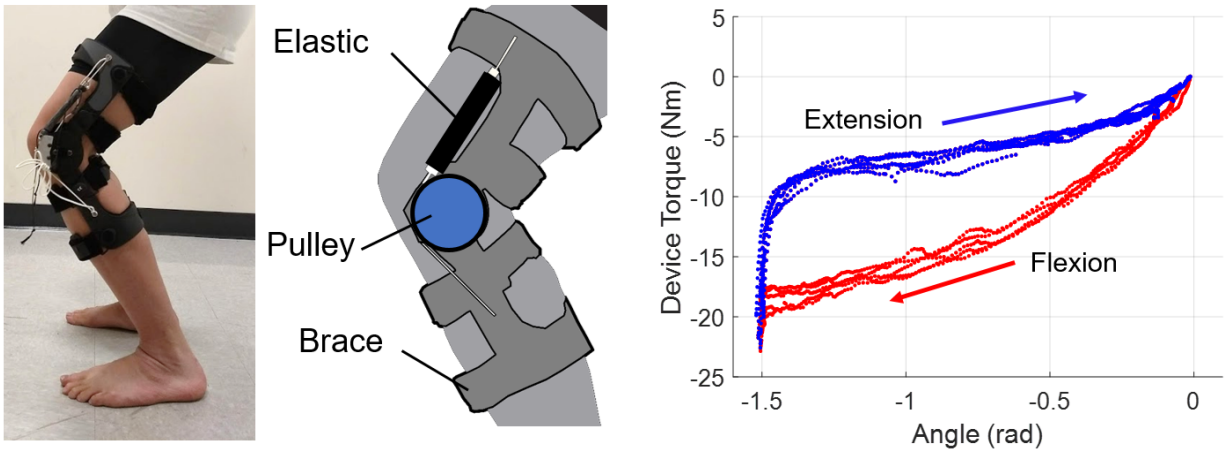

Figure 4.1: Assistive knee orthotic. Left: Device worn by a subject on their left knee (right knee hidden). Center: Schematic of knee assistive system. Elastic band, pulley, and brace as indicated. Right: Characterization curve for the knee orthotic. Flexion and extension directions are as shown.

4.2 Methods

Mechanism Design

A knee orthosis (Figure 4.1) was developed to provide passive assistance at the knee during the STS motion. The angular trajectory of the knee joint during a typical STS consists of exclusively knee extension, whereas the ankle and hip exhibit a combination of flexion and extension. This pure knee extension facilitates the application of a simple passive component without a clutch or other complex mechanism or control scheme. Assistance at the knee is generated by the linear extension of an elastic component which wraps around the knee to produce a torque. Exerting no torque at a full standing position, the device stores energy as the knee is flexed during sitting. This energy is then released during standing, providing an assistive torque in knee extension.

The device was developed by augmenting a commercially available knee brace (DonJoy Legend SE-4) which is used to provide stability following knee injury. The brace was selected for its recommended use during sports activities, allowing for a full range of motion. A 78 mm diameter, 15 mm thick Delrin puck was added onto the knee center of the brace to act as a fixed pulley. Two guides were fabricated out of aluminium and fixed to either side of the pulley.

The elastic band was constructed from a 5/8" outer diameter, 1/8" inner diameter rubber tube (Primeline Industries, Ohio) which was cut into a 1" length. Two stainless steel wishbone inserts were used to attach 2.5 mm Spectra line to each end. The band was secured onto the wishbone insert using a constrictor knot made from 1 mm braided Kevlar. The band was secured onto the brace so that there was slight pre-tension in the line when fully

extended. An R-clip was used to constrain the Spectra to lie between the pulley guides. The total mass of each orthotic was 0.81 ± 0.01 kg.

It is important to note that the device was designed to enable the study of biomechanical effect of assistance during STS, rather than to be worn in daily assistance in its current form. As the mechanism of assistance is designed with consideration for STS, the device would likely inhibit knee motion during gait or other activities.

Device Characterization

Bench-top characterization of the device torque-angle relationship was performed immediately prior to and after each human experiment. With one side of the brace clamped, the contact force at the opposing side was measured using a 6-axis force/torque sensor (ATI Mini-45, ATI Industrial Automation), recording the force measurements at 1000 Hz as the device was manually moved through its full range of motion five times at a gentle pace. Motion capture data of the brace was simultaneously collected to measure the knee flexion angle. The resulting torque-angle curve is shown in Figure 4.1. While hysteresis was observed between flexion and extension, the device was found to provide a repeatable torque response. The maximum assistance provided by the device was measured to be 12 Nm at a knee flexion of 1.5 rad with an approximately linear relationship. The amount of assistance can be adjusted by changing the length or material properties of the band. During testing, a brace is worn on both the left and right legs, providing total assistance equal to twice the characterized value.

Human-Device Model

To assess the motion and analyze the contribution of the knee assistance, it is necessary to model the kinematics and dynamics of the STS motion. A sagittal-plane rigid-body model is used to perform planar inverse kinematic and inverse dynamic analysis. The model consists of revolute joints at the ankle, knee, hip, and lower-lumbar (L5-S1). Length and body segment center of mass parameters were allometrically-scaled by the subject's height and mass [2]. The recovered joint angles can be converted to velocities and accelerations which are propagated through each segment. The wrench in the local body-frame can then be computed to provide estimates of joint torques and powers [83]. The estimated resultant knee torque τ_r obtained through this method is then decomposed into the device τ_d and human τ_h components based on the prior device characterization:

$$\tau_h = \tau_r - \tau_d \tag{4.1}$$

4.3 Experiment

Motion capture and force data were collected to study the effect of bilateral knee assistance on full-body biomechanics during STS. This preliminary data was collected from two healthy

young-adult subjects (S01: male, age 30, 1.78 m height, 65 kg weight, and S02: female, age 26, 1.55 m height, 56 kg weight) under informed consent (UCB IRB protocol 2018-04-10940).

Kinematic data was collected from an 8-camera motion capture system (PhaseSpace Impulse X2, PhaseSpace Inc., San Leandro, CA, USA) at 480 Hz. Markers were placed directly on the skin using adhesive Velcro according to an augmented Plug-In Gait protocol [43], allowing for recovery of the sagittal plane human model. Additional markers were placed on triads mounted on the knee brace. Ground reaction forces were collected with a 6-axis force platform (AMTI, Massachusetts). Additional forces were collected from a 6-axis force/torque sensor (ATI Industrial Automation) mounted inside of a custom chair.

The STS motion was performed under two initial kinematic configurations: natural foot placement and anterior foot placement. The natural position was self-selected by each subject as a comfortable standing position. The anterior foot position was selected at a knee flexion angle of approximately 1.2 rad. This position was chosen to make the STS motion more biomechanically challenging.

STS motions at each foot position were tested under two device conditions, unassisted and assisted, resulting in four total testing conditions. In the unassisted mode, the subject wore the brace with the band disengaged.

For each of the four testing modes, the subject completed three trials consisting of seven STS motions. The subject began each trial in a seated position and was instructed to fold their arms across their chest. The subject was otherwise not coached on how to stand. A metronome at 30 beats per minute was used to indicate when to stand and sit. This allowed for a period of quiet sitting and quiet standing between each sitting or standing action.

Joint positions were estimated from motion capture data using an allometrically-scaled model [2]. The resulting joint angles were then repeatedly filtered and numerically differentiated (Butterworth, 2nd order, 6 Hz) to obtain the corresponding angular velocity and acceleration trajectories.

4.4 Biomechanical Effects of Assistance

This section introduces key biomechanical features for the assisted and unassisted standing actions. Analysis is performed at the knee specifically (Section 4.4) as well the whole-body motion (Section 4.4).

Knee Torque

The torque response curves for the knee are shown in Figure 4.2 with knee extension corresponding to a negative torque. The knee torque is evaluated from the moment of seat off (defined as the point at which the vertical force in the chair is less than 20 N) to quiet standing (defined by zero torso velocity). For the assisted mode, the resultant torque (red) is decomposed into the predicted device torque (black) and human torque (green). It is shown alongside the human torque from the unassisted motion (blue).

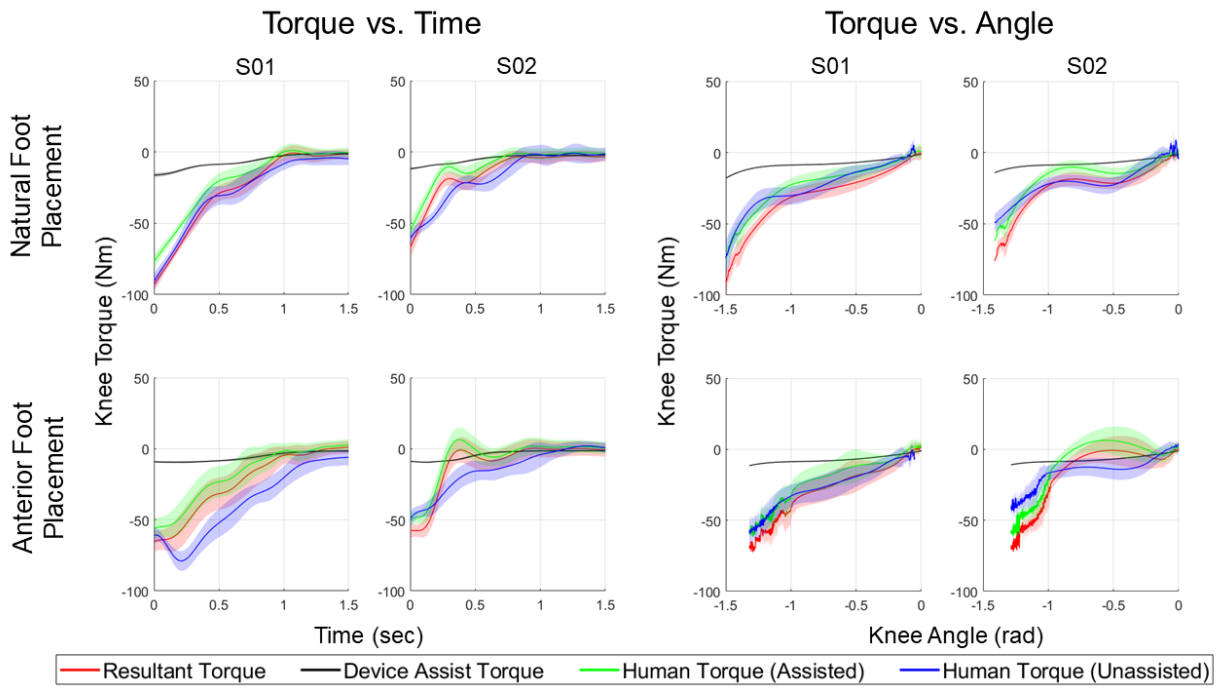

Figure 4.2: Knee torque during sit-to-stand as a function of time (left) and knee angle (right). Each plot has three lines for the assistive mode: the resultant torque from the human and device (red), the device torque (black), and the remaining human torque (green). Additionally, the human torque in the unassistive mode is plotted in blue. The trace represents the mean trajectory across all trials with the standard deviation shown as a shaded region of the same colour. The plots are shown for each subject and separated by the natural foot (top row) and anterior foot placement (bottom row) conditions.

Under assistance, there is an expected decrease in the human torque required. In the torque-angle curves, we observe that the human torque during the assisted mode initially aligns with the unassisted human torque. At a knee angle of approximately -1 radians, the assisted human torque decreases so that the resultant torque matches the unassisted human torque. This suggests that the subjects may exploit the assistance partway through the action. This pattern is consistent across trials, suggesting that subjects are not adapting to the assistance over trials. An exception is seen in the anterior foot placement condition for S02, in which the human provides an abating knee torque in the second half of the motion. This observed torque in the knee flexion direction appears to compensate for greater trunk momentum. The whole-body biomechanical analysis (4.4) indicates that the subject changed their standing strategy under these conditions.

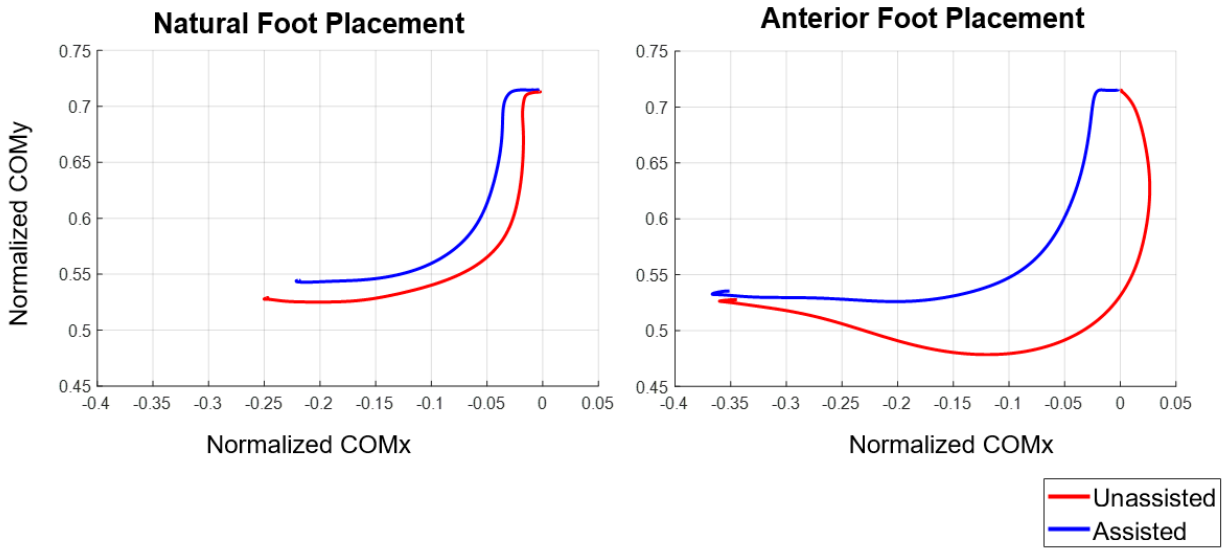

Figure 4.3: Trajectory of the center of mass (COM) of the head-arms-trunk segment during STS with natural foot placement (top) and anterior foot placement (bottom). Trajectories are normalized by subject height with the average taken across all trials for each subject. Blue lines denote assisted trajectory and Red lines denote unassisted trajectory.

Whole-body Biomechanics

Center of Mass

For both foot configurations, the assistance at the knee resulted in a steeper vertical rise of the head-arms-trunk (HAT) body segment. This can be observed in the trajectory of the HAT center of mass (COM) shown in Figure 4.3. This smaller anterior excursion of the COM corresponds to less trunk inclination during the motion.

Torso Momenta

The torso momenta $\boldsymbol{p}$ are computed from the body velocities of the torso and the torso inertia tensor $\mathcal{I}_{torso}$:

$$\boldsymbol{p} = \boldsymbol{I}_{torso}\boldsymbol{V}^{b}_{torso} \tag{4.2}$$

Figure 4.4 shows the vertical component of the linear momentum of the HAT segment. Under all conditions, the peak vertical linear momentum increases with the assistance at the knee. With normal foot placement, the momentum consists of a single peak, suggesting a single momentum transfer action, moving the COM forward and up vertically. This is seen in the assisted and unassisted modes for both subjects. For the anterior foot placement condition, the unassisted mode appears to consist of two separate sections. This may indicate a leaning strategy where the first peak corresponds to the initial movement of the torso,

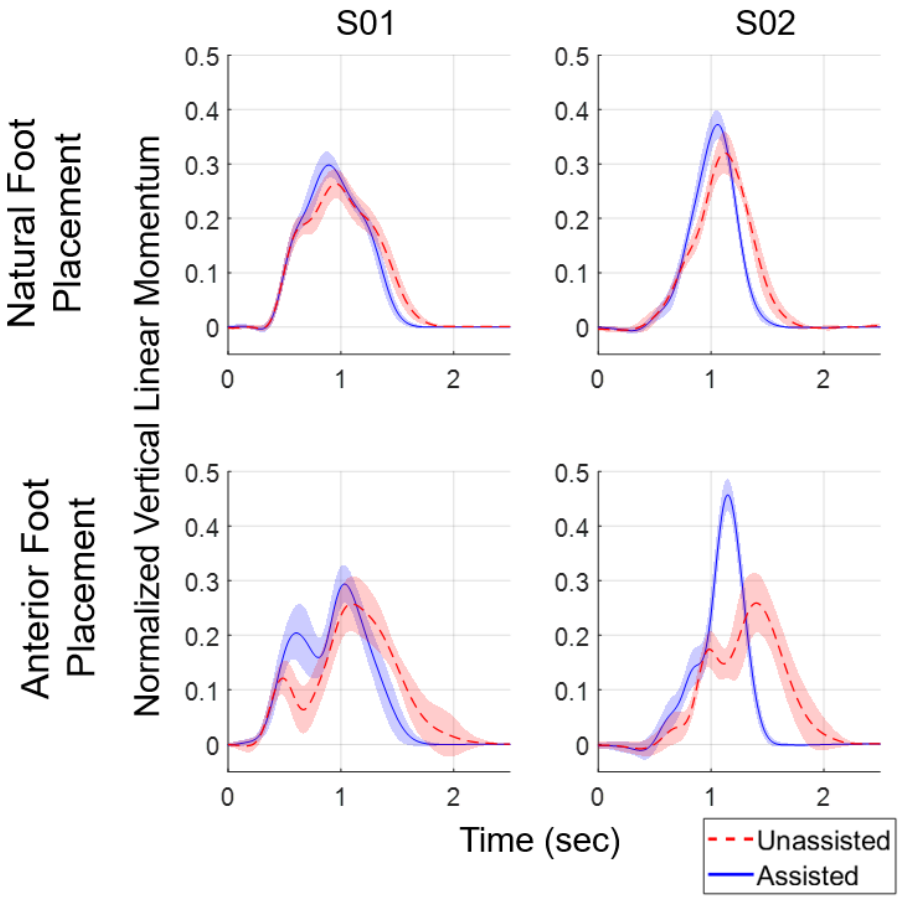

Figure 4.4: Vertical linear momentum of the head-arms-trunk segment. Unassisted motion is shown in red dashed line with assisted motion in blue solid line. The values are normalized by subject height and mass and shown for S01 (left) and S02 (right) under the natural foot placement (top row) and anterior foot placement (bottom row). In each plot, the mean over 21 motions is shown with the standard deviation in shaded bounds.

before there is a second separate rise. For S02 in the anterior foot condition, a transition is seen from a lean strategy to a momentum transfer strategy in the assisted mode. This change in strategy is not seen in S01.

The passive orthotic was able to provide assistance which resulted in lower knee loading and changes in whole-body kinematics and dynamics. This initial biomechanical analysis supports the hypothesis that passive extension assistance at the knee has the potential to affect full-body biomechanics during STS. The increase in upper body vertical momentum was observed for both subjects under all assisted testing conditions. This change in momentum, alongside the corresponding decrease in the anterior excursion of the COM, are promising for improved motions as low vertical momentum was found to be an indicator of failed STS [70].

4.5 Chapter Summary

In this chapter, we present a new device for assistance in knee extension during STS. Augmenting an existing knee orthotic, the device incorporates a simple elastic elemant to provide passive assistance. Our results support the hypothesis that assistance at a single joint can affect whole-body motion. Additionally, our bio-mechanical analysis highlight the varied effect even simple systems can have on whole-body biomechanics and that, even for simple systems, people may respond differently. While providing knee extension assistance during sit-to-stand decreased the average human knee torque for both standing conditions, the effect on the low-back and hips varied. By studying the full-body biomechanical effects of assistive systems, simple devices can be developed to encourage specific motions.

Limitations

Only two healthy subjects were tested in this study over a short time horizon, making generalization on the effect of this system to other subjects, particularly patient groups unclear. Similarly, analysis only occurred in the sagittal plane with the effect of the motion of the arms neglected. The validity of these assumptions needs to be tested as part of a wider study.

Future Work

While this chapter introduces a method for altering whole-body motion, the relationship between the assistance and the resulting motions is not known. A more detailed study that builds on a parameterized model of STS, and a variable stiffness actuator would allow for rapid assessment of the effect of different extension profiles on whole-body standing and balance. A better understanding of the underlying mechanisms for whole-body biomechanics changes would be an electromyography(EMG) study, focusing on the differences in muscle activation in the knee flexors, lower back, and abdominal core muscles. Finally, in order

to translate this method to provide daily assistance, future work must include mechanism development to allow for free or assisted motion during gait.

Chapter 5

An Affordable Device for Robotic Therapy

Since its inception in the 1980s, the field of rehabilitation robotics has seen significant advances in the development of complex mechanisms and controllers. These robotic devices have the potential to facilitate precise, high-intensity, and adaptable rehabilitative tasks while tracking quantitative measures of subject ability. Studies of robot-assisted therapy, however, have only demonstrated modest benefits over traditional therapy, and we have yet to see a widespread adoption of robotic therapy as the standard of care for in-clinic or at-home therapy. While several factors inhibit the adoption of rehabilitation robotics, an undeniable barrier results from high device cost and complexity. This inaccessibility further contributes to a limited understanding of models of recovery and optimal robotic rehabilitation protocols.

We aim to address the limitation of cost and complexity through the introduction of an affordable planar manipulanda for upper limb assessment and therapy. With a total part cost of less than $800, the device utilizes inexpensive and off-the-shelf components to provide active assistance and resistance. It is capable of guiding the arm through trajectories, following the subject's intended motion through force-based admittance control, and imposing assistive or resistive force-fields while tracking the position and force exerted by the subject. In this chapter, we present our design objectives and outline the mechanical, electrical, and software systems. We validate the device performance and present a new method for determining the human arm 3D upper-limb inverse kinematics with the device. Finally, we show initial data from human subjects interacting with the developed system.

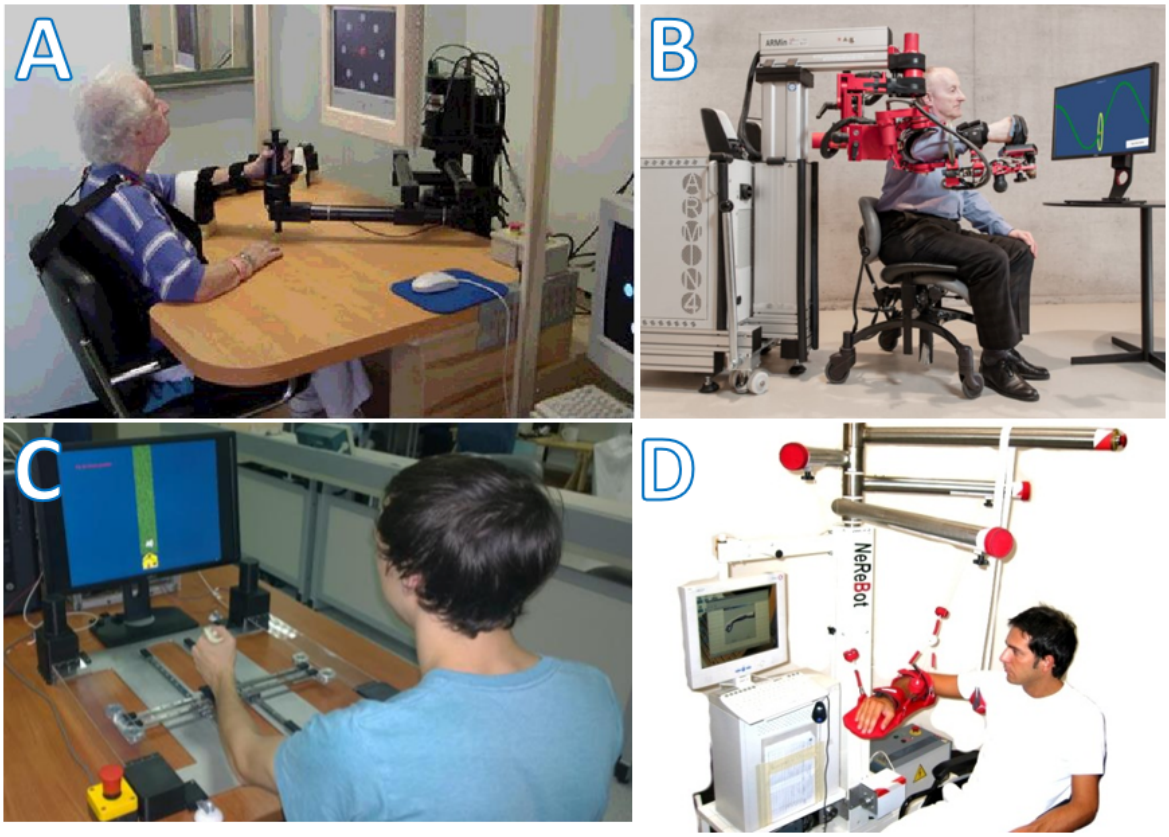

Figure 5.1: Examples of upper-limb robotic rehabilitation devices. A: In-Motion Arm, the commercial version of the MIT-MANUS [84], B: ARMin 4 [85], C: H-Man [86], D: NeRoBot [87].

5.1 Overview of Upper Limb Rehabilitation Robotics

During robot-assisted therapy, a robotic device provides continuous physical interaction with a subject to complete a rehabilitation protocol. This therapy can be incorporated into rehabilitation for subjects with upper limb impairment due to neurological injury such as stroke or spinal cord injury [88]. Stroke is a leading cause of disability in the United States, with many patients experiencing impairment of the upper limb [89]. This motor impairment can manifest in several ways including weakness, spasticity, loss of coordination, and abnormal muscle synergies. The presence of impairments of the upper-limb and hand inhibit the ability to perform activities of daily living and live independently [90]. The incorporation of robotic technology into rehabilitation therapy is desirable because of the ability to provide high-intensity protocols targeted protocols while recording quantitative measures of performance.

There exists an array of robotic therapy devices targeted at the lower limbs, upper limbs,

and hands. We focus on devices for the upper-limb with a few examples of devices shown in Figure 5.1. When describing a robotic therapy device, we can make distinctions based on the mechanism and control architecture. These design choices impact how the subject interacts with the device. Upper-limb rehabilitation robots can be classified as an exoskeleton or end-effector device based on the mechanical structure. Exoskeleton devices have a structure which allows for the control of individual human joints, with the device structure mimicking the anatomical structure of the human. An example is the ARMin device shown in Figure 5.1 B [85]. In contrast, end-effector devices only connect to the subject at the human hand, with the human elbow and shoulder joints moving to achieve the end-effector pose. This simplification does not allow for individual joint motion, but facilitates the implementation of less-complex control schemes and less individual mechanical tuning of the device. Examples include the MIT-MANUS, H-Man, and NeRoRobot shown in Figure 5.1 [84, 86, 87].

Robotic devices can be used to implement a variety of control modalities for robotic therapy. In describing a controller as *assistive*, we make a distinction based on how the subjects interacts with the robotic device. In comparison to are purely *passive* controller, in which the robot completes the motion without input from the subject, and a purely active controller, in which the robot only measures the motion with no impact on the subject's motion, an assistive controller requires the motion to be generated by the subject with varying forms robotic assistance to complete the task or improve performance [90]. Examples of assistive controllers include force-based impedance controller [84, 85], virtual walls moving tangent or normal to a trajectory [84, 91], or trigger-based assistance in which a threshold of subject movement initiates the motion [92].

While there have been numerous studies on the design and control of robotic devices, an understanding of the clinical effectiveness of different robotic controllers is limited [93]. This is due in part to a limited number of studies and study size. In addition to the high cost of robotic devices, most are used only in specialized therapeutic institutes and require operational supervision by expert personnel [94, 95]. To further understand the efficacy of robotic therapy and develop predictive models for optimal rehabilitation protocols, there remains a need for simple, inexpensive, robotic devices.

5.2 Device Design

In this section we describe our robotic therapy device shown in Figure 5.2.

Design Objectives

With the aim of developing an affordable manipulanda for robot-assisted therapy and assessment, we first establish a set of design objectives:

1. Produce active motion to move the arm along arbitrary trajectories in the transverse (horizontal) plane

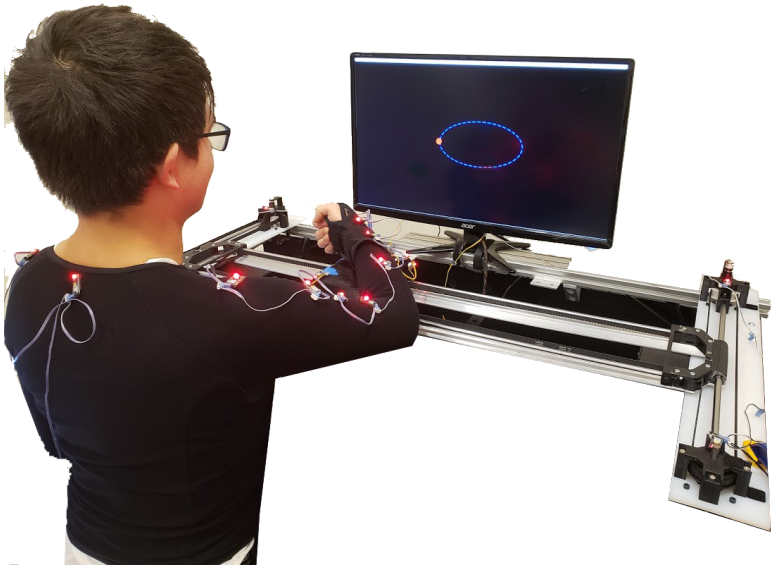

Figure 5.2: Subject seated in front of upper-limb planar rehabilitation device

2. Operate under force-based admittance control to facilitate user-initiated motion
    a) Apply resistive forces to make motions more challenging
    b) Apply force fields to guide movement or assist with error correction
3. Measure end-effector position, velocity, and interaction forces
4. Consist of low-cost off-the-shelf or 3D-printed components
5. Ensure subject safety
6. Have a portable structure
7. Meet the following specifications:
    a) Large workspace to allow for full range of shoulder and elbow motion
    b) Speed range of 0-500 mm/s
    c) Measure and withstand forces up to 50 N

A secondary goal of the device is to be compatible with interfacing with exterior input signals, including an eye-gaze tracking system and a brain machine interface. These studies are part of research collaborations with the Department of Mechanical Engineering at the Hong Kong University of Science and Technology and the Department of Neuroscience at the University of California, San Francisco. The application of those controllers to this device is not further described in this thesis.

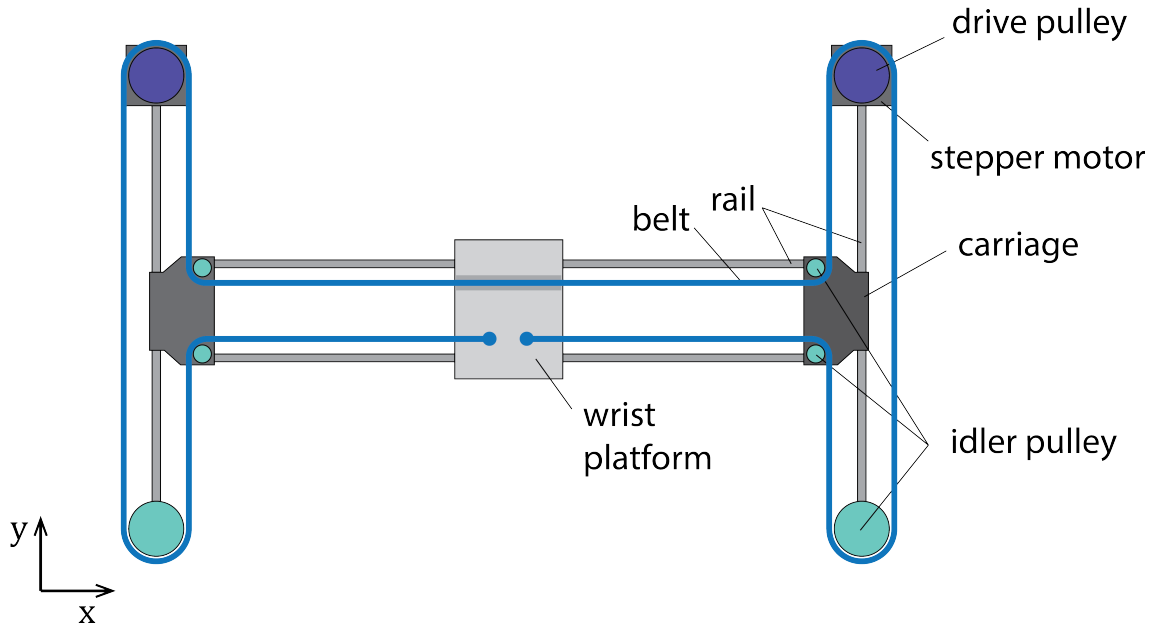

Figure 5.3: Diagram of the mechanical structure of the robot

Mechanical Design

The mechanical structure of our device is shown in Figure 5.3. The system consists of a belt-driven transmission which enables 2D motion in the horizontal plane. This H-shaped differential drive is heavily inspired by the design of H-man [86], a planar manipulanda for haptic interaction. The differential transmission allows for a single belt to move a central platform, while minimizing the inertia of additional transmission elements such as motors by keeping them fixed. In contrast to linkage-based systems, this mechanical architecture results in simplified kinematics and high isotrophy. While we utilize the general mechanism structure of H-man, our mechanical design and control implementation differs to achieve the aforementioned design criteria. Notably, we alter the mechanism to have a large workspace, with a new design for the center carriage and human-robot connection at the wrist. The use inexpensive actuation and force sensing systems require changes throughout the system architecture which are detailed below.

The transmission controls the motion of the end-effector, a platform onto which the subject's forearm is mounted at the wrist. This wrist platform can translate in the x-direction along two rails via linear bearings mounted in the platform. These rails connect on either side to a carriage assembly. Each carriage assembly is mounted on a rail via another pair linear bearings, allowing for translation of the wrist platform and carriages in the y-direction. The motion of the wrist platform is guided by the transmission belt which is is mounted to

one side of the platform and has free motion through the other side of the platform. Two motors connect to the drive pulleys, which move the belt through a pair of idler pulleys in the opposite corners of the device. Four additional idler pulleys are used to guide the belt through the side carriages to and from the center platform. This differential configuration allows for controllable movement through the horizontal plane. The rails, drive pulleys, linear bearings, and small hardware are all off the shelf components. The wrist platform, carriage assemblies, idler pulley, and motor mounts are custom, 3D printed parts.

Actuator Selection

Actuators can be one of the most expensive components of a robotic system. We sought a low-cost actuator which would operate within our desired specifications. The initial system was designed with brushed DC gear motors. However, the performance did not meet the torque specification at low speeds. Our final system is driven by two high-torque stepper motors (Nema 23, 4A, 3Nm), which are typically used for CNC machinery applications. Stepper motors allow for high-torque, open-loop control control, even at low speeds. The motors are powered at 24V and controlled by a digital stepper motor driver (DM542T) with anti-resonance. To achieve a smooth motion, the stepper motors operate at 1/32 microstepping. Motor control is performed at two levels: motor angular velocities are first computed by the high-level microcontroller (Teensy 3.6) and then sent to a motor microcontroller (Teensy 3.2) via I2C. The motor microcontroller converts these desired velocities into pulses which are control the stepper motor driver. In this configuration, the end-effector has a maximum speed of 500 mm/s. This maximum velocity can be altered by adjusting the microstepping configuration.

Device Kinematics

The device kinematics match those of the H-man system and are described by the equation:

$$\begin{bmatrix} \dot{x} \\ \dot{y} \end{bmatrix} = \boldsymbol{J} \begin{bmatrix} \omega_L \\ \omega_R \end{bmatrix} \tag{5.1}$$

where $\dot{x}$ and $\dot{y}$ are the end effector velocity in the task space, ω_L and ω_L are the angular velocities of the left and right motors, and $\boldsymbol{J}$ is the manipulator Jacobian which can be written:

$$\boldsymbol{J} = \frac{r_p}{2} \begin{bmatrix} -1 & -1 \\ -1 & 1 \end{bmatrix} \tag{5.2}$$

where r_p is the radius of the drive pulley. Note that due to the fixed position of the actuators, the manipulator Jacobian is not dependent on the device configuration.

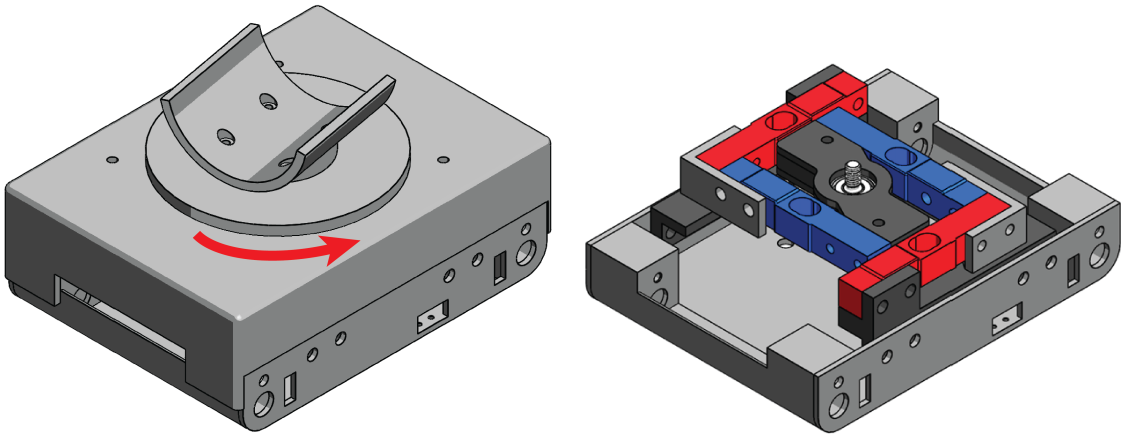

Figure 5.4: CAD model of the wrist platform (left) and interior force system (right)

Wrist Platform

The human subject connects to the device at the wrist platform. We designed the device to connect at the forearm rather than at a handle gripped by the hand. This allows the hand to remain free to interact with objects in the environment while engaging in gross upper-limb motion through the device. This is useful in the study of the reach-to-grasp motion. When using the device, the subject wears a semi-rigid wrist guard to restrict the flexion-extension of the wrist, simplifying the upper-limb kinematics. The wrist is then docked into a 3D-printed semi-circular mount and secured with hook-and-loop straps. The arm may be mounted at different angles of of forearm pronation, with the palm facing down or to the side. The wrist-mount is connected to a freely rotating semi-circle which connects to a ball bearing under the cover. This allows for passive rotation of the forearm relative to the wrist platform during motion. This configuration can be replaced with a handle to allow for interaction to occur at the hand rather than the forearm.

Force Measurement

It is important to measure the interaction forces between the human and the device for several reasons. Interaction forces can be used to assess the subject's strength and coordination, implement an admittance controller for volitional movement, and ensure safety of the human subject. To measure the interaction forces, we designed a novel configuration consisting of four 5 kg load cells mounted underneath the cover of the wrist platform. These inexpensive uni-axial load cells are commonly used in weighing scales. Two sensors measure the force in each the x-direction and y-direction. Forces from the wrist platform are transferred through a shaft and ball-bearing. The bearing is mounted in a 3D-printed bracket which contacts the pair of load cells which measure forces in the y-direction. These load cells are mounted to a second pair of load cells through 3D printed brackets allowing for the measurement of

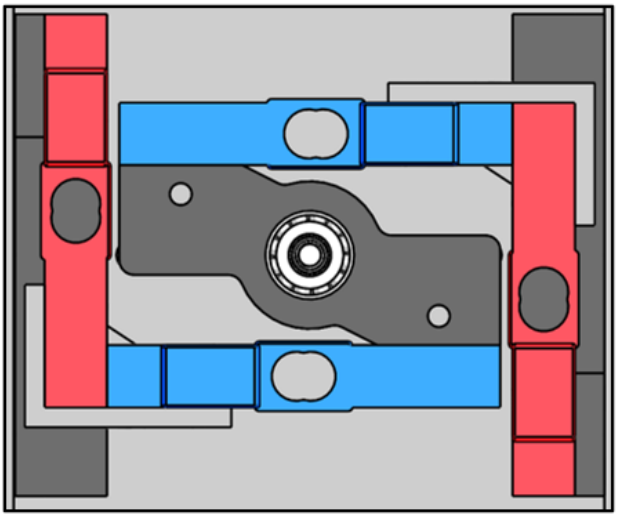

Figure 5.5: Top-down view of the force system

force in the x-direction. The force at the contact point can then be resolved as the sum of all forces:

$$F_x = F_{1x} + F_{2x} \tag{5.3}$$

$$F_y = F_{1y} + F_{2y} \tag{5.4}$$

The force subsystem electronics are mounted within the wrist platform. The load cell voltage is measured by an analog-to-digital converter with a programmable gain amplifier (ADS115). These measurements are then sent to the force microcontroller (Teensy 3.2) via I2C. The force subsystem is shown in Figure 5.8. The load cell configuration is capable of measuring a maximum 10 kg, or 98.06 N, in any direction, with a resolution of .074 N. The ADC chips were selected to maximize the loop speed with a tradeoff in decreased resolution. The maximum load capacity exceeds the 50 N design objective. While a limitation of the system is the inability to measure out of plane forces and torques, these are not necessary given the mechanical design of the system. The device mechanically supports the wrist along the z-axis. The wrist attachment is designed to minimize torques about the x- and y- axes. Finally, given the two-link upper limb system enforced by bracing the wrist, it is not possible for the subject to generate a torque about the z-axis.

Electronics Design

The electronic system architecture (shown in Figure 5.6) consists of a main microcontroller which connects to a motor subsystem (Figure 5.7), a force subsystem (Figure 5.8), and a PC user interface. The main microcontroller is a Teensy 3.6 which features a 32 bit ARM Cortex-M4 processor. This microcontroller operates at a 330 Hz loop frequency. The force

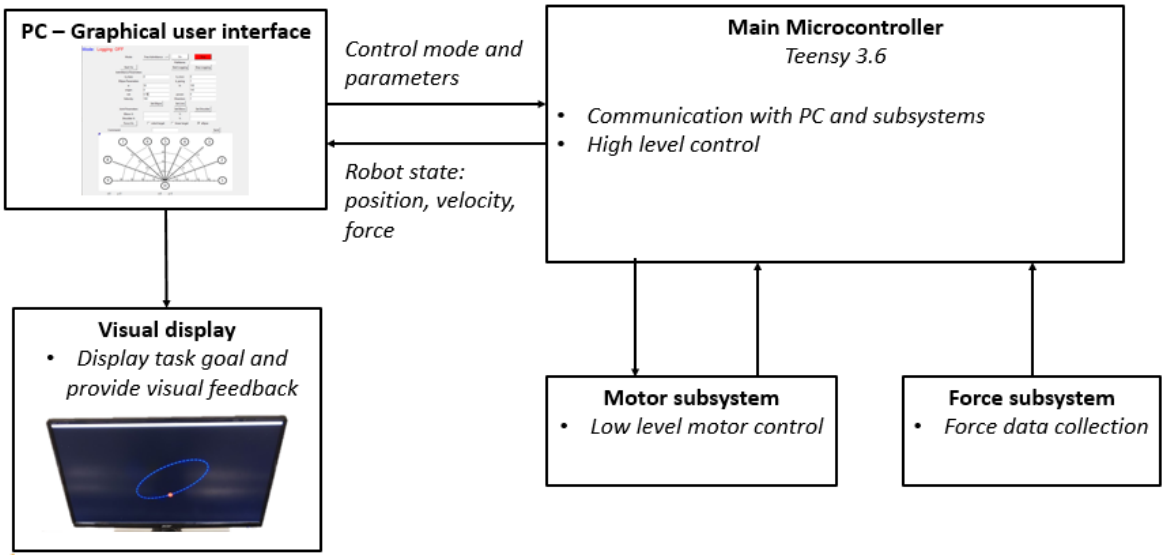

Figure 5.6: Electronic system architecture

and motor subsystems both use a Teensy 3.2 microcontroller, with connections via I2C. Separate microcontrollers were used for these subsystems to maximize the main control loop frequency. The graphical user interface is run in Python and used to set the controller and experimental parameters and log robot state data. It includes a real time visualization of the robot state, including end-effector position and force, as well as an interface to save the data files. The user interface includes a subject-facing display on a separate monitor which can display the desired task and the real time position of the end-effector. The position of the wrist platform is measured by absolute magnetic encoders (US Digital MA3) mounted to each of the drive motor shafts.

Safety Considerations

When designing any system that interacts with a human, it is essential to implement a number of safeguards to mitigate the risk of injury or discomfort to the subject. Workspace limitations prevent the device from moving outside of a subjects comfortable reachable workspace. These are implemented in software as virtual walls which can be customized to each subject alongside limitations on maximum velocity and force. The device power runs in series with two emergency stop buttons which are held by the subject and researcher during experiments. Hitting the button will cut power to the motors. Additionally, there is a software emergency stop in the graphical user interface which will set all motor velocities to zero. Mechanical hardware limits are enforced through physical limit switches which are triggered at the edges of the device workspace. These limit switches are also utilized during the position calibration procedure.

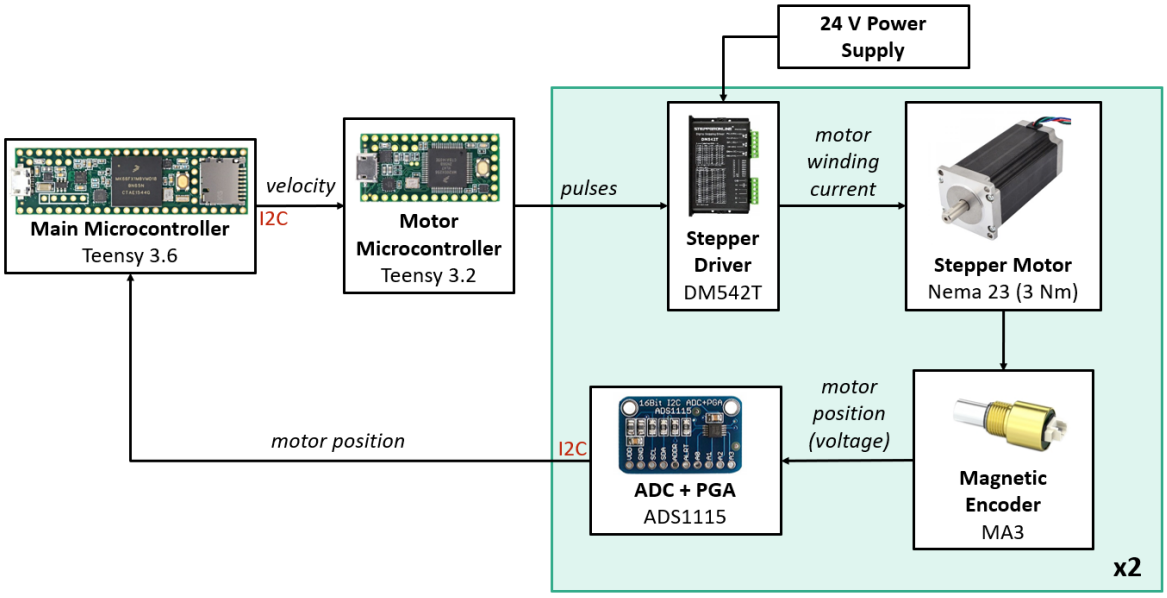

Figure 5.7: Diagram of the motor electronics subsystem

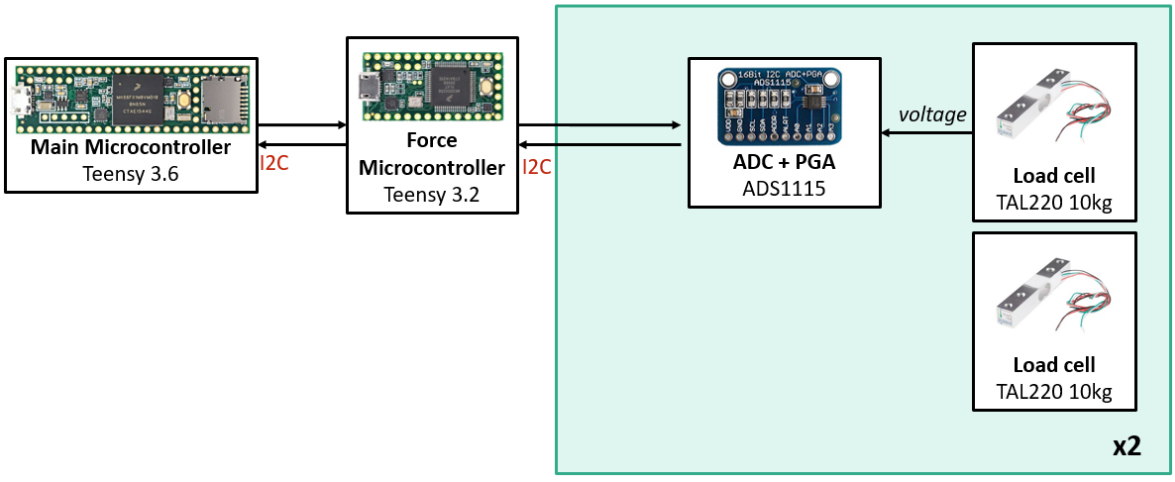

Figure 5.8: Diagram of the force measurement electronics subsystem

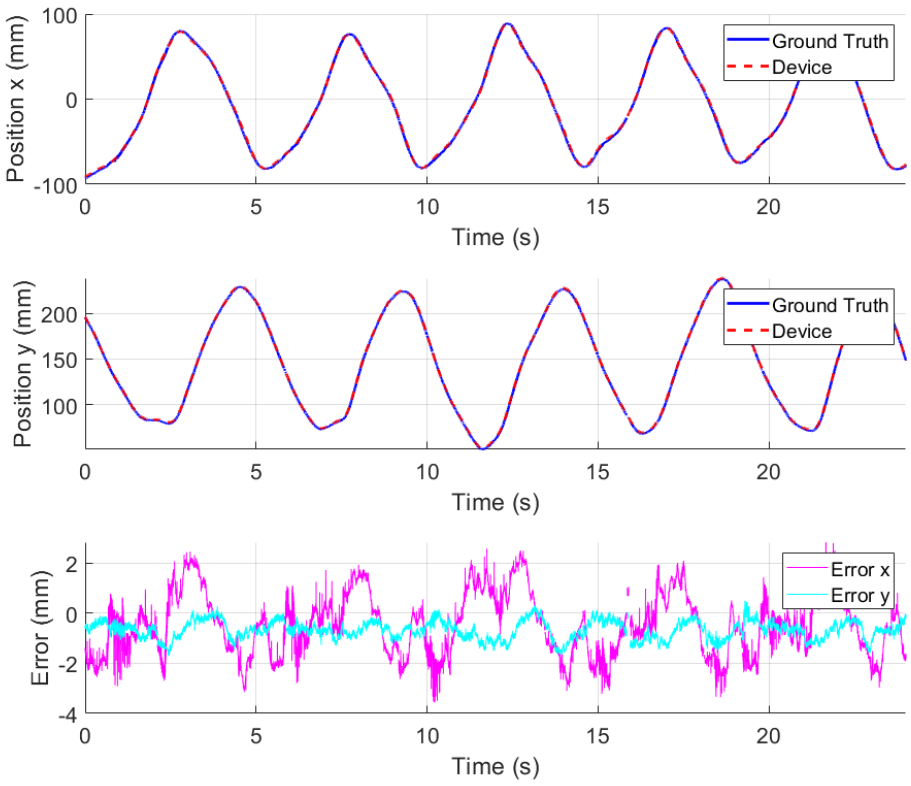

Figure 5.9: Sample data comparing the position trajectories as measured by the ground truth motion capture system and robotic device in the x-direction (top) and y-direction (middle). The error in both directions is shown on the bottom plot.

5.3 Hardware Validation

We validated the device measurements of end-effector position and force against two gold standard measures. A marker-based motion capture system (Phasespace Impulse X2) was used to measure the position of the wrist platform. Phasespace data was recorded at 480 Hz from four markers rigidly attached to the wrist platform. Additional markers were attached to the frame of the device to align the device and camera coordinate systems. The Phasespace data was transformed into the device frame and interpolated and aligned spatially and temporally to compare to the simultaneously recorded device measurements. No additional filtering was applied. Data were collected from ellipsoidal motions completed with a human subject controlling the motion of the device. The mean absolute error for the measurement end-effector position was 1.42 ± 0.71 mm. An example of the position trajectories from the device and Phasespace is shown in Figure 5.9.

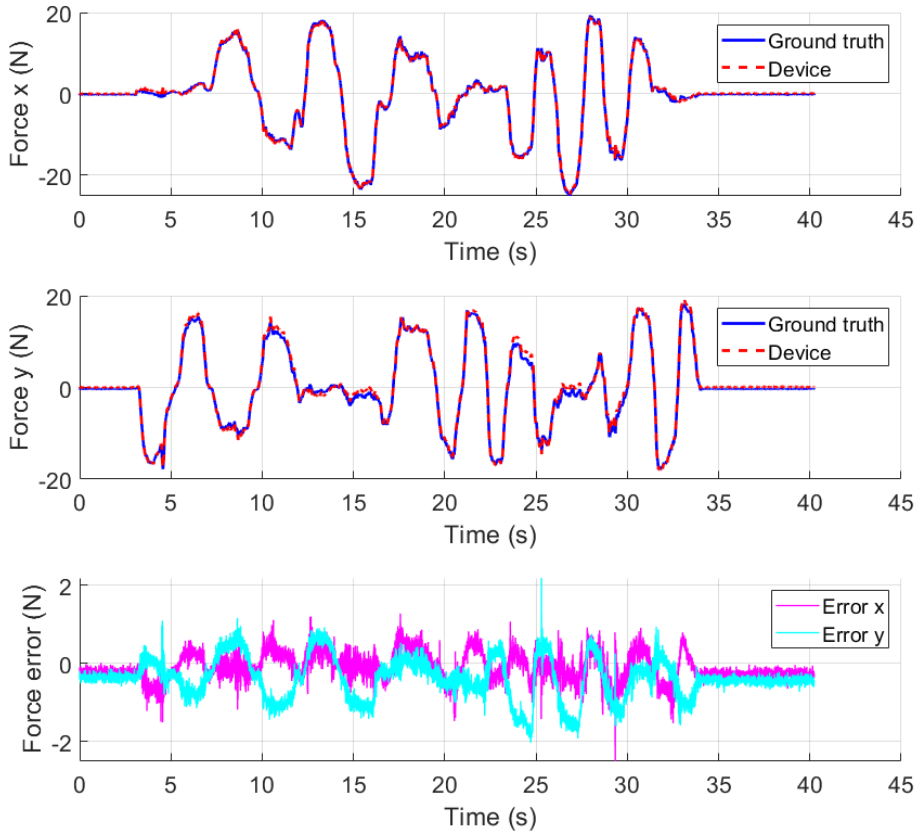

Figure 5.10: Sample data comparing the force trajectories as measured by the ground truth force/torque sensor and robotic device in the x-direction (top) and y-direction (middle). The error in both directions is shown on the bottom plot.

The device measurement of the force was compared against a 6-axis force/torque sensor (ATI Automation). Note that the device load cell configuration does not measure forces outside of the horizontal plane. The out of plane forces and torques, therefore, are not considered. To compare the forces, a custom mount was designed to attach the ATI force/torque sensor directly above the device load cell in place of the wrist mount. A handle was attached to the opposing side of the force/torque sensor. Forces were manually applied to the handle by the investigator. Forces were applied in each of the 8 cardinal directions. An example of the force measurements is shown in Figure 5.10. The mean absolute error for the force in the x-direction was 0.3 ± 0.2 N and for the y-direction was 0.53 ± 0.31 N. These results indicate that the position and force measurements are consistent with those measured by ground truth systems.

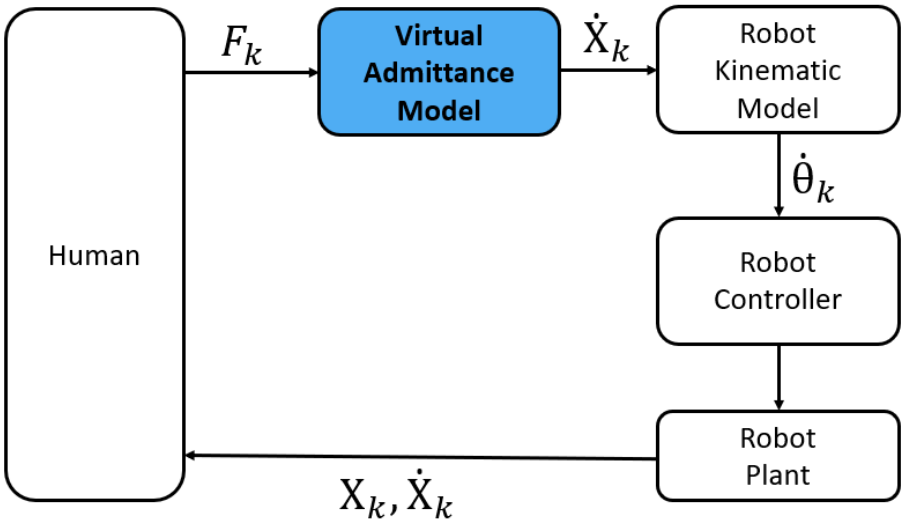

Figure 5.11: Block diagram of the admittance control framework

5.4 Admittance Control Framework

Under an admittance controller, the interaction forces exerted by the subject affect the motion of the robot though virtual model dynamics. The model dynamics are selected to achieve a desired interaction between the human and robot. Commonly, the input force is related to the robot velocity [96]. Our overall admittance control framework is shown in Figure 5.11.

Admittance control is the dual of impedance control, a form of interaction control first presented by Hogan [97]. Impedance control requires a system which is able to apply a force to the human in response to a displacement. Stepper motors cannot operate under low-level torque control, and therefore cannot be used to implement an impredance control architecture. Under an admittance controlled device, it is challenging to render low-inertia environments due to instability. To achieve free or *transparent* motion, we seek to achieve a low-inertia environment, minimizing the interaction force between the subject and device as they complete a motion. To maintain safe and stable interaction, however, we maintain an inertia which is lower than the mechanical friction of the system, but greater than a truly transparent system.

We relate our interaction force F to the robot velocity through the virtual dynamics of a mass-damper system. From Newton's 2nd law and a sum of forces, we can derive the differential equation for the position x:

$$m\ddot{x}(t) + c\dot{x}(t) = F(t) \tag{5.5}$$

where m is the mass and c is the damping coefficient. For implementation, we derive the discrete dynamics via backwards Euler discretization:

$$\dot{x}_k = \frac{\triangle t}{m} F_k + \left(1 - \frac{c \triangle t}{m}\right) \dot{X}_{k-1} \tag{5.6}$$

where $\triangle t$ is the control loop time step. We define controller parameters α_m and α_v to simplify the discussion of mass and viscosity:

$$\alpha_m = \frac{\triangle t}{m} \tag{5.7}$$

$$\alpha_v = \left(1 - \frac{c \triangle t}{m}\right) \tag{5.8}$$

Adjusting the mass and viscosity parameters affects the virtual dynamics of the human-robot-interactions. Increasing the mass parameter results in a decrease in the virtual mass mass. This will result in a more responsive system, requiring less force to achieve a given velocity. Increasing the viscosity parameter results in greater velocity carryover of the previous velocity state.

Upper Limb Inverse Kinematics

While the device measures end-effector position and forces, knowledge of the corresponding human joint angles and torques is useful in biomechanical analysis both as an assessment and as an input into assistive and rehabilitative controllers. In a lab setting, it is possible to track arm kinematics using an external camera or motion capture system. This increases the cost and setup time to acquire data in a clinical or home setting. The constraints of the system allow us to estimate the arm kinematics from minimal additional measurements. We model the human arm from the shoulder to the wrist as a five degree of freedom linkage consisting of a spherical shoulder joint, a cylindrical elbow joint, and a cylindrical joint for wrist pronation as shown in 5.12a. The inverse kinematic problem for this model seeks to find the joint angles given the position and orientation of the end-effector (wrist). From the device we have a measurement of the wrist position and an incomplete measurement of the wrist orientation. The z-axis of the wrist is fixed based on the angle of the wrist in the device. We can derive a closed-form solution for this IK problem, making the following assumptions:

1. The length of the upper and lower arm segments are known
2. The glenohumeral shoulder joint center (SJC) remains fixed (no scapular motion) and known
3. The forearm remains parallel to the horizontal plane

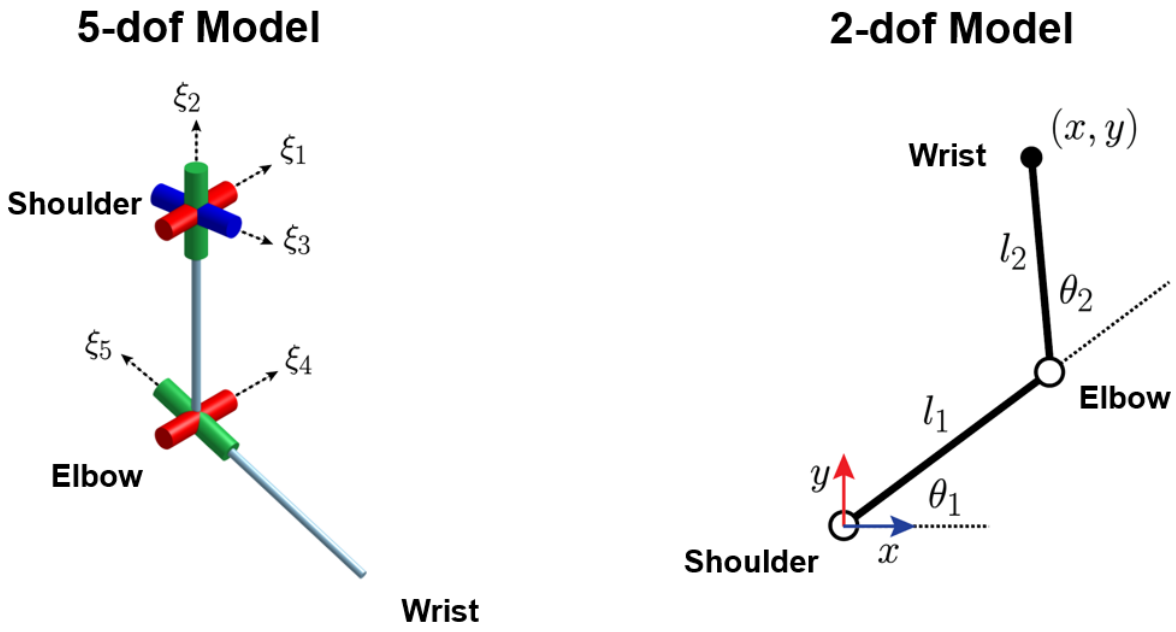

Figure 5.12: Rigid body models of the upper limb. Left: 5-dof model with a spherical shoulder joint, a cylindrical joint for elbow flexion/extension, and a cylindrical joint for wrist pronantion/supination. Right: planar 2-dof model of the arm with cylindrical joints at the shoulder and elbow for flexion/extension.

4. The orientation of the z-axis of the wrist frame remains remains fixed

We measure the position of the shoulder joint relative to the origin of the device. During experiments, we instruct subjects to keep their shoulders back to limit the use of scapular or torso motion. From this incomplete end-effector configuration, we derive a closed-form solution to the inverse kinematics problem using a Paden-Kahan approach for decomposition [67]. We break the derivation into down the following steps:

1. Solve for elbow flexion θ_4 based on distance from wrist to SJC (Paden-Kahan 3)
2. Project onto horizontal plane to solve for 2D position of elbow joint center
3. Solve for shoulder flexion (θ_1) and adduction (θ_3) to the set position of the elbow joint center (Paden-Kahan 2 and 1)
4. Solve for shoulder internal rotation (θ_2) to set the position of the wrist joint center
5. Solve for wrist pronation/supination (θ_5) to align z-axis of wrist frame

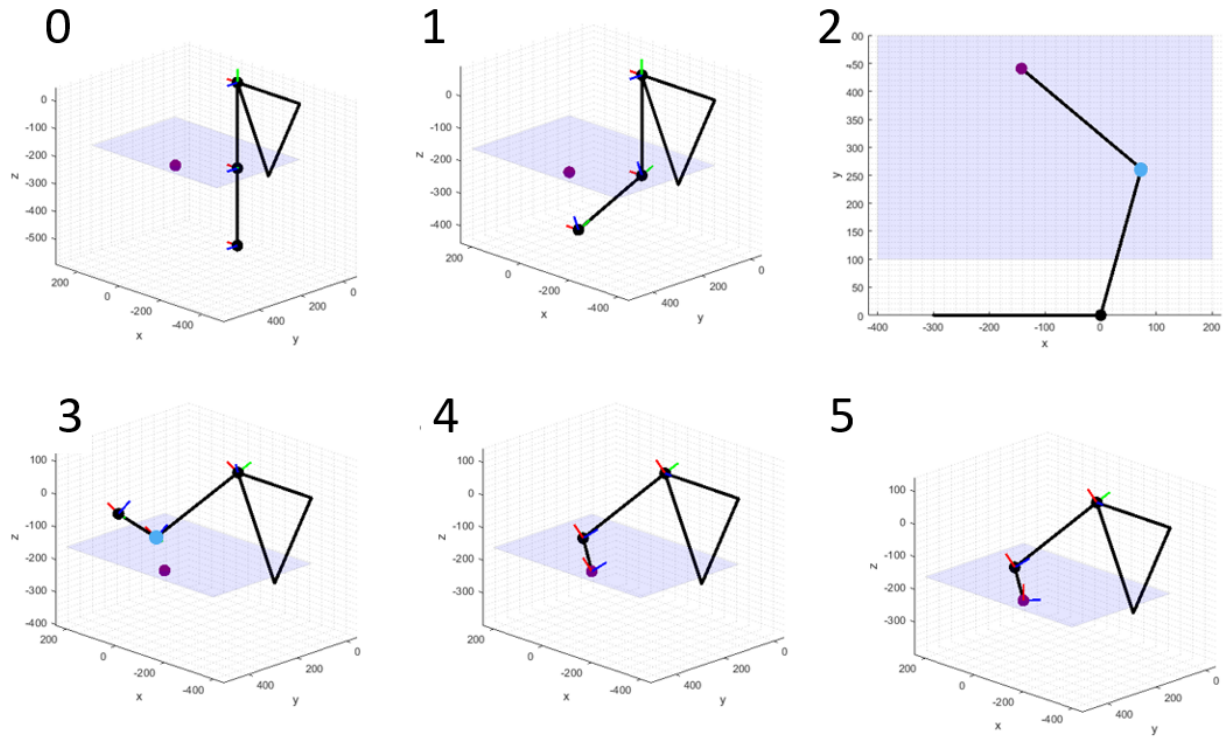

Figure 5.13: Figures illustrating the steps to solve to the inverse kinematics problem for the 5-dof upper-limb model. Step 0 shows the initial reference configuration for the arms. Figures 1 - 5 show the steps outlined in the text.

Operating the device at the subject's shoulder height simplifies the human kinematics. In practice, this is achieved by mounting the planar device on top of a variable height table and adjusting the table to be at shoulder height. We can now model the arm as a two-link planar linkage with a cylindrical joint at the shoulder and elbow (Figure 5.12b). Again assuming that the position of the shoulder and linkage lengths are known, we have a closed-form solution to the inverse kinematics problem [67]:

$$\theta_1 = \text{atan2}(y, x) \pm \cos^{-1}\left(\frac{r^2 + l_1^2 - l_2^2}{2 l_1 r}\right) \tag{5.9}$$

$$\theta_2 = \pi \pm \cos^{-1}\left(\frac{l_1^2 + l_2^2 - r^2}{2 l_1 l_2}\right) \tag{5.10}$$

where l_1 and l_2 are the lengths of the upper-arm and lower-arm segments, respectively, and $r = \sqrt{x^2 + y^2}$ is the distance from the wrist to the shoulder joint center.

Figure 5.14: Assistive glove

5.5 Preliminary Human Subjects Experiments

Preliminary experiments were conducted with a prototype version of the device described in this chapter. The notable differences between the prototype device and the described device are a slower control loop operating at 70 Hz and stepper motors with lower maximum torque. An objective of the experiments is to demonstrate the feasibility of the hardware setup and the use of admittance control for assistive and unconstrained movement. In addition, the experiments explored:

1. Differences in subject interaction during fully-assisted and admittance control
2. The effect of varying the virtual-mass damper dynamics on the interaction force and end-effector velocity
3. The effect of reaching verses reach-to-grasp on gross arm motion
4. The detection of the onset of grasp during a reach-to-grasp action

The experiments were conducted with the use of a prototype assistive glove (Figure 5.14), capable of flexing and extending the index finger to complete a pinch grasp while opposing a braced thumb. The active assistance is provided by a servo motor, whose output is connected in series with a 3D-printed rotational spring assembly. This configuration allows for the glove to operate under both an active assist mode and an admittance controller for volitional motion. While the device is not able to record absolute measurements of finger position or force, in the admittance control mode, the device is able to measure the times of grasp onset, peak opening, and closing. This allows for the stages of the grasp motion to be tracked relative to the gross arm motion. The thumb was braced with a modified finger splint to keep the thumb supported in opposition to the index finger to provide a precision pinch grasp.

Experimental Protocol

Data was collected from four control subjects and two subjects with upper limb impairment under approval of the UCSF Institutional Review Board with reliance approval by the UC Berkeley Institutional Review Board.

In the assisted mode, the device completes a linear minimum-jerk trajectory with no input from the human subject. The minimum-jerk trajectory was selected to follow a smooth velocity profile which has been found to describe a nominal trajectory for linear reaching [98]. For known start and end conditions and a specified duration, Hogan formulated the minimum jerk trajectory:

$$x(t) = x_i + (x_f - x_i)\left(10(t/d)^3 - 15(t/d)^4 + 6(t/d)\right) \tag{5.11}$$

where x_i is the initial position, x_f is the final position, and d is the total duration of the motion. Note that we can independently compute the minimum-jerk trajectory for the x and y dimensions. To implement this we take the first derivative of the discrete-time version of Equation 5.11 to compute the velocity based on the elapsed time. The trajectory is computed in real time with a proportional tracking term on the position error. In this mode, the human motion has no impact on the motion of the device. Subjects were instructed to follow the motion of the device with their arm, and the interaction forces were recorded. In the admittance control mode, the subjects control the motion of the device through the interaction force. Three combinations of mass and viscosity parameters were tested: A1) $m = 3.3$ kg, $\alpha_v = 0.25$, A2) $m = 3.3$ kg, $\alpha_v = 0.5$ A3) $m = 2.2$ kg, $\alpha_v = 0.5$.

All subjects were tested with their right arm in the device. This was the self-reported dominant arm for all subjects. The device origin was positioned in front of the subject's right shoulder joint center in the transverse plane. Targets were placed at three locations: at 0 degrees, 45 degrees, and 90 degrees from the origin. A foam ball of 1 in diameter was connected to a weak magnetic mount. The vertical height of the mount was adjusted so that subjects could grasp the object when connected to the device. Prior to the start of the experiment, the reachable workspace of each subject was manually measured by the experimenter along 8 radial lines from the origin. These measurements were used to set the reaching target distances along each of the target lines.

Trials were designated as reaching trials or reach-to grasp trials. During a reaching trial, the subject completed only the gross reaching motion. During a reach-to-grasp trial, the subject either grasped or released the ball at the end of the reaching trajectory. For all reach-to-grasp motions, the assistive glove operated under an admittance control mode. Each trial consisted of three outward reaches and three inward returns for each target. Each condition, reaching vs reach-to-grasp, assisted (two speeds), and admittance control parameter (3 combinations) was completed once. Subjects were given time to rest between sets of three trials.

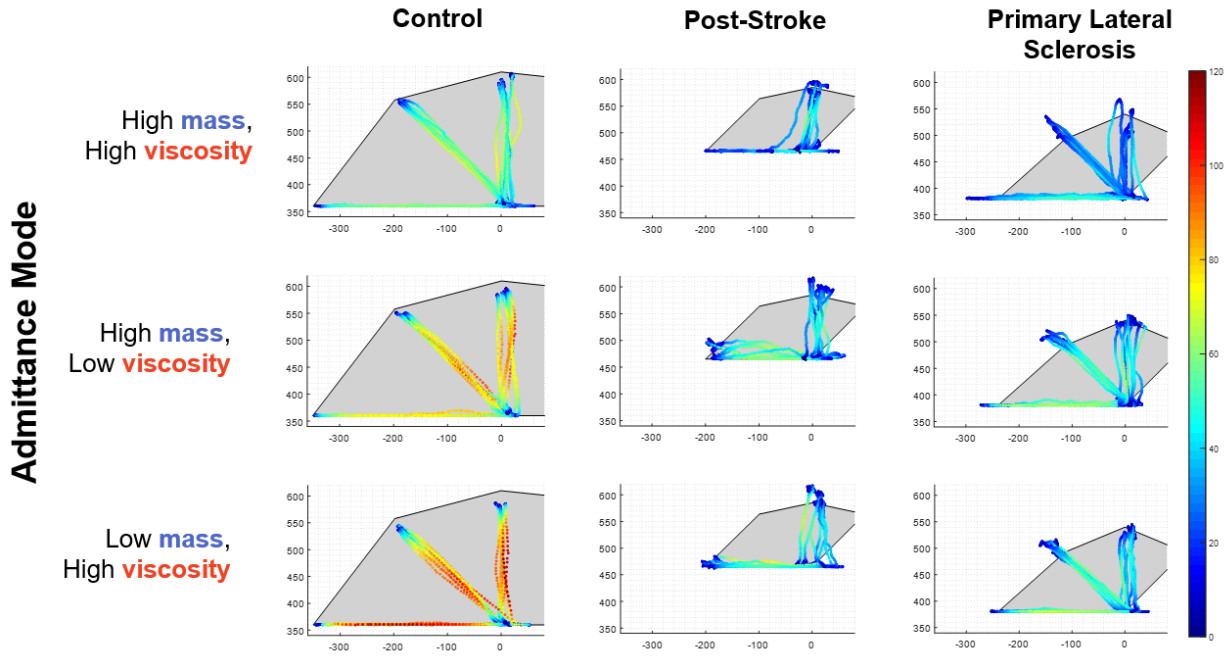

Figure 5.15: Top-down view of planar reaching trajectories for control (left), post-stroke (center), and PLS (right) subjects. The color of each line corresponds to the velocity of the wrist at that point. Subjects performed series of reaches from the home position to radially placed targets. The subject's reachable workspace as measured by clinician is depicted in gray.

Results

Our analysis of this preliminary protocol is largely qualitative as the primary purpose was to assess the hardware feasibility. Figure 5.15 shows sample reaching trajectories from trials under the admittance controller, comparing the motion of a representative control subject, a subject who is post-stroke, and a subject with early Primary Lateral Sclerosis (PLS). We observe variation in the velocity profile and peak speed during the gross transport phase, the ability of the subject to stabilize their arm at the end of the motion, and the linearity and smoothness of the reaching trajectory. These differences were noted despite the subject with a diagnosis of PLS having a high level of functional ability. On examination, this participant had mild bilateral distal upper limb weakness (MRC scale 4/5), mildly elevated tone, and full passive and active range of motion. Changes in the linearity of a reach or reach-to-grasp trajectory have been associated with cerebellar pathologies, leading to separation of the motions of the shoulder and elbow. Prior research has shown that the reaching motions of post-stroke subjects with upper limb impairment are slower, less accurate, and have poorer coordination than non-impaired individuals. Our anecdotal results appear to agree with

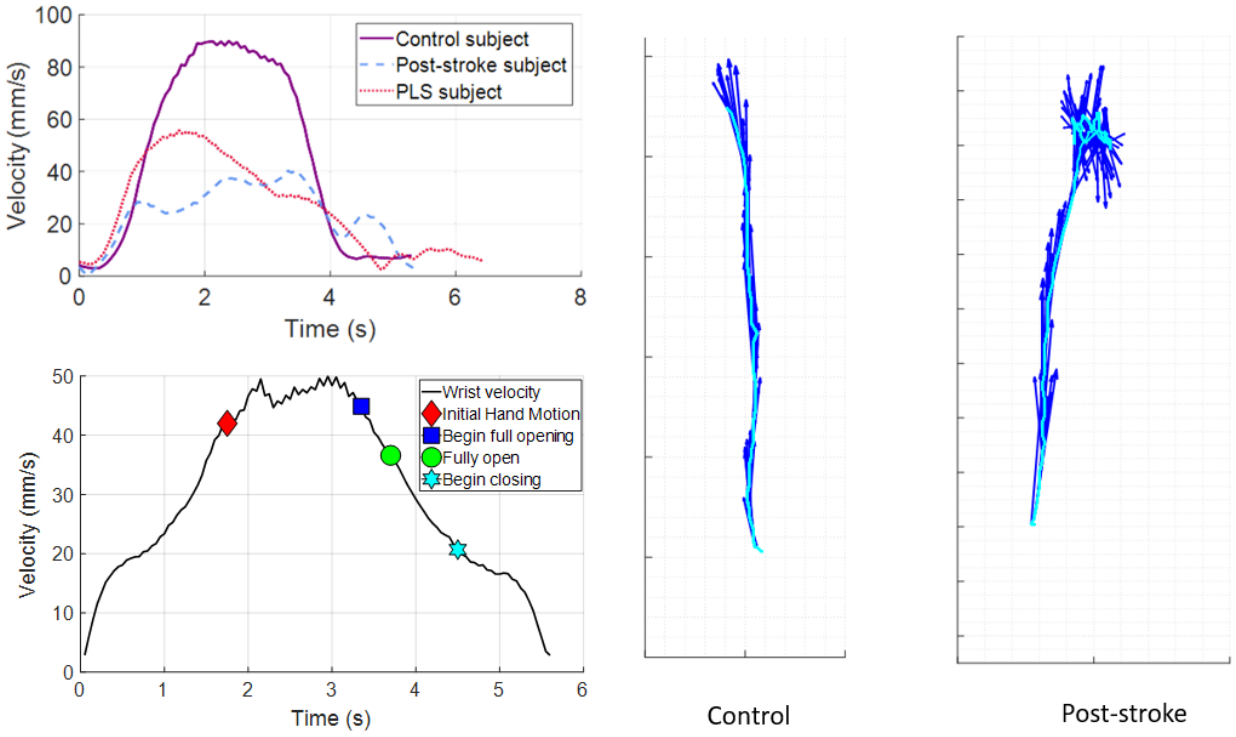

Figure 5.16: Preliminary observations from the human subject protocol. Top left: representative velocity plots for a single reaching motion for control subject (purple), post-stroke subject (blue), and subject with Primary Lateral Sclerosis (Red). Bottom left: demonstration of feasibility to identify key stages of grasp during a reach-to-grasp motion. Right: representative trajectory for a forward reaching motion for a control subject (left) and a post-stroke subject (right), illustrating inability to stabilize at the trajectory endpoint.

these findings.

Figure 5.16 summarizes several observations from the protocol. We show a sample velocity profile for a representative control subject and the two subjects with upper-limb impairment. The velocity profile for the control subjects has a higher peak velocity and exhibits the expected bell-curve shape associated with a smooth, minimum-jerk trajectory. In contrast, the velocity of the two subjects with upper limb impairment does not have a single peak, but rather has a smaller period of acceleration followed by multiple peaks. This is more pronounced in the post-stroke subject than the subject with early PLS. This behavior is consistent with the theory of submovments affecting movement smoothness following stroke [99]. The trajectory plots on the right of Figure 5.16 illustrate instability when the post-stroke subject attempted to remain steady at the end of a reaching motion. This instability was not seen in any of the control subjects and indicates decreased ability to perform precise control and regulate arm stiffness.

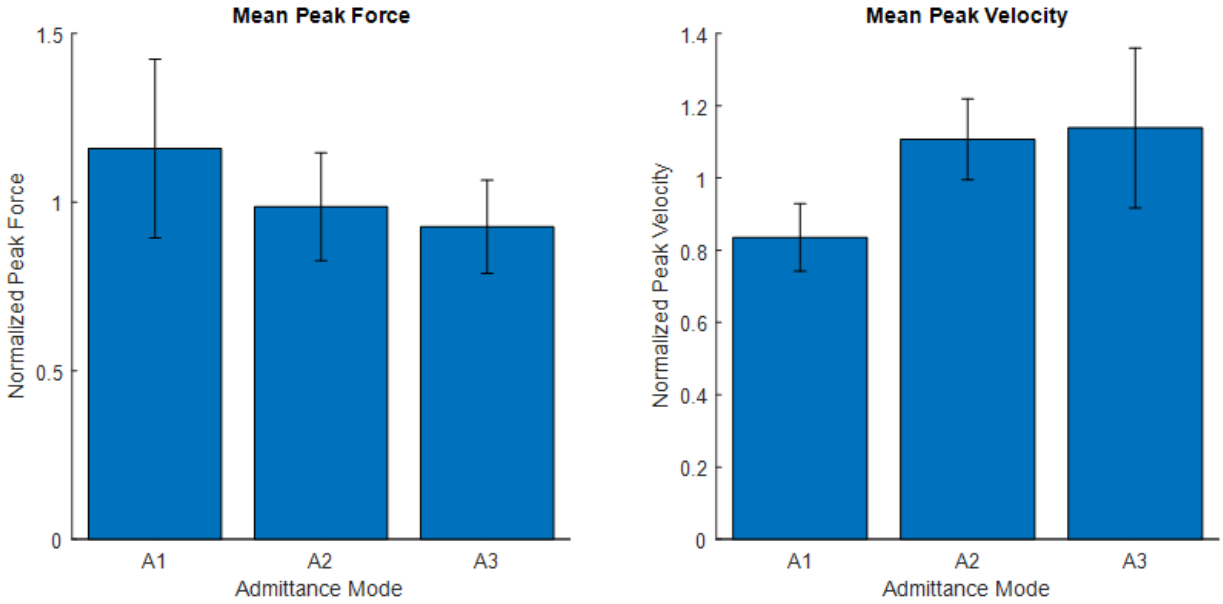

Figure 5.17: Bar charts showing mean peak force (left) and mean peak velocity (right) for healthy controls subejcts completing reaching trials under the different admittance controller virtual dynamics. Peak force and velocity values are normalized to the subject mean. Values represents the mean across the subjects with the error bar corresponding to inter-subject variance. The admittance mode virtual dynamics were defined by the following parameters: A1) $m = 3.3$ kg, $\alpha_v = 0.25$, A2) $m = 3.3$ kg, $\alpha_v = 0.5$ A3) $m = 2.2$ kg, $\alpha_v = 0.5$.

We demonstrate the ability to synchronize analysis of the global reaching motion with the action of the hand (Figure 5.16). Based on position data recorded from the glove device, we identify four key points in the grasping motion: 1) initial hand motion, 2)begin fully open, 3) fully open, 4) begin closing. Because of the small difference in position between beginning to close and the final closed position, it was difficult to identify the time of grasp completion. This is a limitation of the low resolution of the position sensing of the glove device. Information of the grasping motion related to the reaching motion is useful in the study of motor recovery following stroke. In normal reach-to-grasp motion, subjects preshape the hand prior to reaching the end of the reaching trajectory to prepare to grasp the object. Quantitative analysis of these onset times is not included.

Finally, we analyze the effect of altering the virtual dynamics for the admittance control trials for the control subjects. We consider two values: the peak interaction force and the peak velocity for each reaching motion. We compare the values for outward reaching to the target at 45 degrees. To analyze trends across subjects, the values for each subject are normalized with respect to the subjects mean value across each trial. The mean values are shown in Figure 5.17 with the standard deviation corresponding to the variance between

subjects. A1, the controller with a heavier virtual mass, has a higher mean peak force and a lower mean peak velocity. These results demonstrate that it is possible to alter the human interaction with the device by altering the virtual dynamics. We asked subjects for their preference among the three admittance control virtual dynamics. Of note, all healthy control subjects selected either A2 or A3, citing the ability to move at a faster speed. Both subjects with upper limb impairment selected A1. For both subjects, A1 required more force and took a longer period of time to complete the motion. However subjects cited feeling more stable as the reason for their preference.

5.6 Simulation Case Study: Effect of Passive Flexor Muscle Tightness on Joint Torques During Planar Arm Reaching

We now consider the incorporation of a muscle model into our analysis with the developed system. Preliminary reaching data from a Spinal Cord Injury (SCI) subject was collected under approval of the UCSF Institutional Review Board. Example data is shown in Figure 5.18. With the goal of using this robotic device to assess function and assist motion, this study implements a simple biomechanical model which can be incorporated in the analysis of data from the device. Spinal Cord Injury (SCI) may result in impaired function of the upper limb including decreased range of motion due to an increased passive stiffness of the flexor muscles accompanied by deficits in strength. In this case study, we utilize a six-muscle model of the arm to simulate passive muscle forces during reaching motions in the horizontal plane. We study the effect of muscle-level tightness on the resultant elbow and shoulder torques throughout the arm workspace. The resulting joint torques exhibit an expected increase with greater muscle tightness, with this effect most pronounced in lateral reaching motions. These results demonstrate initial feasibility of the use of a simplified muscle model to study joint effects of muscle-tightness, providing insight towards the future development of assessment protocols for generating individualized models of function from task-space observations. Alongside deficits in strength and motor control, SCI may result in tightness of the flexor muscles, resulting in a decrease in range of motion [100]. An increase in passive muscle stiffness and connective tissue of the flexors must be overcome by the active muscle force of the opposing extensor muscles. In this work, we study the effects of muscle tightness on the resultant joint-torques from passive muscle forces during static reaching. This analysis provides insight into how the passive component of muscle force manifests in the joint and task space.

Methods

We consider a two-link model of the upper-limb (right arm) with rotational joints at the shoulder and elbow. Motion is constrained to the tranverse plane at shoulder-height, and

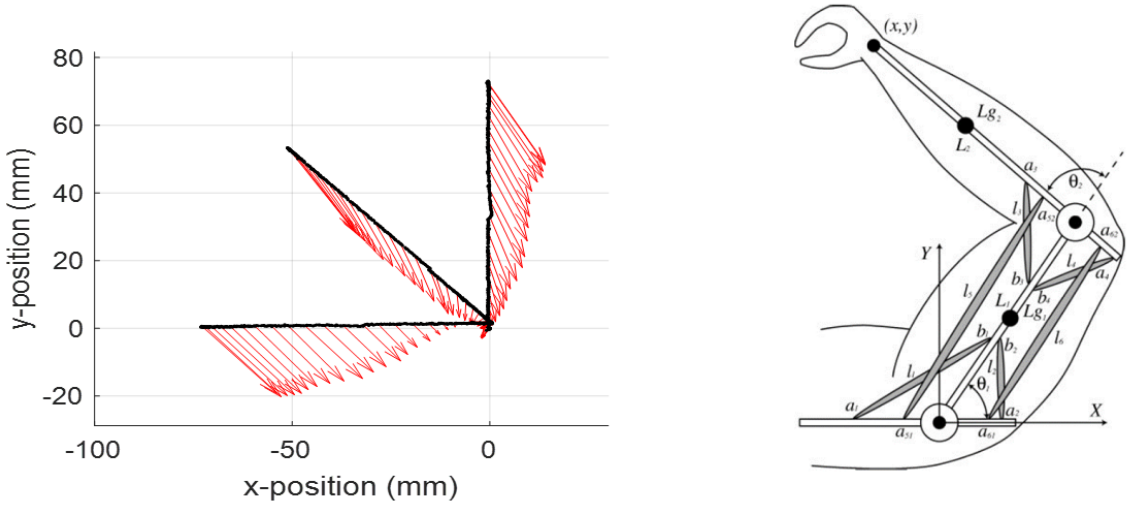

Figure 5.18: Left: representative reaching data from a subject with spinal cord injury undergoing passive reaching to three radial targets. Wrist position is shown in black with the interaction force shown as the scaled red vector. Right: musculosketal arm model. Figure from [101].

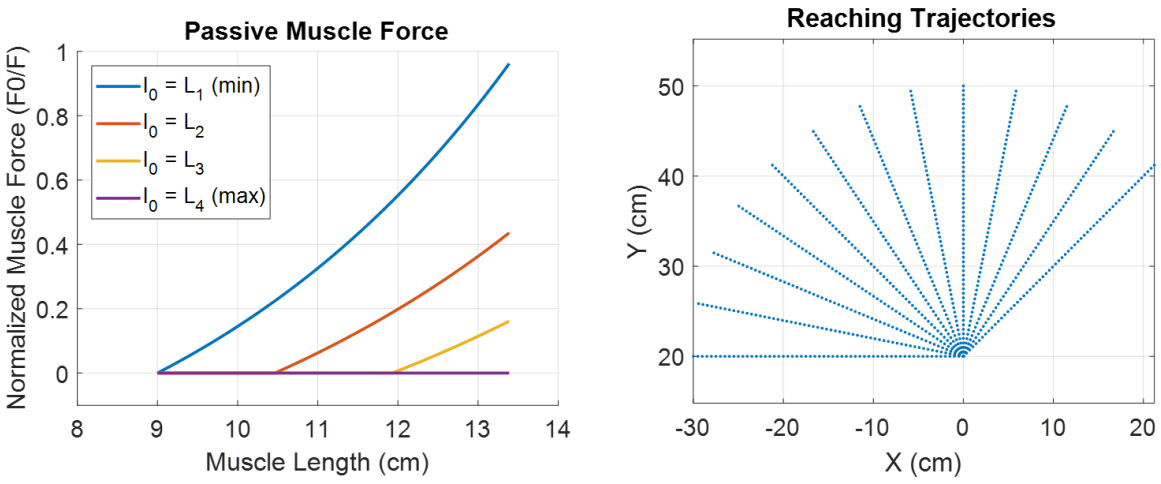

Figure 5.19: (Left) Passive muscle force vs. muscle length. Relationship is shown for four values of nominal muscle length l0. (Right) Simulated wrist positions for reaching trajectories in Cartesian space.

we assume that the arm is supported vertically, neglecting the effect of gravity. The model consists of a lumped-muscle model with six redundant muscles: a mono-articular pair of flexor and extensor at the elbow (brachialis and lateral head of triceps brachii) and at the shoulder (pectoralis major and posterior deltoid) and one bi-articular pair which spans the shoulder and elbows (biceps bracii and long head of triceps) specified in [102].The model geometry is configuration is shown in Figure 5.18. Model parameters including limb length and muscle origin and insertions were taken from [101]. From the Cartesian wrist position, we recover the planar kinematics given known shoulder position and arm lengths, using an analytical inverse kinematic solution. Muscle lengths are computed from the kinematics, assuming the muscle acts along a straight line between the instantaneous position of the origin and insertion points. Variable moment arms for the flexor muscles are computed for the respective elbow and shoulder joints, dependent on the angle between the line of muscle force and the line between the muscle insertion and joint center. The extensor muscles are modeled as a pulley with fixed moment arm (2 cm at the elbow and 4 cm at the shoulder).

The passive muscle force $F(l)$ can be expressed as a function of the muscle length with a Hill-type model as follows:

$$F(l) = \begin{cases} 0 & l < l_0 \\ \frac{F_0}{e^{K_{sh}-1}} \left(e^{\frac{K_{sh}(l-l_0)}{0.5 l_0}} - 1 \right) & l \geq l_0 \end{cases} \tag{5.12}$$

where we set stiffness constant $K_{sh} = 1$ for all muscles [103]. The passive muscle force has an exponential relationship with muscle length which begins when the muscle extends beyond the nominal muscle length l_0.

To modify the muscle tightness, we adjust this nominal muscle length. For each of the flexor muscles, we consider four values of nominal length, equally spaced between the minimum and maximum length observed throughout the workspace. For the extensor muscles, we select a fixed nominal length equal to the mean muscle length throughout the workspace. Figure 5.19 (left) shows the passive muscle force for a single muscle with the different nominal length. We consider only the passive muscle forces and assume static configuration to neglect the dynamics and viscous effect of muscle velocity. For each muscle, we can compute the joint torque τ generated by the muscle force F_m for moment arm r.

$$\tau = F_m r \tag{5.13}$$

The force at the wrist can then be computed from the combination of the shoulder and elbow torques, related by the manipulator Jacobian.

Static reaching along straight lines was simulated for radial targets defined in the Cartesian space with an origin 20 cm directly in front of the shoulder joint center with radii sampled from 0 to 30 cm at angles between 50 and 180 degrees from the horizontal axis (Fig 5.19 - right). We compute the passive muscle forces and resultant joint torque for each static configuration. Along each radial trajectory, we find the maximum elbow and shoulder joint torque in the extension direction along the line. This analysis is performed for four

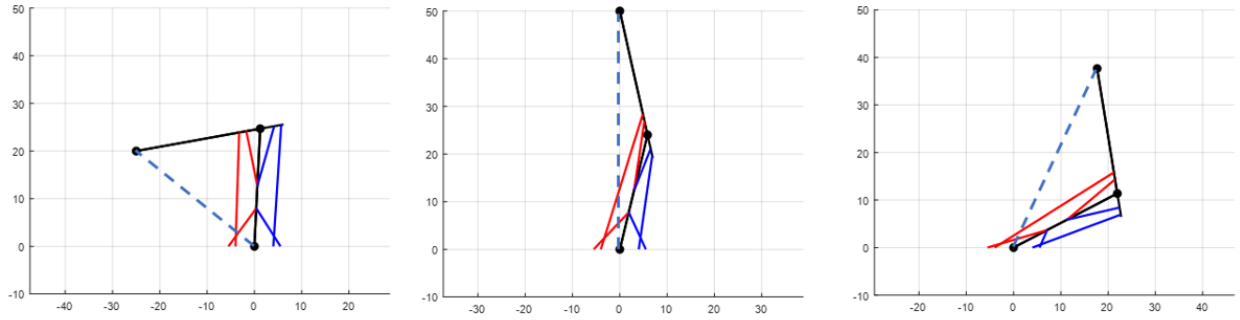

Figure 5.20: Kinematic configuration at three arm configurations along reaching trajectories in the left, center, and right directions. Arm links are shown in black with flexor muscles in red and extensor muscles in blue. The reaching trajectory is shown as the dashed line.

nominal muscle for each of the mono-articular elbow flexor, shoulder flexor, and bi-articular flexor individually and for increased tightness and all three flexors. All computations were completed in MATLAB 2017a.

Representative kinematic configurations of the arm model are shown in Figure 5.20, illustrating the changes in muscles length. The maximum resultant joint torques for the four muscle tightness conditions are shown in Figure 5.21. Adjusting the nominal muscle length of the shoulder flexors has expected changes in shoulder torque and does not affect the elbow torque. The same effect is observed when only the elbow flexor tightness is modified. Adjusting the tightness of the bi-articular muscle results in torque effects in both the shoulder and elbow. The greatest torque is seen when all three flexor muscles have increased tightness.

Discussion

We implemented an upper limb musculoskeletal model with six muscles to assess the effect of passive muscle tightness on joint torques. The results demonstrate expected increases in elbow and shoulder torques with increases in flexor muscle tightness. The effect of the bi-articular muscle on both elbow and shoulder joints indicates a usefulness in the incorporation of a muscle-level model in this analysis rather than a simple rotational stiffness at the joint-level. Additionally, the effects of the muscle parameters are observed to vary within the workspace, with greater torque at the most lateral target as both the shoulder and elbow flexors are extended in this arm configuration. This result implies that it is valuable to consider mechanical constraints at the muscle-level effects when developing controllers that will operate in the Cartesian workspace. Assessment of active range of motion, convey limitations due to a combination of passive stiffness and deficits in active muscle force generation The analysis in the study is limited as we consider only the passive component of muscle force for a simplified muscle model. The total muscle force must be modeled as a combination of

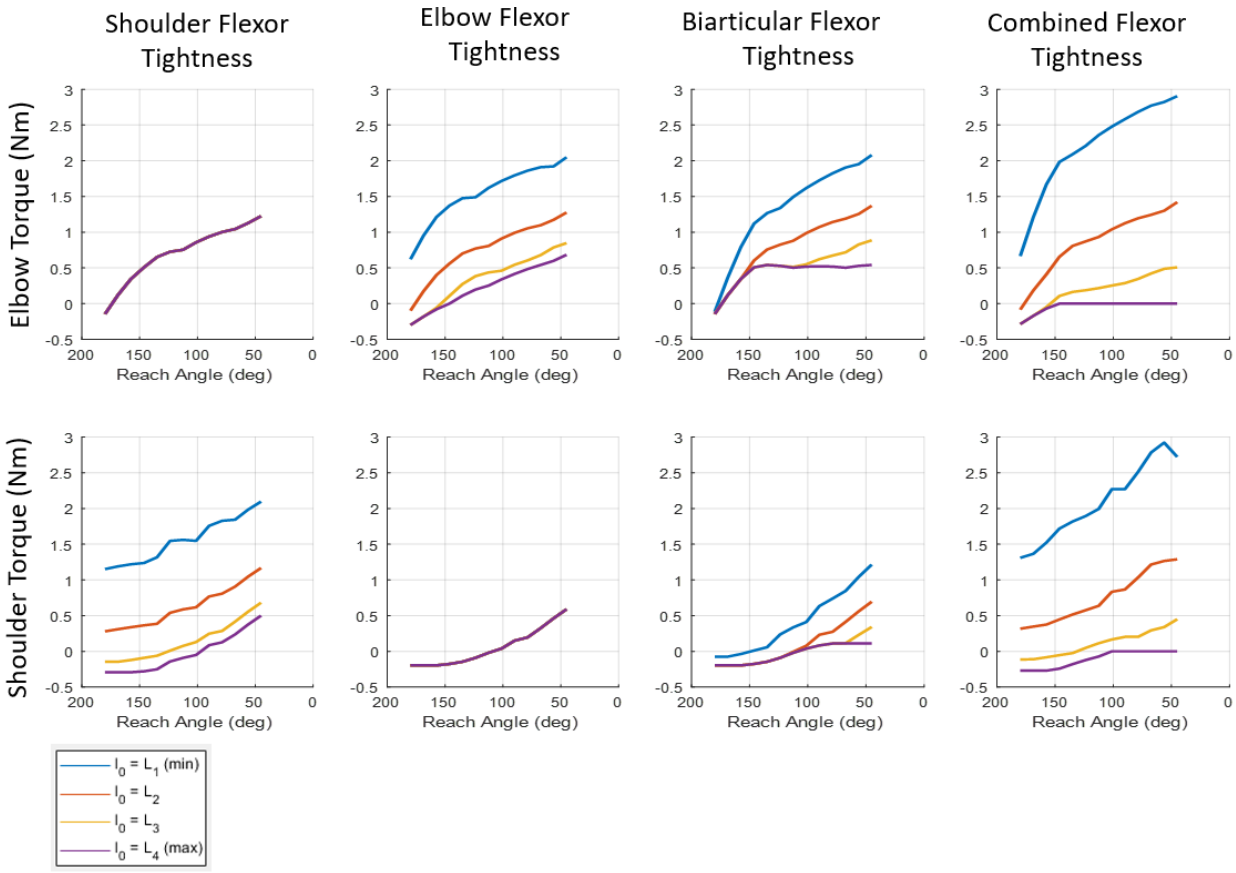

Figure 5.21: Resultant maximum torques at the elbow (top row) and shoulder (bottom row) for muscle tightness conditions. The nomical muscle length L1 corresponds to the shortest muscle length, with L4 being the greatest. Torques are plotted as the maximum value for a given reaching angle defined in the Cartesian space between the wrist position and the horizontal line through the center point.

active and passive muscle forces. While it is straightforward to implement the forward model with specified values of nominal muscle length, it is difficult to separately assess the passive and active components of muscle force. However, given the joint-specific and workspace variations, the preliminary results of this parameter study indicate that for passive motion we may be able to identify optimal muscle-model parameters which correspond to the observed end-effector forces. Future work will aim to utilize this model of passive muscle forces to drive subject specific models of impairment using task-space observations of motion and force with a planar robotic device.

5.7 Chapter Summary

This chapter presented the design, analysis, and validation of an affordable planar robotic device for upper limb assessment and rehabilitation. With a total material cost of less than $800, the device was able to meet our design objectives. We introduce a novel configuration for low-cost load cells, enabling measurement of human-robot interaction forces. The measured forces and positions recorded by the device were experimentally validated against ground truth measurements. Initial human subjects experiments demonstrated device feasibility through the subject ability to operate the device under volitional force-based admittance control. We observed differences in the robot interaction of healthy control subjects and subjects with a low-level of impairment, with notable differences in peak forces and velocities, motion smoothness, the ability to stabilize, and the self-selected preferable virtual dynamics.

Chapter 6

Algorithms for Assistance and Assessment

In this chapter, we utilize the robotic device developed in Chapter 5 to investigate two methods for assisting and assessing human motion: 1) the use of lateral spring assistance during elliptical trajectory tracing and 2) the assessment of arm strength through isolated joint motions. We describe our motivation, design, and implementation for each of protocol and present analysis of human subject data. These results further demonstrate the capabilities of the affordable device for quantitative assessment and robotic therapy applications.

6.1 Exploitation of Assistance During Ellipse Tracing

Motivation and Background

During the preliminary experiments (Section 5.5), we observed a behavior in which subjects were *leaning into* a virtual safety wall by exerting a large interaction force in the direction of the wall, normal to the direction of the desired trajectory. Subjects were not generally assisted in completing the protocol under an admittance controller. There were, however, force fields at the edge of the human workspace which prevented the subject from reaching outside of a safe region. The target to the left was positioned along the virtual wall, with a straight line from the starting point to the target running along the wall. This unintentionally resulted in several subjects exploiting the presence of the virtual wall by exerting a force in the direction of the wall to maintain a stable trajectory. An example of this behavior is shown in Figure 6.1. This figure shows data from a subject with upper-limb impairment, following diagnosis of Primary Lateral Sclerosis. Here we observe variance in the position trajectories for the vertical and 45 degree targets. The left target of interest has almost no variance. Additionally, from the overlaid velocity profile, we observe higher peak velocities along the left target, indicating higher forces directed along the line of interest. This can be explained by the plot to the right which shows the interaction force exerted by the subject.

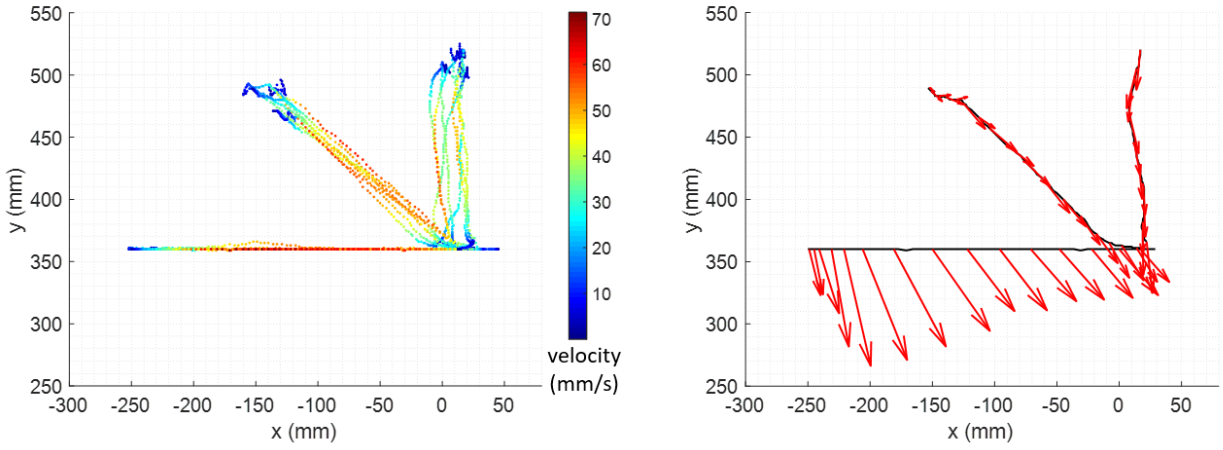

Figure 6.1: Sample of the data from preliminary experiment demonstrating subject leaning into force field during reaching. (Left) Top-down view of reaching trajectories to targets at 0, 45, and 90 degrees from the vertical. The velocity at the point is represented by the color. (Right) Sampled interaction force overlaid on top of reaching trajectory.

For the targets at 0 and 45 degrees, the force exerted by the subject primarily lies along the line from the start position to the goal. The interaction force of the lower trajectory, however, has a large component normal to the desired trajectory, pointing into the wall.

These forces allow the subject to stabilize their trajectory, requiring less precise end-effector forces. The subject appears to intentionally lean in to the wall, exploiting its unintentional assistance to complete the motion with less precise control. This not only resulted in greater forces in the normal direction, but also greater forces in the in the correct direction and a faster total motion. The use of virtual walls along the trajectory or spring forces acting normal to the trajectory is not a new concept and has been seen in several studies [104, 84]. In fact, this behavior of motor slacking to minimize energy resulting in over-reliance on assistance has been observed [105]. This led to the implementation of virtual tunnels, a deadband of specified dimensions surrounding the desired trajectory in which no assistive force is applied. This is one example of an *assist-as-needed* paradigm for robotic rehabilitation. Subjects are not assisted in completing the task unless they surpass an error threshold in space or time. This has benefit in promoting subject engagement which has been shown to be an important factor in treatment efficacy. Other methods have been implemented to decrease the assistance in response to subject performance in order to promote engagement in the protocol [84, 106].

While the tunnel method and decreased assistance promote *correct* motion, we hypothesize that there is benefit in allowing subjects to exploit an assistive force field. Consider a subject limited by a deficit in muscle synergy coordination but with adequate strength.

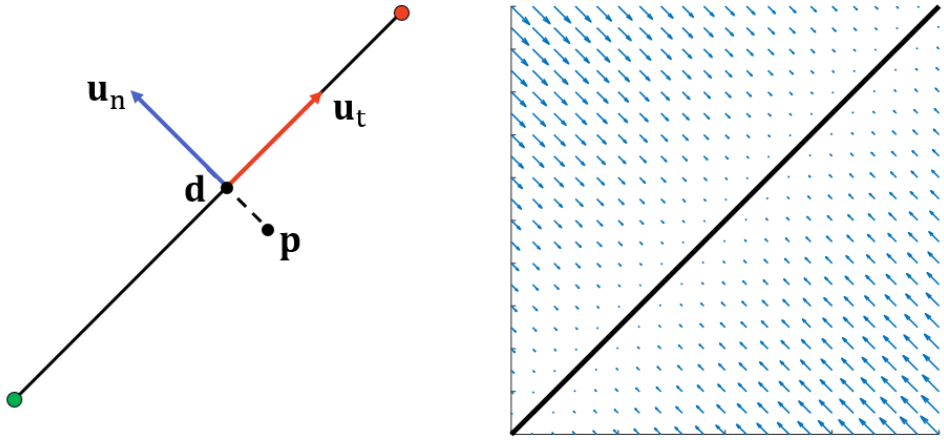

Figure 6.2: Left: drawing of the tangent-normal coordinate frame for linear spring assistance, showing the unit and normal tangent vectors, u_n and u_t, current position p and desired position d. Right: plot of the vector field of the linear spring assistance for a linear desired trajectory.

Operating within the deadband of a tunnel, the subject may complete slow, disjoint motions due to their inability to precisely regulate the direction of their end-effector force output. With an assistive wall, we hypothesize that the subject may be able to more confidently exert greater force and complete a faster, smoother motion. We present an experiment to investigate this approach when applied to continuous elliptical trajectories.

6.2 Spring Assistance Formulation

Building on the free admittance control framework presented in section 5.4, we incorporate an assistive spring term into the mass-damper virtual dynamics model. In this section, we first explain the controller implementation for a linear trajectory and then expand to the elliptical trajectories studied in this chapter. We consider a desired trajectory with a spatial component and no specified velocity profile for self-paced motion under admittance control. The assistance helps the subject follow the desired trajectory by applying a restoring force when the subject deviates from the trajectory. We implement this through a virtual linear spring acting in the direction normal to the trajectory. If the subject has no position error, the spring will provide zero force. Likewise, the spring provides no assistance along the forward direction of the trajectory. This type of assistance does not perform the task for the subject but, rather, assists in error correction. A linear spring was selected rather than a hard virtual wall to allow for some deviation without a strong restoring force. While we did not implement a virtual tunnel deadband to encourage the exploitation of the assistance, it would be straightforward to incorporate a deadband as an alternative protocol.

To implement these dynamics, we first perform a transformation from the device Cartesian coordinate system into the instantaneous tangent-normal coordinate frame of the desired trajectory. The normal vector is perpendicular to the tangent vector at a counterclockwise rotation of 90 degrees. We define the unit tangent vector $\mathbf{u}_t$ and unit normal vector $\mathbf{u}_n$ to be tangent and normal to the trajectory. For a line, the tangent-normal frame has fixed orientation with the tangent axis colinear with the trajectory. The spring acts in the direction of $\mathbf{u}_n$ with force proportional to the distance from the trajectory along $\mathbf{u}_n$:

$$F_{spring} = -k\left(\mathbf{p} - \mathbf{d}\right) \cdot \mathbf{u}_n \tag{6.1}$$

where $\mathbf{p}$ is the current position, $\mathbf{d}$ is the nearest position on the desired trajectory, and k is a spring constant chosen for selected stiffness level. Note that the formulation of this spring force differs slightly from the standard form [107] through the vector dot product with the unit normal vector. Our formulation was selected for expansion to elliptical trajectories when the approximated unit normal vector may not be collinear with $\mathbf{p} - \mathbf{d}$. We now represent our admittance controller with virtual mass-spring-damper dynamics in tangent normal coordinates:

$$F_n = m\ddot{x}_n(t) + c\dot{x}_n(t) - k(\mathbf{p} - \mathbf{d}) \cdot \mathbf{u}_n \tag{6.2}$$

$$F_t = m\ddot{x}_t(t) + c\dot{x}_t(t) \tag{6.3}$$

where the subscripts n and t denote the normal and tangent directions for the force, acceleration, and velocity. Note that there is no spring force in the tangent direction. The virtual mass and damper constants are the same for the normal and tangent directions. Controller velocities computed in the normal-tangent frame are transformed to the Cartesian frame.

Spring Assistance for an Elliptical Trajectory

Implementation of the linear spring force on an elliptical trajectory requires computation of the instantaneous tangent and normal vectors to the ellipse at a given point. Consider a standard ellipse defined the following parametric equation:

$$\begin{bmatrix} x \\ y \end{bmatrix} = \begin{bmatrix} a\cos\left(t\right) \\ b\sin\left(t\right) \end{bmatrix} \tag{6.4}$$

for $0 \leq t \leq 2\pi$, where x and y correspond to the position, a is the length of the semi-major axis, and b is the length of the semi-minor axis. We derive the tangent to an ellipse at a point d which lies on the ellipse. The slope of the tangent line is the first derivative at the point. First, take the first derivative of Eq. 6.4:

$$\begin{bmatrix} \dot{x} \\ \dot{y} \end{bmatrix} = \begin{bmatrix} a\sin\left(t\right) \\ b\cos\left(t\right) \end{bmatrix} \tag{6.5}$$

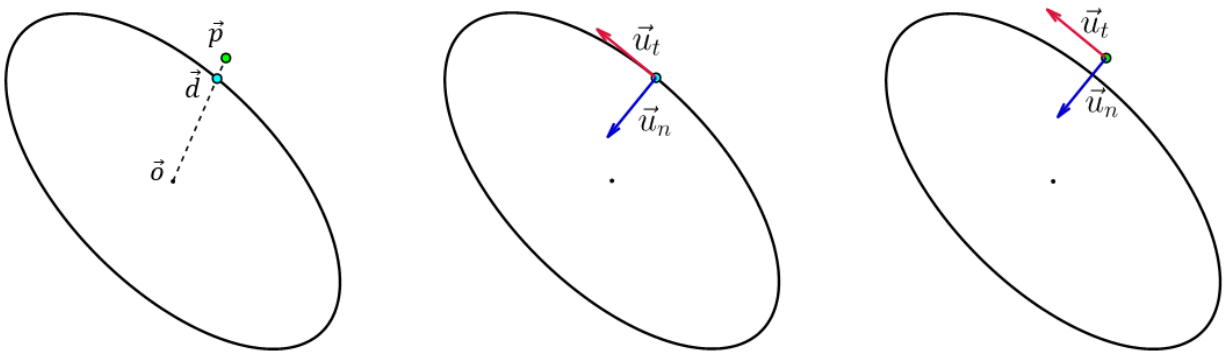

Figure 6.3: Illustration of the method for determining the unit tangent vector $\mathbf{u}_t$ and unit normal vector$\mathbf{u}_n$ at a point p when tracking an elliptical trajectory. (Left) Finding the desired point d, (Center) Computing the unit tangent and unit normal vectors at the desired position, (Right) Translating the tangent-normal coordinate frame to the current position.

Rearranging Eq. 6.4, we have $cos(t) = x/a$ and $sin(t) = y/b$. These relationships are combined with 6.5 to obtain the tangent vector $\mathbf{v}_t$:

$$\mathbf{v}_t = \begin{bmatrix} \frac{-ay}{b} \\ \frac{bx}{a} \end{bmatrix} \tag{6.6}$$

and unit tangent vector:

$$\mathbf{u}_t = \frac{\mathbf{v}_t}{\|\mathbf{v}_t\|} = \begin{bmatrix} \frac{-a^2y}{\sqrt{a^4y^2+b^4x^2}} \\ \frac{b^2x}{\sqrt{a^4y^2+b^4x^2}} \end{bmatrix} \tag{6.7}$$

The unit normal vector is perpendicular to the unit tangent vector, pointing into the curve. We can compute the unit normal with the following equation:

$$\mathbf{u}_n = \begin{bmatrix} -\mathbf{u}_{ty} \\ \mathbf{u}_{tx} \end{bmatrix} = \begin{bmatrix} \frac{-b^2x}{\sqrt{a^4y^2+b^4x^2}} \\ \frac{-a^2y}{\sqrt{a^4y^2+b^4x^2}} \end{bmatrix} \tag{6.8}$$

We transform the forces measured in the Cartesian frame into the tangent-normal frame with the equation:

$$\begin{bmatrix} f_t \\ f_n \end{bmatrix} = \begin{bmatrix} \mathbf{u}_t & \mathbf{u}_n \end{bmatrix}^T \begin{bmatrix} f_x \\ f_y \end{bmatrix} \tag{6.9}$$

For a point p which does not lie on the ellipse, we select the desired point d on the ellipse to be the intersection of the ellipse and a line between p and o, the ellipse origin. The position of the point d is expressed by the equation:

$$d = \begin{bmatrix} \frac{abp_x}{a^2p+y^2+b^2p_x^2} \\ \frac{abp_y}{a^2p+y^2+b^2p_x^2} \end{bmatrix} \tag{6.10}$$

Note that for the general case of an ellipse, the point d is not the closest point to the ellipse, but rather it is along the radial line from the origin. For the specific case of a circle, these points will be the same. The closest point to the ellipse does not have a closed-form solution. It can be solved with numerical optimization, but this was not chosen for our implementation to decrease the computational complexity as these constraints are being performed in realtime on an inexpensive microcontroller. We compute the unit tangent and unit normal vectors at the point d. These vectors approximate the unit tangent and normal vector for the point p which is not on the ellipse. The spring force acts along the unit normal vector from the point p toward the elliptical path. The vector field of spring force is plotted in Figure 6.4.

6.3 Experimental Protocol

Our experimental protocol was selected to study human interaction with the system under assisted and unassisted control. We hypothesize that the presence of a stiff assistive force field will result in the leaning in behavior observed in the linear reaching experiments. Subjects completed ellipsoidal trajectories with the device operating under an admittance controller. We consider three independent variables: admittance control virtual mass, spring assistance, and ellipse orientation. Two values of virtual mass (0.47 kg and 0.92 kg) were selected. The lower mass provides a lighter, more transparent motion. This lighter mass was selected to be so light that it may feel slightly unstable but not result in significant oscillations. The four ellipse orientations are rotations of 0, 45, 90, and -45 degrees from the vertical. A single spring constant of $k_s = 1$ was selected for the assisted case. No spring force was applied for the unassisted case. The combinations of variables correspond to a total of 16 unique test conditions. Subjects completed 3 trials of each of conditions, resulting in 48 total trials. Note that one subject completed only 32 trials (two of each condition) due to a time constraint on the part of the subject. Trials were broken into blocks of four trials which consisted of one trial for each ellipse orientation for a given mass and assistance condition. Subjects were informed if the trial would be assisted or unassisted. The order of the ellipse orientation was randomized. Each trial consisted of 10 ellipses, beginning and ending at the vertex. The ellipses were defined by semi-major axis a = 100 and semi-minor axis b = 50. The first and last ellipse were excluded from each trial during analysis to account for effects of initial acceleration or adjustment and final deceleration. All trajectories were completed in a counter-clockwise direction. The desired ellipse was displayed on a monitor

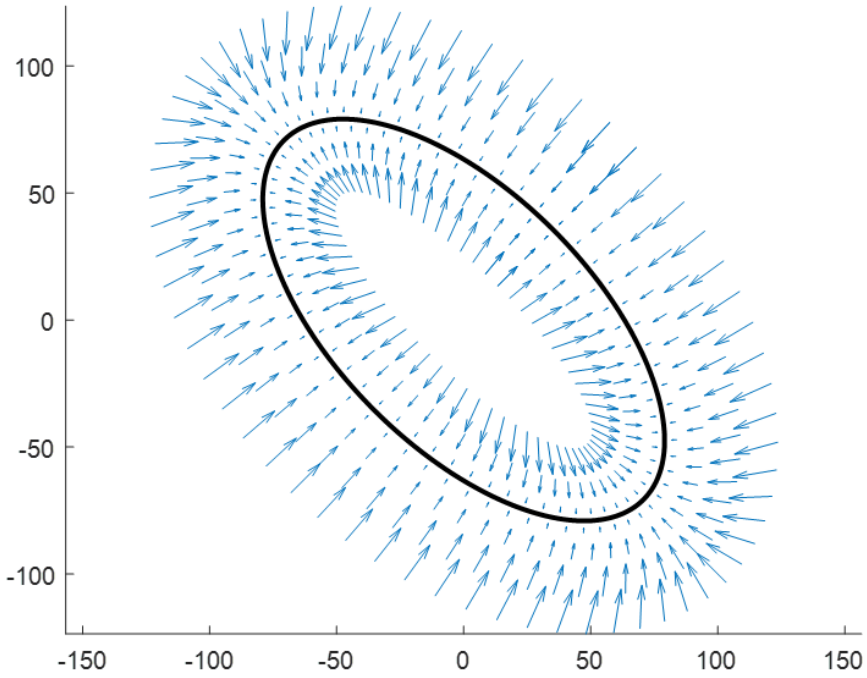

Figure 6.4: Vector field plot of the assistive spring force field for an elliptical trajectory. Arrows indicated the magnitude and direction of the force for the given position error from the desired trajectory.

in from of the subject, with visual feedback of the current wrist position shown as a red dot (Figure 6.5). Subjects were instructed to trace the path of the ellipse and move at a comfortable and continuous pace for the duration of the trial (not stopping at the end of each ellipse). Position, velocity, and force data was collected from the device. Position data was also collected from a motion capture system (Phasespace Impulse X2) at 480 Hz.

Data was collected from seven young adult subjects (4 M, 3 F) with no upper-limb impairment at UC Berkeley under the approval of the UCSF Institutional Review Board with reliance approval by the UC Berkeley Reliance Registry. The right arm of each subject was tested. This was the self-identified dominant hand of six of the seven subjects.

6.4 Results

Analysis Methodology

We consider several metrics for analyzing the effect of virtual mass, assistance, and orientation on the elliptical trajectory tracing. These metrics are computed from the position and

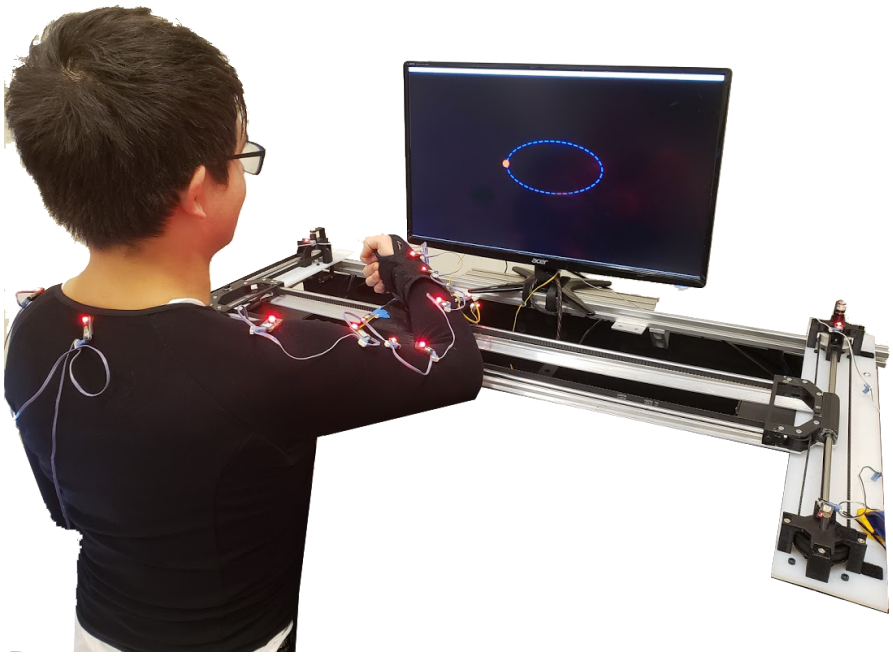

Figure 6.5: Subject connected to rehabilitation device. The monitor displays the desired trajectory and real-time feedback of the subject's wrist position.

force data measured by the device at 330 Hz. The motion capture system was not used in the computation of these metrics. Analysis was completed offline in MATLAB. A 3rd order lowpass Butterworth filter with a 6 Hz cutoff frequency was applied to the x and y components of the force data. The position data was not filtered. Each trial was segmented into individual ellipses for analysis. The following metrics were used to process the experimental data:

- **Normalized mean force (NMF).** We define the mean force (MF) of an ellipse to be the mean value of the magnitude of the interaction force vector across time

$$MF = \frac{1}{K} \sum_{k=1}^{K} \|f(k\| \tag{6.11}$$

  where $f(k)$ is the force vector at timestep k and K is the number of samples in the ellipse. Between subjects, there was variation in the mean interaction force. To assess trends across the subjects, we normalize the mean force for an ellipse by scaling it to the subjects's mean force across all trials:

$$NMF(t) = \frac{MF(t)}{\overline{MF}} \tag{6.12}$$

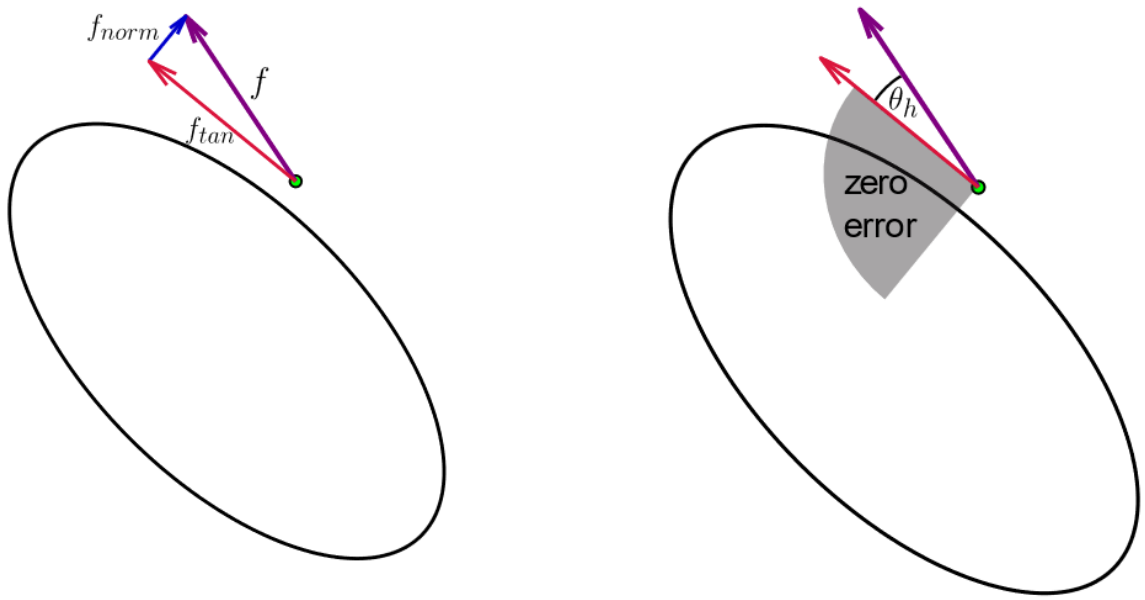

Figure 6.6: Illustration of the interaction force decomposition (Left) and the heading error (Right)

where $NMF(t)$ and $MF(t)$ are the normalized mean force and mean force for a given trial t, and $\overline{MF}$ is the mean of the mean force across all trials.

- **Normalized mean duration (NMD).** The duration for an ellipse is defined as the time taken to complete one ellipse as measured by crossing the semi-major axis. As in Eq. 6.12, we normalize the duration of a given trial relative to the subject's mean duration across all trials.

- **Mean Heading Error(θ_h).** We define the heading error as the angle between the interaction force vector and the tangent vector at the current position as shown in Figure 6.6. To allow for position error correction, we do not penalize interaction force vectors which point toward the ellipse in the normal direction. For example, if the subject's wrist is outside of the desired ellipse path, then a force vector pointing inward toward the ellipse has zero heading error. Likewise, if the wrist is inside of the ellipse, a force vector pointing outward toward the desired path has zero heading error. We formalize this with the equation:

$$\theta_h = \begin{cases} \text{atan2}(\mathbf{f}, \mathbf{u}_t) & \mathbf{f}_n \cdot \mathbf{e} > 0 \\ 0 & else \end{cases} \tag{6.13}$$

where $\mathbf{e}$ is the error vector between the current position p and the desired position d.

- **Zero crossings of the normal force** Zero crossings in the normal force can be indicative of position error correction. The number of zero crossings is counted per ellipse.

- **Coefficients of velocity-curvature** Ellipses provide an opportunity to investigate the relationship between velocity and path curvature. Studied have found that continuous human movements follows the *Two-Thirds Power Law* which states that end-point velocity (V) is a power function of the radius of curvature of the endpoint trajectory. The kinematics of this relationship have been studied outside of robotic devices [108], with a study of the relationship in water [109]. The ability of the robotic device to adjust the virtual mass and viscosity parameters allows for testing of this relationship under loading. Recently, the interaction forces between a robot and human were studied when humans follow robot motion along intuitive and unintuitive velocity profiles [110].

Changes in Ellipse Tracking

We first describe qualitative observations from the experiment. Figure 6.7 shows representative results from a subject completing elliptical trials under unassisted and assisted conditions for the light admittance mass. The data represents a single ellipse of each condition for an ellipse at a rotation of 90 degrees under the light admittance mode. The top row shows an example position trajectory with the color corresponding to the velocity at that point. The sampled interaction force exerted by the subject at the wrist is shown by the black vectors. Comparing the total interaction force in the unassisted and assisted case, we observe that the magnitude of the interaction force is greater in the assisted case, corresponding to a higher velocities. Looking at the normal force, in the unassisted case, we observe that the direction of the force changes sign as the subject adjusts the direction of the interaction force in order to correct for position error. In the unassisted case, we observe that the normal force has a greater magnitude when compared to the unassisted case and the direction of the normal force points outward for the entirety of the trial. This direction indicates that the subject is not carefully modulating the direction of their exerted force in order to follow the trajectory, but, rather is leaning into the spring force to achieve smooth motion. We note that this constant outward direction is not consistent for this subject among all conditions, or between subjects. In studying these force plots, we observe subjects with normal force pointed continuously inward, normal force with a bias in the task space (ie. majority directed upward), or normal force which changes direction throughout the ellipse. For a given trial of the same orientation and controller parameters, subjects tend to follow the same pattern of normal force direction for each of the ten ellipses.

These qualitative observations are supported by the quantitative metrics shown in Figure 6.8 and Table 6.1. These mean metrics are averaged across all subjects with standard

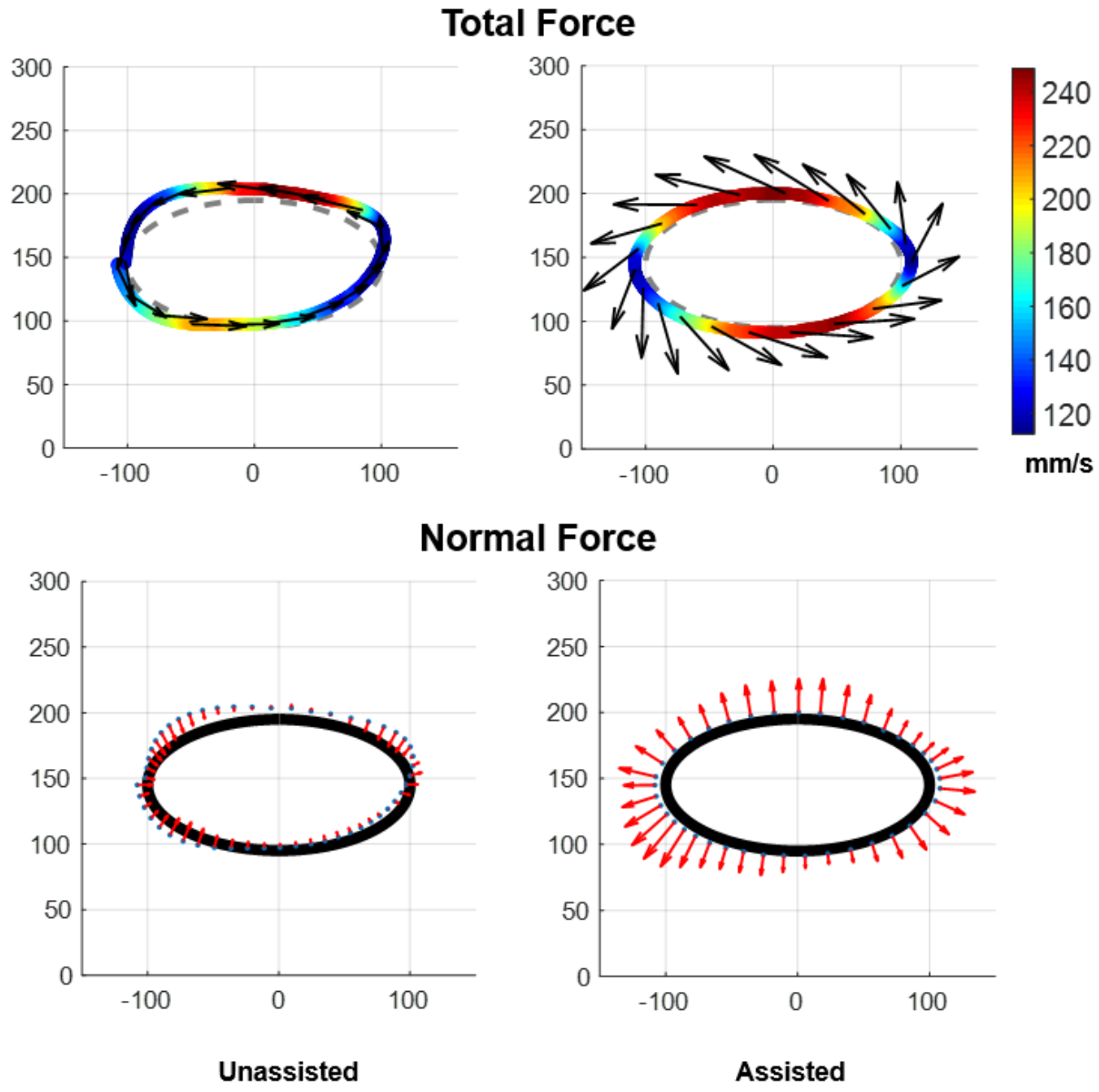

Figure 6.7: Representative data for a subject completing elliptical trajectories under unassisted (left column) and assisted (right column) admittance control. Top row: The end-effector (wrist) position is plotted with the color corresponding to the velocity at that point. The end-effector force is shown in the solid black arrows with arrow length and direction corresponding to the magnitude and direction of the interaction force. Bottom Row: The normal component of the force, f_n is plotted in the red arrows.

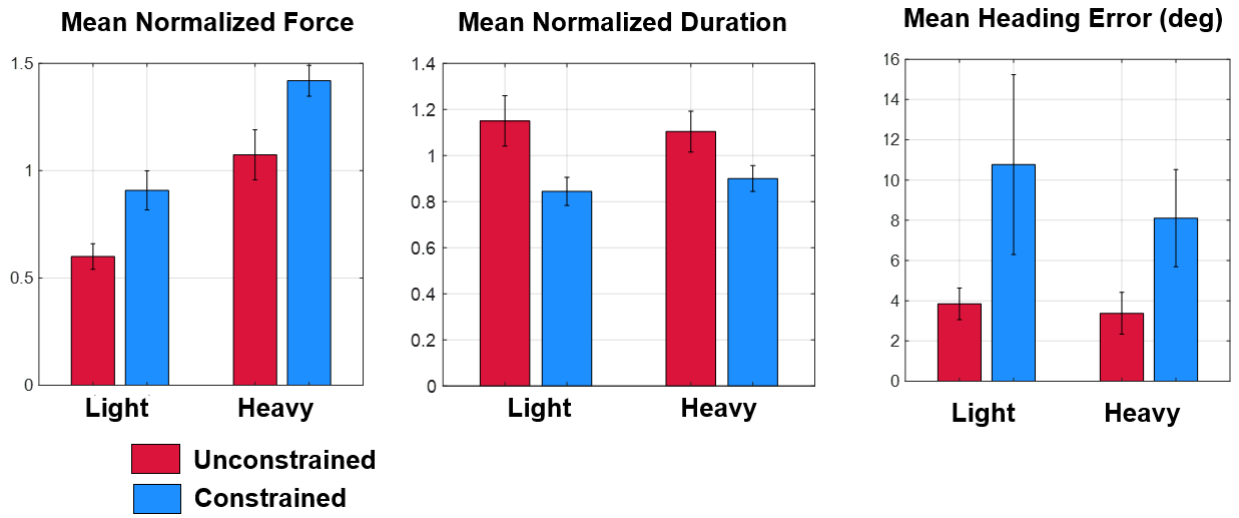

Figure 6.8: Bar charts of the results of of ellipse tracking, showing the mean normalized force (left), mean normalized duration (center), and mean heading error.

Table 6.1: Quantitative interaction metrics under four virtual dynamic conditions: Light Unassisted (LU), Light Assisted (LA), Heavy Unassisted (HU), and Heavy Assisted (HA). The mean is taken across all subjects with the standard deviation corresponding to variance across subjects.

Metric	LU	LA	HU	HA
Norm. Mean Force	0.60 ± 0.06	0.9 ± 0.09	1.07 ± 0.11	1.41 ± 0.08
Norm. Duration	1.14 ± 0.10	0.84 ± 0.07	1.10 ± 0.09	0.90±0.06
Mean Heading Error	4.93 ± 2.97	10.32 ± 4.24	4.21 ± 2.41	8.05 ± 2.21
Zero Crossings	5.77 ± 3.99	3.22 ± 1.35	4.89 ±3.37	3.2 ± 1.39

Table 6.2: Mean force for each subject under four virtual dynamic conditions: Light Unassisted, Light Assisted, Heavy Unassisted, and Heavy Assisted. The mean and standard deviation are taken across all trials for the condition (all orientations).

Subject	Light Unassisted	Light Assisted	Heavy Unassisted	Heavy Assisted
S01	8.14 ± 1.79	16.23 ± 4.94	12.55 ± 1.82	22.30 ± 4.43
S02	2.96 ± 0.34	4.09 ± 0.63	5.04 ± 0.67	6.98±1.28
S03	5.11 ± 1.33	8.37 ± 1.54	10.82 ± 1.79	14.07 ± 2.12
S04	6.70 ± 0.59	8.77 ± 0.93	11.29 ±0.74	13.04 ± 1.47
S05	4.80 ± 0.98	7.98 ±0.87	9.72 ±1.01	12.69 ±1.46
S06	5.85 ± 0.70	8.47 ± 1.64	9.46 ± 0.91	12.99 ±1.57
S07	3.28 ±0.31	4.09 ± 0.47	6.06 ±0.34	6.63 ± 0.53

deviation representing inter-subject variation. These metrics are also averaged across all orientations as no significant difference was found between the orientations when averaged across all subjects. There were significant differences between the orientations for individual subjects, but these were not found to be trends across subjects. The results show a greater mean normalized forced in the assisted case than the unassisted case for both the light and heavy conditions, indicating that subjects are exerting greater active forces with the presence of spring assistance. The mean normalized duration decreases in the unassisted case for both light and heavy conditions, corresponding with the increase in interaction force. With the assistance, subjects are completing each ellipse in less time. The mean heading error increases in the assisted case for both the light and heavy conditions. When comparing the light and heavy condition, the normalized total force increases under the heavier condition. The normalized duration, however, is unaffected by the virtual mass. For the unassisted case, the mean heading error is unaffected by the virtual mass. However, in the assisted case, the mean heading error is greater for the lighter mass.

These results support the hypothesis that subjects will exploit assistance when completing the task as demonstrated by the increase in the heading error. This is also supported by the decrease in zero-crossings in the assisted case. Figure 6.9 shows an example plot of the normal force, highlighting the frequency of zeros crossings in the unassisted case. This varied between subjects with two subjects exhibiting slower, more precise motion. Although the healthy control subjects are capable of completing the task with minimal heading error as demonstrated in the unassissted case, we see a reliance on the assistive force field. The results support the hypothesis that the force field will result in greater exertion as evidenced by the increase in greater mean force and decreased duration.

We note that there were significant difference in the mean force exerted by each subject which are shown in Table 6.2. Despite these differences in the magnitude of force, the trends in the normalized forces were seen across subjects.

Human Arm Inverse Kinematics and Statics Analysis

Thus far, we have only considered metrics relating to the end-effector position, velocity and force. The end-effector measures correspond to motion and torques exerted by the human arm. The inverse kinematic method described in section 5.4 can be used to estimate the joint angles from the device measurement alone (with additional measurement of shoulder joint center and limb segment length). In this study, however, we use active motion capture data to recover the joint angles. The method used is similar to that described in Chapter 2. For each subject, we first utilize an optimization-based parameter identification method to recover an individualized rigid body model. The recovered model consists of three segments in the transverse plane with a torso base segment and two segments for the upper and lower arms which are connected by cylindrical joints corresponding to the shoulder and elbow. The parameter-identification method optimizes for the rigid body parameters which define the model and the positions of the motion capture markers in the local segment frame. The end-effector position recorded by the device was integrated into the optimization and treated

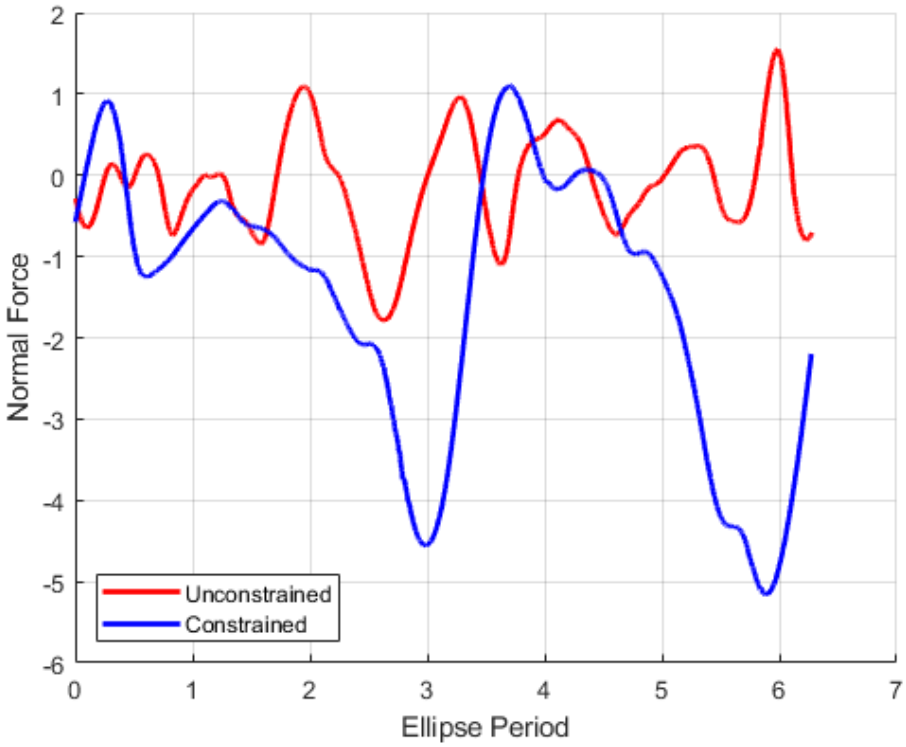

Figure 6.9: Example plots of normal force for an unconstrained (red) and constrained (blue) trials.

as an additional marker rigidly affixed to the forearm segment. The model can then be used to recover the joint angles using frame-wise, non-linear least squares optimization.

With direct measurement of end-effector interaction force, we can estimate the human joint torques using inverse statics analysis. Our estimation of joint torque results in the net joint torque which may consist of active joint torque (generated by muscles) and passive torques due to internal resistances of bones or tissue which must be overcome. From the known force measured at the end-effector, we can use the following equation to compute the torques:

$$\tau = J^T F \tag{6.14}$$

where τ is the vector of joint torques, F is the vector of forces in the global frame, and J is the manipulator Jacobian. For a the two-link upper arm model, we have the manipulator Jacobian J:

$$J = \begin{bmatrix} [-l_{sho} * sin(\theta_{sho}) - -l_{elb} * sin(\theta_{sho} + \theta_{elb}) & -l_{elb} * sin(\theta_{sho} + \theta_{elb}) \\ l_{sho} * cos(\theta_{sho}) + -l_{elb} * cos(\theta_{sho} + \theta_{elb}) & -l_{elb} * cos(\theta_{sho} + \theta_{elb})] \end{bmatrix} \tag{6.15}$$

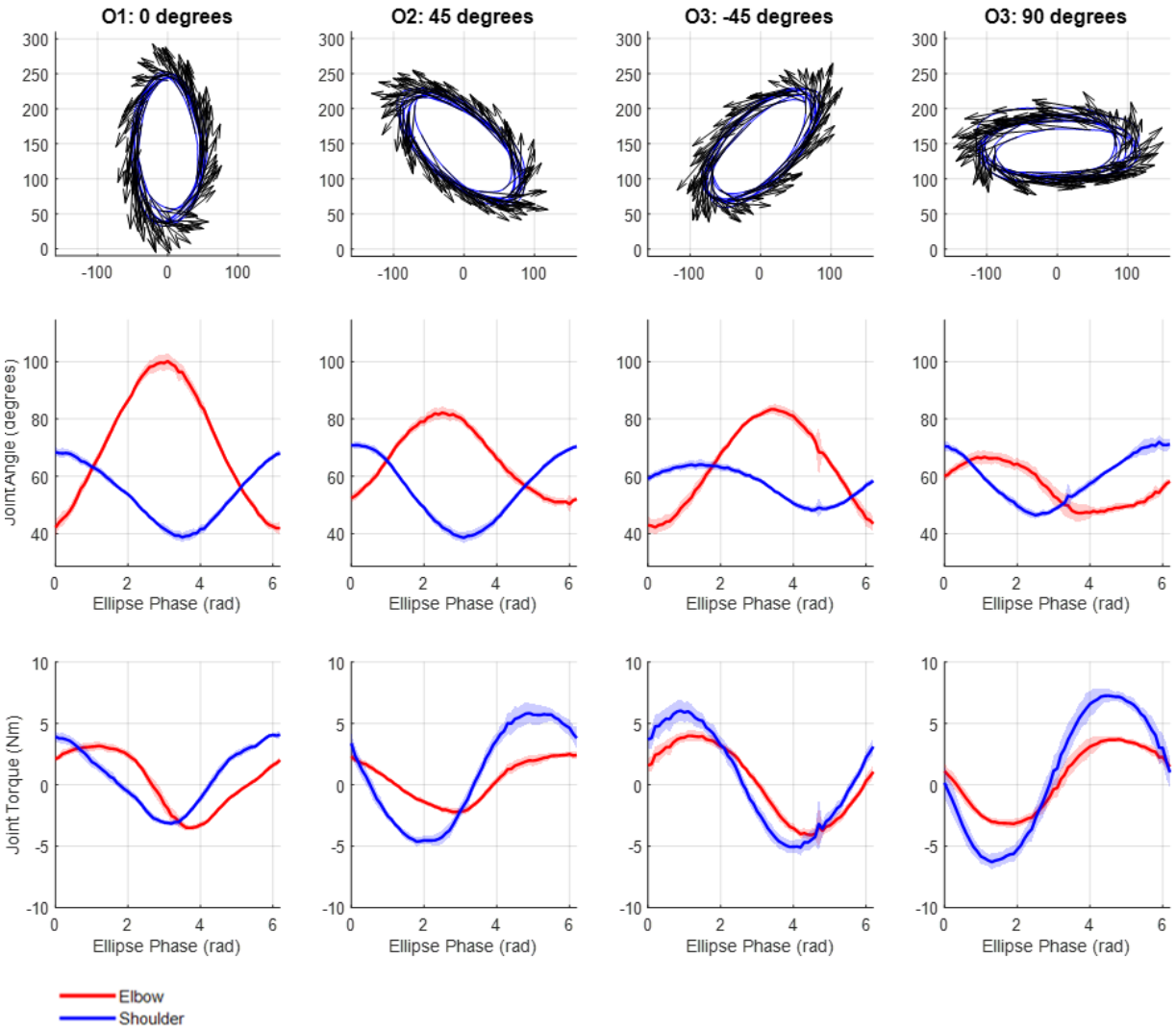

Figure 6.10: Example plots for a subject completing unconstrained elliptical tracing with columns corresponding to the four orientations measured with respect to the vertical. Top Row: plots of trajectory with interaction force overlaid as black arrows. Center row: joint angles for the shoulder (blue) and elbow (red) joints. Bottom row: joint torques estimated from inverse statics analysis for the shoulder (blue) and elbow (red).

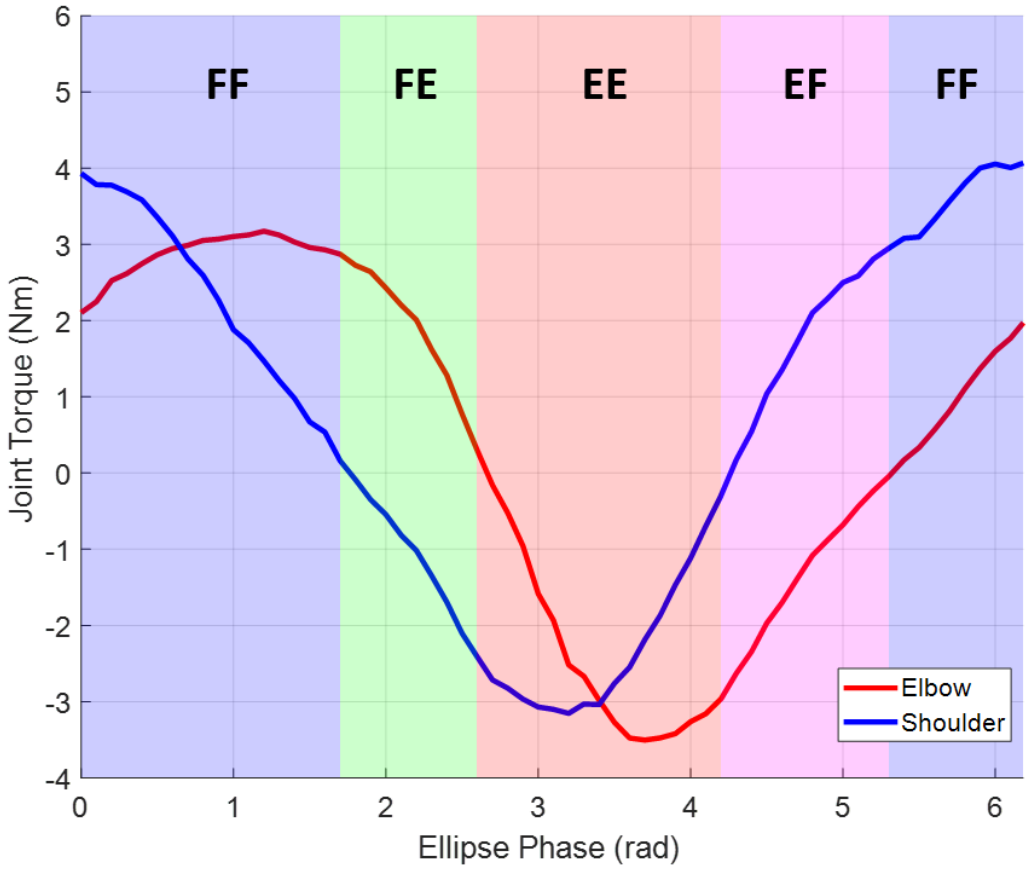

Figure 6.11: Example plots of segmenting ellipse tracking into phases of elbow and shoulder flexion or extension. Estimated mean joint elbow and shoulder torques are shown for an ellipse tracing trial. The background shading relates whether each joint is exerting a torque in flexion (F) or extension (E). The labels indicate the elbow status followed by the shoulder (e.g. FE indicates elbow flexion and shoulder extension).

This static analysis neglects forces due to the arm dynamics. For faster motions, this may result in inaccuracies in the computed joint torque. However, the force due to the acceleration of the mass of the limb segments is relatively small compared to the exerted end-effector forces. We additionally assume that the movement at the shoulder is confined to the glenohumeral joint, with no movement of the scapula or torso.

Figure 6.10 shows example plots of end-effectors forces, estimated joint angles, and estimated joint torques for each orientation. As noted, there were no significant differences in the selected end-effector-based metrics presented in Section 6.4. As intended, we do observe differences in the joint range of motion and joint torques for the different orientations. For example, consider orientation 1 (O1) with semi-major axis aligned with the vertical and orientation 4 (O4) with semi-major axis aligned with the horizontal. The range of motion for the elbow joint is much greater in O1 than O4. The joint angles will be different for reach subjects as they depend on the subjects limb lengths.

From the estimated joint torques, it is straightforward to segment each ellipse trajectory into times in which each joint producing a flexion or extension torque 6.11. This analysis is useful because it allows for a combination of isometric and eccentric/concentric testing of function as part of a higher level task. Additionally, this provides a first step toward designing protocols which target specific deficits at the joint-level or involving joint synergies. Future work can explore incorporating this into the selection of desired trajectories.

6.5 Strength Assessment via Joint Motion Isolation

In this section, we present a framework for the assessment of joint strength and coordination by constraining the end-effector to isolate the motion of a single joint. While it is possible to attain kinematic isolation of the shoulder or elbow motion, we note that this does not correspond to isolating the joint torque. In order to produce an end-effector force tangent to the motion, the immobile joint must produce a torque to balance the torque produced by the joint in motion. Resolving the joint torques from the measured end-effector forces, we can gain insight into the elbow strength, shoulder strength, and joint coordination. The initial feasibility is demonstrated on a single healthy control subject.

Methodology

An illustration of the proposed method for joint isolation is shown in 6.12. For this section, we assume the device is operating at shoulder height and model the arm as a two-joint planar linkage. To isolate the motion of the elbow and shoulder joints, we must know the location of the joint center. This can be accomplished by manual measurement (with a ruler) or through visual sensing with a top mounted camera or motion capture system. We can alternatively estimate the joint center from device data alone by performing a calibration procedure with the device to estimate the joint centers through a functional recovery method. With the device under an unconstrained admittance controller, the subject can complete isolated joint

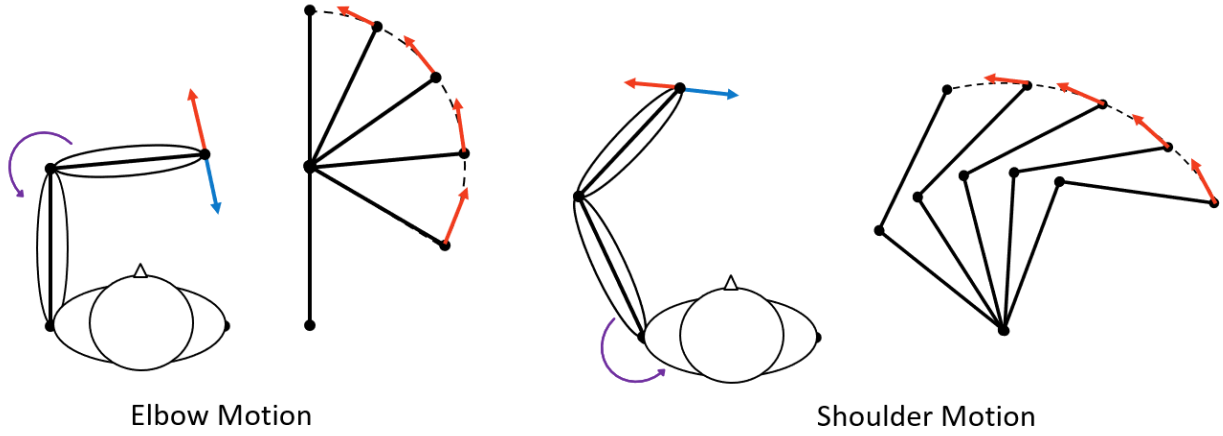

Figure 6.12: Illustration of the joint motion isolation protocol with elbow isolation on the left and shoulder isolation on the right.

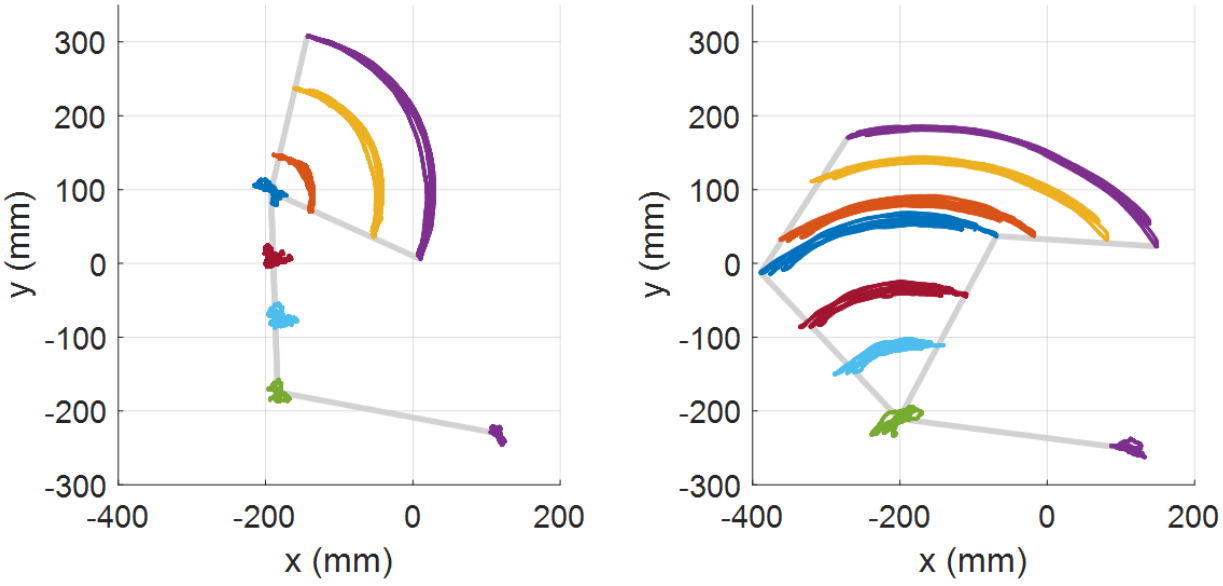

Figure 6.13: Visualization of the motion capture data from the joint isolation trials of the elbow joint (left) and shoulder joint (right).

motions. In the case of a subject with limited ability to complete these isolated motions, the therapist or researcher can guide the arm through these motions. From the position data, we can compute the best fit joint center location.

During the joint isolation protocol, we enforce a circular trajectory, centered at the predetermined joint center. We set a hard constraint which locks the end-effector onto the target trajectory. To implement this, we set our virtual admittance dynamics to have no velocity response along the direction normal to the trajectory (an infinitely stiff spring). The viscosity is set such that there is no carry-over velocity from the previous timestep. To increase the strength required to complete the motion, we make the task more difficult by setting the virtual mass of the admittance control to be high. For the preliminary test, the mass was set to be 16 kg. This value can be adjusted for each individual. In future work, we can expand this by having the mass parameter adjusted in real-time to optimally challenge the subject. Beginning at a fully flexed position, the subject will extend their joint through their full range of motion. This will measure the subjects ability to generate joint torque through a continuous range of joint angles. In the case of a subject with a high level of spasticity and contracture and decreased ability to produce an active joint torque (such as the case for some patients with spinal cord injury), the device can be used to measure the passive stiffness of the arm by moving the subject. This can also be used to identify the passive range of motion.

For this experiment, a passive support was attached to provide gravity compensation for the arm. The device, modified from the Wilmington Robotics Exoskeleton [111], supports the arm just above the elbow. The subject's left arm was otherwise connected to the device as described in Section 6.3. Motion capture markers were used to track the motion of the human and device. The subject, a healthy young adult female, completed trials consisting of three extension-flexion motions, in which she moved from a fully flexed to a fully extended position with a small pause after each completed motion. The elbow was tested with the shoulder at 90 degrees, extended forward in front of the subject. The shoulder was tested with the elbow flexed at approximately 115 degrees.

Results

To demonstrate feasibility of the method, we first show that the device successfully isolated the motion of the joint. Motion capture data was collected to validate the motion of the arm during the joint isolation trials. Figure 6.13 shows traces of the motion capture markers during elbow and shoulder isolation trials. We observe the task space motion along a circular arc corresponding to motion of a single joint. We expect the joint center to remain stationary during the single joint motion. There is, however, some translation of the joint center of interest in both the shoulder and elbow isolation. Several factors may contribute to this error. First, the approximate joint center was marked by a single motion capture marker. For the elbow joint, especially, the position of this marker will be effected by skin motion artifact due to the changing shape of the muscle belly. We expect this to less pronounced for the shoulder joint, whose motion may be due to error in the selection of the joint center

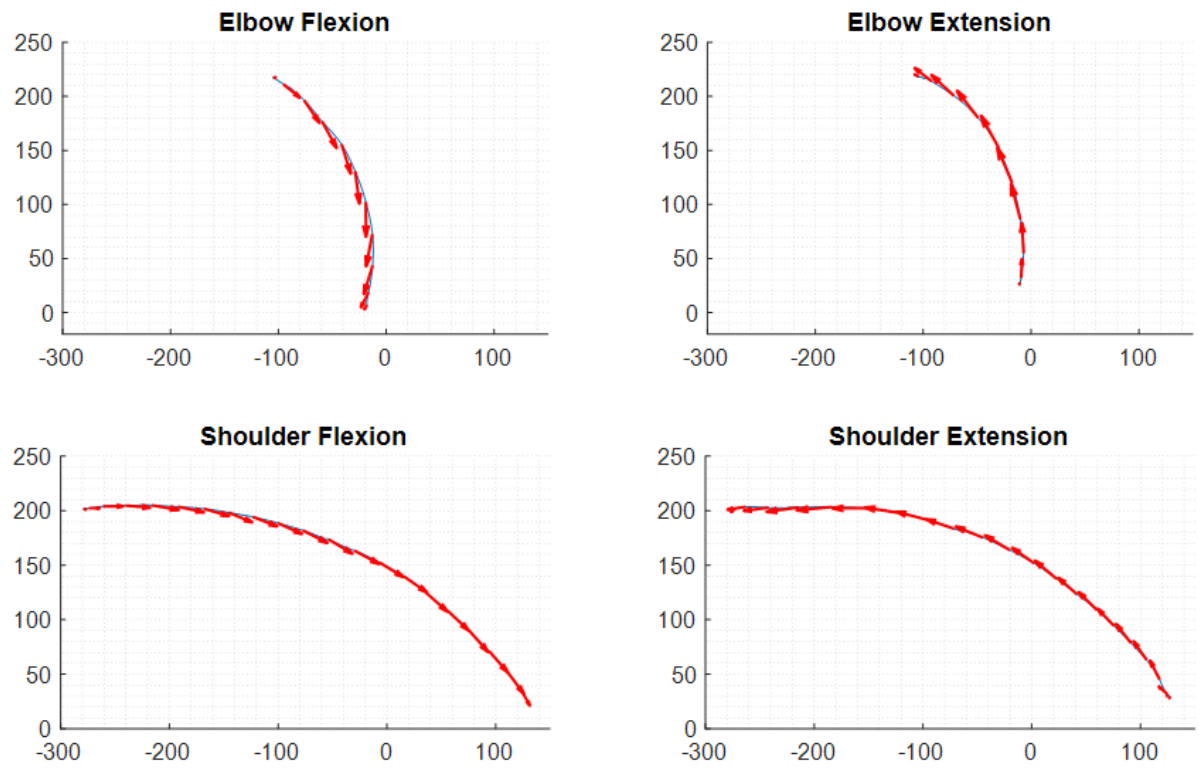

Figure 6.14: Example plots of the end effector forces measured during the joint isolation protocol for flexion and extension of the elbow and shoulder joints.

or the presence of scapular motion during the motion. Additional error may result from the subject moving their torso during the trial.

Examples of the recorded end-effector forces are shown in figure 6.14. The direction of the force is primarily tangent to the joint isolation trajectory, indicating that the subject was able to regulate the combination of the shoulder and elbow torques to generate an end-effector force in the correct direction. Joint torques were recovered using the inverse static analysis method described in Section 6.4. The resultant net joint torques for an elbow isolation trial and a shoulder isolation trial are shown in Figure 6.15. The torque across the three trials was averaged by joint angle with the standard deviation at each point denoted by the shaded region around the mean. We observe good repeatability between the motions as evidenced by the size of the shaded region. For the elbow isolation trials, we observe a nearly constant joint torque of 6 Nm in elbow extension and 5 Nm in elbow flexion. To counterbalance the constant elbow torque, we observe that the shoulder torque must vary with elbow angle. The shoulder must initially produce an extension torque which varies to then produce a flexion torque. In the case of isolated shoulder motion, the elbow joint must produce a torque in the same direction as the shoulder. The shoulder joint torques

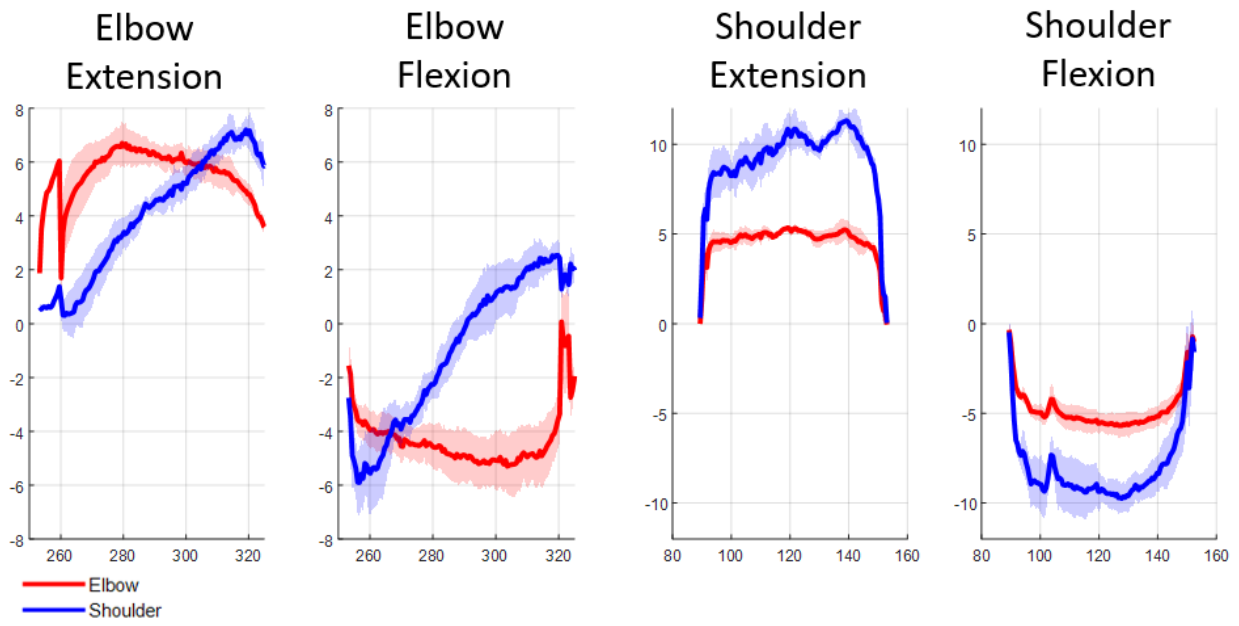

Figure 6.15: Estimated joint torques for shoulder (blue) and elbow (red) joints during elbow isolation (left) and shoulder isolation (right). Each plot shows the mean for three trials with the standard deviation shaded.

were relatively constant at approximately 10 Nm in both extension and flexion. In a subject with deficits in strength or coordination, we would expect to see these manifest in the peak joint torques or the inability to coordinate the joint torque to produce an end effector force tangent to the isolated motion trajectory.

6.6 Chapter Summary

In this chapter, we presented two protocols for robot-assisted assessment using the robotic therapy device described in Chapter 5. These control strategies expand upon the admittance control framework, incorporating assistive force fields and hard constraints.

In the first method, we add a spring term into the virtual dynamics model, providing a restoring force in the direction normal to the trajectory. We demonstrate the ability of our low-cost system to produce force fields on curved trajectories. Human subject experiments studied the phenomenon of subject reliance on assistance. The results support the hypothesis that subjects will exploit the assistive force field and *lean in* to the force field to achieve a smoother motion. While previous work has found that humans *slack* to minimize the energy of the motion, we found that the assistance resulted in greater exertion as evidenced by greater total force and force in the correct direction. These findings can inform the

design of robotic rehabilitation therapy protocols for subjects with coordination deficits. By eliminating the need to produce an end-effector first in a precise direction, assistive force fields can encourage rehabilitiative exercise with greater force output and faster motion.

The second method presents a protocol for assessment of strength and joint coordination through isolated joint motions, enabling measurement through a continuous range of joint angles. Through the implementation of constraints, we can decompose the strength at each joint with the coordination required to complete the motion. Initial feasibility was demonstrated through results on a single healthy control subject.

Chapter 7

Final Thoughts and Future Work

In this dissertation, we explored methods for assessing and assisting human motion with the aim of developing clinically accessible technologies. Our approach integrated biomechanical modeling into the design and development of affordable hardware systems and the accompanying analysis methods. We placed a large emphasis on experimental validation through both hardware characterization and human subjects experiments.

We first presented a framework for improved kinematic recovery by imposing a rigid-body model on noisy data from a single depth camera. A validation study comparing the algorithm to a marker-based motion capture system demonstrated the feasibility of the system to be used as an accurate and fast tool for human motion analysis in clinic. This framework has since been utilized in additional work outside of the scope of this thesis. Building on the kinematic recovery, a dynamic model was integrated and validated [112]. This work estimated joint torques and back loading computed through inverse dynamics analysis using the recovered kinematics. Ongoing and future work using this technology will continue with our clinical collaborators who can utilize the tool for motion analysis studies in patient populations. These methods have been applied to a longitudinal study of a cohort of subjects with adult spinal deformity completing sit-to-stand (STS) [113] and are currently being used as a standard measure in the National Institute of Health REACH Initiative for understanding low-back pain.

Secondly, we introduced a simple passive device which provides bilateral knee assistance during STS. Our preliminary results indicated both the ability to aid in completing the motion by reducing the required human knee torque and the potential to encourage desirable changes in whole-body motion. A number of future directions would expand on these initial experiments. First, an electromyography (EMG) study could be used to better understand how the device and changes in overall strategy affect muscle activity and recruitment. Additionally, the effects of the device should be tested on a larger cohort as well as a clinical cohort. We note that the device was not developed for daily assistance and significant modifications, including the development of a clutch mechanism to disengage the elastic element, would need to be incorporated to allow for daily use. In its current form, the device is more suited to rehabilitation protocols.

Finally, we introduced an affordable upper limb planar robotic manipulandum. Human subjects studies demonstrated the feasibility of the device to be used for robot-assisted assessment and therapy. Building on the admittance control framework, we proposed a number of extensions which were not fully explored in this dissertation, including the integration of a muscle model and a method for the assessment of joint-level range of motion, passive stiffness, and strength through isolated joint motions. In combination with task-space rehabilitation protocols, the joint isolation method has the potential provide decipherable information on the underlying limitations behind functional deficits. This information can be used to inform subject-specific models of impairment which in turn can determine optimal protocols for robot-assisted rehabilitation and assistance. These case studies would greatly benefit from formalized experiments on a larger cohort of patients with upper limb impairment. This is the only way to truly demonstrate the efficacy of the device. Our design has been replicated by our collaborators at Hong Kong University of Science and Technology as well as University of California, San Francisco, for the development of eye-gaze and brain-computer interfaces. Through the development of this low-cost device, we hope to expand the accessibility of robotic platforms for incorporation in clinical care and research studies.

Bibliography

[1] Michelle E. Mlinac and Michelle C. Feng. "Assessment of Activities of Daily Living, Self-Care, and Independence". In: *Archives of Clinical Neuropsychology* (2016). ISSN: 08876177. DOI: 10.1093/arclin/acw049.

[2] Robert Peter Matthew et al. "Kinematic and Kinetic Validation of an Improved Depth Camera Motion Assessment System Using Rigid Bodies". In: *IEEE Journal of Biomedical and Health Informatics* (2019). ISSN: 21682208. DOI: 10.1109/JBHI.2018.2872834.

[3] Sarah Seko et al. "A functional method for generating individualized spine models from motion-capture data". In: *Proceedings of the Annual International Conference of the IEEE Engineering in Medicine and Biology Society, EMBS*. 2018. ISBN: 9781538636466. DOI: 10.1109/EMBC.2018.8512580.

[4] Sarah Seko et al. "Passive Knee Assistance Affects Whole-Body Biomechanics during Sit-to-Stand". In: *Proceedings of the Annual International Conference of the IEEE Engineering in Medicine and Biology Society, EMBS*. 2019. ISBN: 9781538613115. DOI: 10.1109/EMBC.2019.8856477.

[5] William Thomas Crow and David R. Willis. "Estimating cost of care for patients with acute low back pain: a retrospective review of patient records." eng. In: *The Journal of the American Osteopathic Association* 109.4 (2009), pp. 229–33. ISSN: 1945-1997. DOI: 10.7556/jaoa.2009.109.4.229.

[6] André J Cardin and Camille Hadida. "Evaluation of lumbar intersegmental range of motion using flexion-extension radiographs of asymptomatic versus low back pain adults". In: *The Journal of the Canadian Chiropractic Association* 38.2 (June 1994), pp. 83–89. ISSN: 0008-3194.

[7] Balkan Cakir et al. "Evaluation of lumbar spine motion with dynamic X-ray–a reliability analysis." eng. In: *Spine* 31.11 (May 2006), pp. 1258–1264. ISSN: 0362-2436. DOI: 10.1097/01.brs.0000217763.80593.50.

[8] B. J. Van Royen et al. "Accuracy of the sagittal vertical axis in a standing lateral radiograph as a measurement of balance in spinal deformities". In: *European Spine Journal* 7.5 (1998), pp. 408–412. ISSN: 09406719. DOI: 10.1007/s005860050098.

[9] S. S. Coghlin and B. J. McFadyen. "Transfer strategies used to rise from a chair in normal and low back pain subjects". In: *Clinical Biomechanics* 9.2 (1994), pp. 85–92. ISSN: 02680033. DOI: 10.1016/0268-0033(94)90029-9.

[10] Elisabetta Papa and Aurelio Cappozzo. "Sit-to-stand motor strategies investigated in able-bodied young and elderly subjects". In: *Journal of Biomechanics* 33.9 (2000), pp. 1113–1122. ISSN: 00219290. DOI: 10.1016/S0021-9290(00)00046-4.

[11] Stephanie L. Jones et al. "Individuals with non-specific low back pain use a trunk stiffening strategy to maintain upright posture". In: *Journal of Electromyography and Kinesiology* 22.1 (2012), pp. 13–20. ISSN: 10506411. DOI: 10.1016/j.jelekin.2011.10.006.

[12] John Rasmussen et al. "The anybody project – computer analysis of the human body". In: *Biomechanics of Man* (2002), pp. 270–274.

[13] Scott L Delp et al. "OpenSim: Open source to create and analyze dynamic simulations of movement". In: *IEEE transactions on bio-medical engineering* 54.11 (2007), pp. 1940–1950. ISSN: 0018-9294. DOI: 10.1109/TBME.2007.901024. arXiv: 15334406.

[14] W. S. Marras et al. "Accuracy of a three-dimensional lumbar motion monitor for recording dynamic trunk motion characteristics". In: *International Journal of Industrial Ergonomics* 9.1 (1992), pp. 75–87.

[15] Sue A. Ferguson, William S. Marras, and Purnendu Gupta. "Longitudinal quantitative measures of the natural course of low back pain recovery". In: *Spine* 25.15 (2000), pp. 1950–1956. ISSN: 03622436. DOI: 10.1097/00007632-200008010-00014.

[16] William R. Taylor, Tobias Consmüller, and Antonius Rohlmann. "A novel system for the dynamic assessment of back shape". In: *Medical Engineering and Physics* 32.9 (2010), pp. 1080–1083. ISSN: 13504533. DOI: 10.1016/j.medengphy.2010.07.011.

[17] Tobias Consmüller et al. "Comparative evaluation of a novel measurement tool to assess lumbar spine posture and range of motion." In: *European spine journal : official publication of the European Spine Society, the European Spinal Deformity Society, and the European Section of the Cervical Spine Research Society* 21.11 (2012), pp. 2170–80. ISSN: 1432-0932. DOI: 10.1007/s00586-012-2312-1.

[18] Zhengyou Zhang. "Microsoft Kinect sensor and its effect". In: *IEEE Multimedia* 19.2 (2012), pp. 4–10. ISSN: 1070986X. DOI: 10.1109/MMUL.2012.24.

[19] Alexandra Pfister et al. "Comparative abilities of Microsoft Kinect and Vicon 3D motion capture for gait analysis". In: *Journal of Medical Engineering and Technology* 38.5 (2014), pp. 274–280. ISSN: 1464522X. DOI: 10.3109/03091902.2014.909540.

[20] Julia K. Nichols et al. "A Kinect-based movement assessment system: marker position comparison to Vicon". In: *Computer Methods in Biomechanics and Biomedical Engineering* 20.12 (2017), pp. 1289–1298. ISSN: 14768259. DOI: 10.1080/10255842.2017.1340464.

[21] Catalin Ionescu et al. "Human3.6M: Large scale datasets and predictive methods for 3D human sensing in natural environments". In: *IEEE Transactions on Pattern Analysis and Machine Intelligence* 36.7 (2014), pp. 1325–1339. ISSN: 01628828. DOI: 10.1109/TPAMI.2013.248.

[22] Georgios Pavlakos et al. "Coarse-to-fine volumetric prediction for single-image 3D human pose". In: *Proceedings - 30th IEEE Conference on Computer Vision and Pattern Recognition, CVPR 2017* 2017-Janua (2017), pp. 1263–1272. DOI: 10.1109/CVPR.2017.139. arXiv: 1611.07828.

[23] Sungheon Park, Jihye Hwang, and Nojun Kwak. "3D Human Pose Estimation Using Convolutional Neural Networks with 2D Pose Information". In: *European Conference on Computer Vision (ECCV) Workshop*. 2016, pp. 156–169. ISBN: 9783319494081. DOI: 10.1007/978-3-319-49409-8_15. arXiv: 1608.03075.

[24] Xingyi Zhou et al. "Deep kinematic pose regression". In: *European Conference on Computer Vision*. 2016, pp. 186–201. ISBN: 9783319494081. DOI: 10.1007/978-3-319-49409-8_17. arXiv: 1609.05317.

[25] Dushyant Mehta et al. "VNect: Real-time 3D Human Pose Estimation with a Single RGB Camera". In: *ACM Transactions on Graphics* 36.4 (2017), pp. 1–14. ISSN: 15577368. DOI: 10.1145/3072959.3073596. arXiv: 1705.01583.

[26] Carsten Stoll et al. "Fast articulated motion tracking using a sums of Gaussians body model". In: *Proceedings of the IEEE International Conference on Computer Vision*. 2011, pp. 951–958. ISBN: 9781457711015. DOI: 10.1109/ICCV.2011.6126338.

[27] Meng Ding and Guoliang Fan. "Articulated and generalized Gaussian kernel correlation for human pose estimation". In: *IEEE Transactions on Image Processing* 25.2 (2016), pp. 776–789. ISSN: 10577149. DOI: 10.1109/TIP.2015.2507445.

[28] Liang Shuai et al. "Motion Capture with Ellipsoidal Skeleton Using Multiple Depth Cameras". In: *IEEE Transactions on Visualization and Computer Graphics* 23.2 (2017), pp. 1085–1098. ISSN: 10772626. DOI: 10.1109/TVCG.2016.2520926.

[29] NASA. "Anthropometric Source Book Volume I: Anthropometry for Designers". In: I.2 (1978), pp. 1–606. ISSN: 0717-6163. DOI: 10.1007/s13398-014-0173-7.2. arXiv: 9809069v1 [arXiv:gr-qc].

[30] Don B Chaffin. "Development of Computerized Human Static Strength Simulation Model for Job Design". In: *Human Factors and Ergonomics in Manufacturing* 7.4 (1997), pp. 305–322. ISSN: 1090-8471. DOI: 10.1002/(SICI)1520-6564(199723)7:43.3.CO;2-S.

[31] Don B. Chaffin, Gunnar B. J. Andersson, and Bernard J. Martin. *Occupational Biomechanics*. 4th. New York: John Wiley & Sons. ISBN: 0-471-24697-2.

[32] Scott L. Delp and J. Peter Loan. "A graphics-based software system to develop and analyze models of musculoskeletal structures". In: *Computers in Biology and Medicine* 25.1 (1995), pp. 21–34. ISSN: 00104825. DOI: 10.1016/0010-4825(95)98882-E.

[33] Mohammad Ali Rajaee et al. "Comparative evaluation of six quantitative lifting tools to estimate spine loads during static activities". In: *Applied Ergonomics* 48 (2015), pp. 22–32. ISSN: 18729126. DOI: 10.1016/j.apergo.2014.11.002.

[34] Kevin M Lynch and Frank C Park. *Modern Robotics: Mechanics, Planning, and Control*. Cambridge University Press, 2017.

[35] Ko Ayusawa, Gentiane Venture, and Yoshihiko Nakamura. "Identification of humanoid robots dynamics using floating-base motion dynamics". In: *2008 IEEE/RSJ International Conference on Intelligent Robots and Systems, IROS* (2008), pp. 2854–2859. DOI: 10.1109/IROS.2008.4650614.

[36] Johannes Buckup. *Clinical tests for the musculoskeletal system: examinations-signs-phenomena*. TPS, 2016.

[37] Don B. Chaffin, Gunnar B. J. Andersson, and Bernard J. Martin. *Occupational Biomechanics*. 1999.

[38] Simon J. Julier and Jeffrey K. Uhlmann. "New extension of the Kalman filter to nonlinear systems". In: July 1997 (1997), p. 182. ISSN: 0277786X. DOI: 10.1117/12.280797.

[39] E. A. Wan and R. Van Der Merwe. "The unscented Kalman filter for nonlinear estimation". In: *IEEE 2000 Adaptive Systems for Signal Processing, Communications, and Control Symposium, AS-SPCC 2000* February 2000 (2000), pp. 153–158. ISSN: 15270297. DOI: 10.1109/ASSPCC.2000.882463.

[40] Matthew Reed, Miriam A. Manary, and Lawrence W. Schneider. "Methods for Measuring and Representing Automobile Occupant Posture". In: 724 (1999). ISSN: 0148-7191. DOI: 10.4271/1999-01-0959.

[41] Charles K. Anderson, Don B. Chaffin, and Gary D. Herrin. "A study of lumbosacral orientation under varied static loads". In: *Spine* 11.5 (1986), pp. 456–462. ISSN: 15281159. DOI: 10.1097/00007632-198606000-00012.

[42] H.M. Reynolds, C.C. Snow, and J.W. Young. *Spatial Geometry of the Human Pelvis*. Oklahoma City, OK, 1982.

[43] Vicon®. "Plug-in-Gait Marker Placement". In: *Mocap* (2006).

[44] Ge Wu et al. "ISB recommendation on definitions of joint coordinate system of various joints for the reporting of human joint motion—part I: ankle, hip, and spine". In: *Journal of Biomechanics* 35.4 (2002), pp. 543–548. ISSN: 00219290. DOI: 10.1016/S0021-9290(01)00222-6. arXiv: 44.

[45] Hans Kainz et al. "Reliability of functional and predictive methods to estimate the hip joint centre in human motion analysis in healthy adults". In: *Gait and Posture* 53 (2017), pp. 179–184. ISSN: 18792219. DOI: 10.1016/j.gaitpost.2017.01.023.

[46] Thor F. Besier et al. "Repeatability of gait data using a functional hip joint centre and a mean helical knee axis". In: *Journal of Biomechanics* 36.8 (2003), pp. 1159–1168. ISSN: 00219290. DOI: 10.1016/S0021-9290(03)00087-3.

[47] Margaret K.Y. Mak et al. "Joint torques during sit-to-stand in healthy subjects and people with Parkinson's disease". In: *Clinical Biomechanics* 18.3 (2003), pp. 197–206. ISSN: 02680033. DOI: 10.1016/S0268-0033(02)00191-2.

[48] Josip Musić, Roman Kamnik, and Marko Munih. "Model based inertial sensing of human body motion kinematics in sit-to-stand movement". In: *Simulation Modelling Practice and Theory* 16.8 (2008), pp. 933–944. ISSN: 1569190X. DOI: 10.1016/j.simpat.2008.05.005.

[49] L I Lin et al. "A proposal for strength-of-agreement criteria for Lin's Concordance Correlation Coefficient". In: *NIWA Client Report* 45.1 (2005), pp. 307–310. ISSN: 0006-341X. DOI: 10.2307/2532051.

[50] P E Shrout and J L Fleiss. "Intraclass correlations-uses in assessing rater reliability". In: *Psychological Bulletin* 86.2 (1979), pp. 420–428. DOI: 10.1037//0033-2909.86.2.420.

[51] Kenneth O. McGraw and S. P. Wong. "Forming Inferences about Some Intraclass Correlation Coefficients". In: *Psychological Methods* 1.1 (1996), pp. 30–46. ISSN: 1082989X. DOI: 10.1037/1082-989X.1.1.30.

[52] Terry K. Koo and Mae Y. Li. "A Guideline of Selecting and Reporting Intraclass Correlation Coefficients for Reliability Research". In: *Journal of Chiropractic Medicine* 15.2 (2016), pp. 155–163. ISSN: 15563707. DOI: 10.1016/j.jcm.2016.02.012. arXiv: PMC4913118.

[53] Domenic V. Cicchetti. "Guidlines, Criteria, and Rules of Thumb for Evalauting Normed and Standardized Assessment Instruments in Psychology". In: *Psychological Assessment* 6.4 (1994), pp. 284–290. ISSN: 1939-134X. DOI: 10.1037/1040-3590.6.4.284.

[54] Moataz Eltoukhy et al. "Validation of Static and Dynamic Balance Assessment using Microsoft Kinect for Young and Elderly Populations". In: *IEEE Journal of Biomedical and Health Informatics* (2017), pp. 1–1. ISSN: 2168-2194. DOI: 10.1109/JBHI.2017.2686330.

[55] Ferda Ofli, Rizwan Chaudhry, and Gregorij Kurillo. "Berkeley Multimodal Human Action Database (MHAD)". In: (2014).

[56] Q. Wang et al. "Smart Rehabilitation Garment for posture monitoring". In: *Proceedings of the Annual International Conference of the IEEE Engineering in Medicine and Biology Society, EMBS* 2015-Novem (2015), pp. 5736–5739. ISSN: 1557170X. DOI: 10.1109/EMBC.2015.7319695.

[57] R. J. Full and D. E. Koditschek. "Templates and anchors: Neuromechanical hypotheses of legged locomotion on land". In: *Journal of Experimental Biology* (1999). ISSN: 00220949.

[58] Richard G. Snyder, Don B. Chaffin, and Rodney K. Schutz. *Link System of the Human Torso*. Tech. rep. August 1972. Aerospace Medical Research Laboratory.

[59] D. H. Robbins. *Anthropometric Specificaitons for Mid-Sized Male Dummy, Voume 2*. Tech. rep. The UNiversity of Michigan, Transportation Research Institute, 1983.

[60] Alberto Leardini et al. "Validation of a functional method for the estimation of hip joint centre location". In: *Journal of Biomechanics* (1999). ISSN: 00219290. DOI: 10.1016/S0021-9290(98)00148-1.

[61] Oliver Rettig et al. "A new kinematic model of the upper extremity based on functional joint parameter determination for shoulder and elbow". In: *Gait and Posture* (2009). ISSN: 09666362. DOI: 10.1016/j.gaitpost.2009.07.111.

[62] K. Han Kim et al. "Adaptation of torso movement strategies in persons with spinal cord injury or low back pain". In: *Spine* (2010). ISSN: 03622436. DOI: 10.1097/BRS.0b013e3181cb4769.

[63] Maarten F. Bobbert et al. "Searching for strategies to reduce the mechanical demands of the sit-to-stand task with a muscle-actuated optimal control model". In: *Clinical Biomechanics* (2016). ISSN: 18791271. DOI: 10.1016/j.clinbiomech.2016.06.008.

[64] Charles K. Anderson et al. "A biomechanical model of the lumbosacral joint during lifting activities". In: *Journal of Biomechanics* (1985). ISSN: 00219290. DOI: 10.1016/0021-9290(85)90012-0.

[65] A. Nerot, W. Skalli, and X. Wang. "Estimation of spinal joint centers from external back profile and anatomical landmarks". In: *Journal of Biomechanics* (2018). ISSN: 18732380. DOI: 10.1016/j.jbiomech.2017.11.013.

[66] Ge Wu et al. "ISB recommendation on definitions of joint coordinate systems of various joints for the reporting of human joint motion - Part II: Shoulder, elbow, wrist and hand". In: *Journal of Biomechanics* (2005). ISSN: 00219290. DOI: 10.1016/j.jbiomech.2004.05.042.

[67] Richard M. Murray, Zexiang Li, and S. Shankar Sastry. *A mathematical introduction to robotic manipulation*. CRC Press, 1994. ISBN: 9781351469791. DOI: 10.1201/9781315136370.

[68] D H Robbins. *Anthropometric Specifications for Small Female and Large Male Dummies - Volume 3*. 1983.

[69] Patrick O. Riley et al. "Mechanics of a constrained chair-rise". In: *Journal of Biomechanics* (1991). ISSN: 00219290. DOI: 10.1016/0021-9290(91)90328-K.

[70] P. O. Riley, D. E. Krebs, and R. A. Popat. "Biomechanical analysis of failed sit-to-stand". In: *IEEE Transactions on Rehabilitation Engineering* (1997). ISSN: 10636528. DOI: 10.1109/86.650289.

[71] M. A. Hughes et al. "Chair rise strategies in the elderly". In: *Clinical Biomechanics* (1994). ISSN: 02680033. DOI: 10.1016/0268-0033(94)90020-5.

[72] Gary L.K. Shum, Jack Crosbie, and Raymond Y.W. Lee. "Effect of low back pain on the kinematics and joint coordination of the lumbar spine and hip during sit-to-stand and stand-to-sit". In: *Spine* (2005). ISSN: 03622436. DOI: 10.1097/01.brs.0000176195.16128.27.

[73] Bing Chen et al. *Knee exoskeletons for gait rehabilitation and human performance augmentation: A state-of-the-art*. 2019. DOI: 10.1016/j.mechmachtheory.2019.01.016.

[74] Nikos Karavas et al. "Tele-impedance based assistive control for a compliant knee exoskeleton". In: *Robotics and Autonomous Systems*. 2015. DOI: 10.1016/j.robot.2014.09.027.

[75] Max K. Shepherd and Elliott J. Rouse. "Design and Validation of a Torque-Controllable Knee Exoskeleton for Sit-to-Stand Assistance". In: *IEEE/ASME Transactions on Mechatronics* (2017). ISSN: 10834435. DOI: 10.1109/TMECH.2017.2704521.

[76] Bing Chen et al. "Sit-to-stand and stand-to-sit assistance for paraplegic patients with CUHK-EXO exoskeleton". In: *Robotica* (2018). ISSN: 14698668. DOI: 10.1017/S0263574717000546.

[77] Stuart Diller, Carmel Majidi, and Steven H. Collins. "A lightweight, low-power electroadhesive clutch and spring for exoskeleton actuation". In: *Proceedings - IEEE International Conference on Robotics and Automation*. 2016. ISBN: 9781467380263. DOI: 10.1109/ICRA.2016.7487194.

[78] Daisuke Kaneishi, Robert Peter Matthew, and Masayoshi Tomizuka. "Optimal Control Parameterization for ActivelPassive EXoskeleton with Variable Impedance Actuator". In: *Proceedings of the IEEE RAS and EMBS International Conference on Biomedical Robotics and Biomechatronics*. 2018. ISBN: 9781538681831. DOI: 10.1109/BIOROB.2018.8487719.

[79] Daisuke Kaneishi, Masayoshi Tomizuka, and Robert Peter Matthew. "Characterization of Active/Passive Pneumatic Actuators for Assistive Devices". In: *IEEE International Conference on Intelligent Robots and Systems*. 2018. ISBN: 9781538680940. DOI: 10.1109/IROS.2018.8594143.

[80] Kamran Shamaei et al. "Design and evaluation of a quasi-passive knee exoskeleton for investigation of motor adaptation in lower extremity joints". In: *IEEE Transactions on Biomedical Engineering* (2014). ISSN: 15582531. DOI: 10.1109/TBME.2014.2307698.

[81] Kamran Shamaei et al. "Biomechanical effects of stiffness in parallel with the knee joint during walking". In: *IEEE Transactions on Biomedical Engineering* (2015). ISSN: 15582531. DOI: 10.1109/TBME.2015.2428636.

[82] Steven H. Collins, M. Bruce Wiggin, and Gregory S. Sawicki. "Reducing the energy cost of human walking using an unpowered exoskeleton". In: *Nature* (2015). ISSN: 14764687. DOI: 10.1038/nature14288.

[83] F. C. Park, J. E. Bobrow, and S. R. Ploen. "A Lie Group Formulation of Robot Dynamics". In: *The International Journal of Robotics Research* (1995). ISSN: 17413176. DOI: 10.1177/027836499501400606.

[84] H. I. Krebs et al. "Rehabilitation robotics: Performance-based progressive robot-assisted therapy". In: *Autonomous Robots* 15.1 (2003), pp. 7–20. ISSN: 09295593. DOI: 10.1023/A:1024494031121.

[85] Tobias Nef, Marco Guidali, and Robert Riener. "ARMin III – Arm Therapy Exoskeleton with an Ergonomic Shoulder Actuation". In: *Applied Bionics and Biomechanics* (2009). ISSN: 1176-2322. DOI: 10.1155/2009/962956.

[86] Domenico Campolo et al. "H-Man: A planar, H-shape cabled differential robotic manipulandum for experiments on human motor control". In: *Journal of Neuroscience Methods* 235 (2014), pp. 285–297. ISSN: 1872678X. DOI: 10.1016/j.jneumeth.2014.07.003.

[87] Giulio Rosati, Paolo Gallina, and Stefano Masiero. "Design, implementation and clinical tests of a wire-based robot for neurorehabilitation". In: *IEEE Transactions on Neural Systems and Rehabilitation Engineering* (2007). ISSN: 15344320. DOI: 10.1109/TNSRE.2007.908560.

[88] Robert Riener, T. Nef, and G. Colombo. "Robot-aided neurorehabilitation of the upper extremities". In: *Medical and Biological Engineering and Computing* 43.1 (2005), pp. 2–10. ISSN: 01400118. DOI: 10.1007/BF02345116.

[89] Carol L. Richards, Francine Malouin, and Sylvie Nadeau. *Stroke rehabilitation: Clinical picture, assessment, and therapeutic challenge*. 1st ed. Vol. 218. Elsevier B.V., 2015, pp. 253–280. DOI: 10.1016/bs.pbr.2015.01.003.

[90] Angelo Basteris et al. *Training modalities in robot-mediated upper limb rehabilitation in stroke: A framework for classification based on a systematic review*. 2014. DOI: 10.1186/1743-0003-11-111.

[91] Alexander Duschau-wicke et al. "Haptic Constraints for Rehabilitation Robots : An Overview Haptic Constraints". In: *Biomed Tech.* Vol. 55. 2010. DOI: 10.1515/BMT.2010.481.

[92] Rui C.V. Loureiro and William S. Harwin. "Reach & grasp therapy: Design and control of a 9-DOF robotic neuro-rehabilitation system". In: *2007 IEEE 10th International Conference on Rehabilitation Robotics, ICORR'07* 00.c (2007), pp. 757–763. DOI: 10.1109/ICORR.2007.4428510.

[93] Laura Marchal-Crespo and David J. Reinkensmeyer. "Review of control strategies for robotic movement training after neurologic injury". In: *Journal of NeuroEngineering and Rehabilitation* 6.1 (2009). ISSN: 17430003. DOI: 10.1186/1743-0003-6-20.

[94] M. P. Dijkers et al. "Patient and staff acceptance of robotic technology in occupational therapy: A pilot study". In: *Journal of Rehabilitation Research and Development* (1991). ISSN: 0007506X. DOI: 10.1682/jrrd.1991.04.0033.

[95] Paweł Maciejasz et al. "A survey on robotic devices for upper limb rehabilitation". In: *Journal of NeuroEngineering and Rehabilitation* 11.3 (2014). ISSN: 17430003. DOI: 10.1186/1743-0003-11-3.

[96] Arvid Q.L. Keemink, Herman van der Kooij, and Arno H.A. Stienen. "Admittance control for physical human–robot interaction". In: *International Journal of Robotics Research* 37.11 (2018), pp. 1421–1444. ISSN: 17413176. DOI: 10.1177/0278364918768950.

[97] Neville Hogan. "Impedance control: An approach to manipulation: Part I-theory". In: *Journal of Dynamic Systems, Measurement and Control, Transactions of the ASME* (1985). ISSN: 15289028. DOI: 10.1115/1.3140702.

[98] T. Flash and N. Hogan. "The coordination of arm movements: An experimentally confirmed mathematical model". In: *Journal of Neuroscience* 5.7 (1985), pp. 1688–1703. ISSN: 02706474. DOI: 10.1523/jneurosci.05-07-01688.1985.

[99] Laura Dipietro et al. "Submovement changes characterize generalization of motor recovery after stroke". In: *Cortex* 45.3 (2009), pp. 318–324. ISSN: 00109452. DOI: 10.1016/j.cortex.2008.02.008.

[100] Sébastien Mateo et al. "Upper limb kinematics after cervical spinal cord injury: A review". In: *Journal of NeuroEngineering and Rehabilitation* 12.9 (2015). ISSN: 17430003. DOI: 10.1186/1743-0003-12-9.

[101] Evert Jan Nijhof and David A. Gabriel. "Maximum isometric arm forces in the horizontal plane". In: *Journal of Biomechanics* (2006). ISSN: 00219290. DOI: 10.1016/j.jbiomech.2005.01.004.

[102] Kenji Tahara et al. "Sensory-motor control mechanism for reaching movements of a redundant musculo-skeletal arm". In: *Journal of Robotic Systems* (2005). ISSN: 07412223. DOI: 10.1002/rob.20089.

[103] Matjaž Zadravec and Zlatko Matjačić. "Planar arm movement trajectory formation: An optimization based simulation study". In: *Biocybernetics and Biomedical Engineering* (2013). ISSN: 02085216. DOI: 10.1016/j.bbe.2013.03.006.

[104] F Amirabdollahian et al. *Error correction movement for machine assisted stroke rehabilitation*. Ed. by M Mokhtari. Amsterdam, The Netherlands: IOS Press, 2001, pp. 60–65. ISBN: 1-58603-171-6.

[105] David J. Reinkensmeyer et al. "Slacking by the human motor system: Computational models and implic implications for robotic orthoses". In: *Proceedings of the 31st Annual International Conference of the IEEE Engineering in Medicine and Biology Society: Engineering the Future of Biomedicine, EMBC 2009*. 2009. ISBN: 9781424432967. DOI: 10.1109/IEMBS.2009.5333978.

[106] Urs Keller, Georg Rauter, and Robert Riener. "Assist-as-needed path control for the PASCAL rehabilitation robot". In: *IEEE International Conference on Rehabilitation Robotics*. 2013. ISBN: 9781467360241. DOI: 10.1109/ICORR.2013.6650475.

[107] Oliver M. O'Reilly. *Engineering Dynamics: A Primer*. Third Ed. New York: Spinger-Verlag, 2019. DOI: 10.1007/978-3-030-11745-0.

[108] Francesco Lacquaniti, Carlo Terzuolo, and Paolo Viviani. "The law relating the kinematic and figural aspects of drawing movements". In: *Acta Psychologica* (1983). ISSN: 00016918. DOI: 10.1016/0001-6918(83)90027-6.

[109] Giovanna Catavitello et al. "Drawing ellipses in water: evidence for dynamic constraints in the relation between velocity and path curvature". In: *Experimental Brain Research* 234.6 (2016), pp. 1649–1657. ISSN: 14321106. DOI: 10.1007/s00221-016-4569-9.

[110] Pauline Maurice et al. "Velocity-Curvature Patterns Limit Human-Robot Physical Interaction". In: *IEEE Robotics and Automation Letters* 3.1 (2018), pp. 249–256. ISSN: 23773766. DOI: 10.1109/LRA.2017.2737048.

[111] Thierry Haumont et al. "Wilmington robotic exoskeleton: A novel device to maintain arm improvement in muscular disease". In: *Journal of Pediatric Orthopaedics* 31.5 (2011), pp. 44–49. ISSN: 02716798. DOI: 10.1097/BPO.0b013e31821f50b5.

[112] Robert Peter Matthew et al. "Estimating Sit-to-Stand Dynamics Using a Single Depth Camera". In: *IEEE Journal of Biomedical and Health Informatics* (2019). ISSN: 21682208. DOI: 10.1109/JBHI.2019.2897245.

[113] Jeannie F. Bailey et al. "ISSLS PRIZE IN BIOENGINEERING SCIENCE 2019: biomechanical changes in dynamic sagittal balance and lower limb compensatory strategies following realignment surgery in adult spinal deformity patients". In: *European Spine Journal* (2019). ISSN: 14320932. DOI: 10.1007/s00586-019-05925-2.